Development of gas cooled applicators for microwave ablation

Lepers, Benjamin

Award date:
2008

Awarding institution:
University of Bath

DEVELOPMENT OF GAS COOLED APPLICATORS FOR MICROWAVE ABLATION

submitted by Benjamin Lepers for the degree of
Doctor of Philosophy (PhD) of the University of Bath
July 2008

ABSTRACT

A background of electromagnetic theory, heat transfer conduction and heat transfer convection relevant to the development of a 5 mm in diameter laparoscopic microwave applicator and a 2.4 mm in diameter percutaneous applicator for liver ablation therapy is presented. Laparoscopic and percutaneous procedures are described and specifications for each applicator are obtained. Lengths of the radiating section of each applicator have been obtained with a parametric analysis by using a finite element package. Calculated and measured $|S_{11}|$ are in good agreement in water load, the electric and energy distribution (SAR) is obtained with the finite element model for both applicators. Experimental tests have been performed in phantom PAG tissue and in ex vivo bovine liver and showed a good agreement of the energy distribution with the model.

Water movements in the ablation volume during microwave ablation are discussed together with the need of a closed loop circuit applicator which will stop the deposition of an external fluid in the ablation volume.

It is shown that an eccentric air filled coaxial cable has similar electrical properties as a standard low loss PTFE cable and can be used in the design of the laparoscopic and percutaneous gas closed loop microwave applicators.

Temperature evolution at different locations along the shaft of the applicator have been measured and a good prediction of the shaft temperature was obtained with a finite element model solving the incompressible laminar fluid equation together with the heat conduction equation.

This technical solution has been implemented on these two applicators, the shape and lesion size obtained in ex vivo bovine liver is similar as the applicators with the open loop solution. This solution increases the potential range of applications of the 2.4 mm gas cooled applicator.

Contents

List of Figures

Chapter 1

Introduction and background

1.1 Introduction

The subject of this thesis is the development of a closed loop cooling system for percutaneous microwave applicators used in thermal cancer therapy.

For some patients, removal of tumours with open surgery is not possible or involves a too high risk due to the poor condition of the patient. The use of minimally invasive surgery or percutaneous intervention may in this case be adequate and confer advantages such as safety, less trauma [20] and reduced operative time [8].

The principle of the microwave ablation technique depends on heating the tumour tissue in order to kill cancerous cells. During a microwave thermal ablation, intense heat in the targeted tissue close to the applicator tip is generated and heat is conducted along the shaft of the device. Futhermore, heat is generated inside the coax line of the applicator due to electric losses in the cable. To avoid burns to normal tissue in contact with the shaft when using a percutaneous procedure, a cooling circuit needs to be incorporated into the applicator to maintain the temperature of the shaft below a regulatory authority imposed safety limit of 41 °C [75]. To avoid any liquid deposition in the ablation zone, a closed loop cooling circuit has been developed and incorporated to a microwave percutaneous applicator.

This thesis is divided into eight chapters following the advances made during the construction of a closed loop gas cooled microwave applicator.

The first chapter is the introduction with a review of different thermal ablative modalities with the main advantages and drawbacks associated with each ablative technique. The second chapter is a background of electromagnetic interaction with dielectric materials and heat transfer by conduction and convection which occur during a microwave ablation in tissue. These microwave applicators are designated by their shaft diameter which is 5 mm for the large one and 2.4 mm for the small percutaneous one. In the third and fourth chapters, electromagnetic design and tests of the 5 mm and 2.4 mm microwave

applicators with a water cooling circuit are presented together with a discussion of external fluid movement in the ablation zone. These two applicators are perfused applicators because the water used to cooled the shaft exhausts into the tissue. For this reason, they are called open loop water cooled applicators.

Chapter five described the construction and study of an air filled coaxial cable. Electromagnetic calculations and temperature measurements along the shaft are performed in order to show that an air filled coaxial line can be used in the design of two new gas cooled microwave applicators. These applicators do not release any fluid into the tissue because the cooling circuit is closed. For this reason, they are called closed loop cooled applicators. The construction and operation of the 5 mm gas cooled applicator are described in chapter six. In an identical way, the 2.4 mm gas cooled applicator is described in chapter seven. Chapter eight is a summary of this work with suggestion of further research.

1.2 Liver malignancies

The 5 mm and 2.4 mm applicator developed in this work are designed to perform microwave thermal ablation of liver tumours. There are many types of liver tumour; the two main types are hepatocellular carcinoma (HCC) and colorectal secondary metastases. HCC are relatively unusual in western countries with 1.5 deaths per 100 000 head in United Kingdom, but more common in Asia. Colorectal secondary cancers are more common in the west with 30 000 new cases in United Kingdom per annum of which 50 % will develop secondary metastases [11].

1.3 Different thermal treatment modalities

The effect of heat on tissue cells depends on the temperature level and the duration of the treatment. Cell death is achieved for high temperature in a short time or moderate temperature between 42 °C to 45 °C with longer time of exposure [19]. Heat can temporarily stop cell replication [69], coagulate blood vessels [9] and induce cell death. At temperatures higher than 100 °C vaporization and carbonisation occur in the tissue. At high temperature, this hyperthermia technique is referred to as ablation [47].

There exist many different thermal therapy techniques each with its own advantages and disadvantages. Thermal ablative techniques offer benefits for the patient such as reduced morbidity, improved quality of life and shortened recovery time [48].

1.3.1 Percutaneous injection of saline solution

The simplest thermal technique is the percutaneous injection of hyperthermic saline solution through the skin. The saline solution is a sterile solution of 0.9 % sodium chloride

in water. A temperature up to 60 °C induces death of normal liver cells. Furthermore, tumour cells are more sensitive to heat than normal cells because of relative hypoxia and decreased pH levels in the tumor [68], [43]. Saline solution can be used in large quantities and could be used to ablate large tumours [35]. The main drawback is a difficulty in controlling the volume of ablation because the hot fluid flows along the minimum resistance path and some regions of tumour can remain untreated resulting in a potential risk of local cancer recurrence.

1.3.2 Laser

Interstitial laser ablation is performed with laser light emitted from a tip of a thin optical fiber. The interaction between the laser energy and the tissue generates heat in the tissue and causes coagulative necrosis. Lasers used for hyperthermia have a wavelength in the range from 410 nm to 1064 nm, the penetration depth increasing with the wavelength. A Nd:YAG (neodymium-doped yttrium aluminium garnet, $Nd : Y_3Al_5O_{12}$) laser of 1064 nm wavelength gives the greatest penetration depth in tumour liver around 4 mm [54].

The main drawbacks of laser thermotherapy are that it is slow and perform limited lesion size due to the small depth penetration of the light in the tissue. The advantage is that it may be percutaneously applied with an optical fiber and used in conjunction with Magnetic Resonance Imaging (MRI) machines for placement and real time monitoring [77]. This technique has been used by Amin *et al* [2].

1.3.3 Radiofrequency

The most commonly used thermal ablation technique in interventional radiology thermal ablation is percutaneous radiofrequency ablation.

Currents at frequencies from 450 to 1000 kHz flow inside the tissue, producing ionic agitation, molecular friction, denaturation of proteins, cell membrane disintegration and generating heat inside the tissue. In a bipolar system, two electrodes are located at the end of the applicator, so the current field is relatively well confined between these two electrodes. In a monopolar system, the currents circulate between the electrode inserted in the tumour and a grounding pad located on the thighs or back muscles of the patient. In Tokyo University Tateishi *et al* [72] have treated 1000 patients in 4 years between 1999 and 2003 with percutaneous radiofrequency probes for liver cancer. Treatments have increased the rate of survival of patients.

The main disadvantage is that the tissue becomes less and less electrically conductive during dessication. This dessication or drying process decreases the heating process efficiency during the ablation and consequently limits the ablation volume. Finally, in the case of a monopolar system, there are some potential leakage currents through the body

that are potentially harmful for the patient and lead to undesirable burning of normal tissue [66]. The nervous system is sensitive to these currents and it is sometimes painful for the patient with an associated risk of electric shock.

1.3.4 Ultrasound

A high intensity focussed ultrasound technique can also produces significant tissue heating. The excitation frequency of the transducer is between 0.5 to 4.0 MHz. Mechanical waves propagate in the tissue and intense tissue agitation generates heat leading to protein denaturation and cell death. This is the least invasive technique and consists of focussing a high amplitude ultrasound wave on a spot located in the tumour. The heated spot is scanned through the tumour volume and causes coagulation.

There exist also interstitial ultrasound applicators which are inserted via a percutaneous route into the tumour. A review of interstitial ultrasound applicator is given by Lafon *et al* [44].

The source of ultrasound generation is a piezoelectric transducer vibrating at high frequency. To improve the mechanical wave transmission the patient is usually immersed in a water bath. Overall, the installation is important compared to other hyperthermia systems.

1.3.5 Cryotherapy

Cryotherapy is capable of treating large lesions [6] but with higher risk of complications such as systemic shock and post operation bleeding. The cryoprobe is a liquid nitrogen cooled probe from 3 up to 10 mm diameter which is inserted in the center of the tumour to generate a low temperature volume encapsulating the tumour. To ensure cell death, a few cycles are performed. As a consequence, treatment time for large tumours is up to several hours. Intra and extra cellular ice formation [50], osmotic change [79], ice expansion [41] and ischemia following the destruction of microvasculature [63], [64] are mechanisms involved in the cell destruction.

1.3.6 Microwave

Microwaves have a high potential for tissue heating because microwaves interact with water molecules. Human tissue has high water content of around 70 % to 80 % by mass [22]. This technique makes it possible to carry large and small ablation of cancer tissue in minutes [70].

The frequency range of microwaves is between 0.3 GHz and 300 GHz [55] with penetration depth from several millimetres to several centimetres in biological tissue. The 2.45 GHz frequency gives an optimum between the penetration depth and the effectiveness in

heating the tissue by dipole molecules vibration. For this reason, the applicators described in this thesis operate at 2.45 GHz (which is also the operating frequency of commercial microwave ovens). Absorption of microwaves is relatively uniform because the water content is relatively uniform in high water content organs such as liver or kidney.

To ensure that the major part of the microwave radiation is absorbed in tissue, the design of the applicator plays a fundamental role. The percutaneous applicators presented need to perform large and approximately spherical ablations in solid organs. A spherical distribution of energy is the best shape in order to target the tumour. Once the radiating section is inserted in the tumour and, providing that the radius of the tumour is smaller than the radius of the ablation sphere performed with the applicator, the tumour tissue is totally treated.

For large tumours, the ability to perform large volume ablation is an important advantage because the tumour can be ablated in one session, with a safety margin of normal tissue. A safety margin of one centimetre and a one session treatment for the tumour are important factors that minimize local recurrence risk [53].

The physical processes that occur during a microwave ablation involve microwave energy and heat transfer into the tissue. Elements of electromagnetism and heat transfer theory are given in the next chapter in order to understand the development of these microwave applicators.

Chapter 2

Microwave heating principles

Microwaves are electromagnetic waves in the range from 0.3 GHz to 300 GHz [32]. The interaction of microwaves and a lossy dielectric material such as a biological tissue generates heat. For medical treatment, frequencies from 1 to 10 GHz are used with a typical wavelength in the tissue of around one centimetre. The strong interaction between microwaves and dipole molecules, and the fact that biological tissues have a relatively homogenous high water content gives a good predictability and efficiency for the microwave heating technique.

To perform tumour ablation by localised microwave heating, an applicator has to be designed and developed. The radiating section of the applicator requires a careful electromagnetic design to ensure good energy transmission into the tissue.

During a microwave ablation, heat is generated in the tissue surrounding the radiating tip of the applicator and then transported outward by thermal conduction and convection mechanisms.

Relevant elements of electromagnetic theory used for the design of the radiating section of each applicator are described. Then heat conduction and convection mechanisms occurring during a microwave ablation in a biological tissue are discussed with the heat conduction equation.

2.1 Electromagnetic wave propagation in a dielectric

2.1.1 Maxwell's equations

When an electric charge is following a non uniform motion, it generates an electric field and a magnetic field. For example a simple wire loop carrying an alternating current will create a magnetic and electric field which radiates into space. All time varying electric phenomena are described by Maxwell's equations. Stored energy in an electromagnetic field can be transported through vacuum and absorbed by lossy materials. Maxwell's equa-

tions give the relationship between the macroscopic electric field, magnetic field, electric flux and magnetic flux. There are a set of four equations linking the electric field with the magnetic field and the conservation of electric and magnetic charge. The conservation of electric flux implies that the electric flux through a closed surface surrounding an electric charge is equal to the charge inside the volume delimited by the area. This is referred as Gauss's law:

$$\int_{\partial\Omega} \boldsymbol{D} \cdot \boldsymbol{ds} = \int_{\Omega} \rho dv \tag{2.1}$$

with $\boldsymbol{D}[Cm^{-2}]$ the electric flux density and $\rho[Cm^{-3}]$ the charge density. $\boldsymbol{ds}$ is the unit vector pointing out the surface. The charge is enclosed in the volume Ω with the $\partial\Omega$ the attached surface. There is also conservation of the magnetic flux through any closed surface surrounding a volume. Because a magnetic charge does not exist, the conservation of magnetic flux is expressed as:

$$\int_{\partial\Omega} \boldsymbol{B} \cdot \boldsymbol{ds} = 0 \tag{2.2}$$

with $\boldsymbol{B}[Vsm^{-2}]$ the magnetic flux. Faraday discovered that a time varying magnetic flux over a surface generates a circulation of electric charges along a circuit C. The relationship between the magnetic flux $\boldsymbol{B}$ and electric field $\boldsymbol{E}$ is expressed by:

$$\int_{C} \boldsymbol{E} \cdot \boldsymbol{dl} = -\int_{\partial\Omega} \frac{\partial \boldsymbol{B}}{\partial t} \cdot \boldsymbol{ds} \tag{2.3}$$

and is known as Faraday's law. Finally, Maxwell suggested that a time varying electric flux must generate a circulation of magnetic field. The relationship is:

$$\int_{C} \boldsymbol{H} \cdot \boldsymbol{dl} = \int_{\partial\Omega} \boldsymbol{J} \cdot \boldsymbol{ds} + \int_{\partial\Omega} \frac{\partial \boldsymbol{D}}{\partial t} \cdot \boldsymbol{ds} \tag{2.4}$$

where $\boldsymbol{J}[Am^{-3}]$ is the volume current density and $\frac{\partial \boldsymbol{D}}{\partial t}$, the displacement current. These equations in integral form are referred as Maxwell's equations and form the complete description of time varying electromagnetic phenomenon.

$$\int_{C} \boldsymbol{E} \cdot \boldsymbol{dl} = -\int_{\partial\Omega} \frac{\partial \boldsymbol{B}}{\partial t} \cdot \boldsymbol{ds} \tag{2.5}$$

$$\int_{C} \boldsymbol{H} \cdot \boldsymbol{dl} = \int_{\partial\Omega} \boldsymbol{J} \cdot \boldsymbol{ds} + \int_{\partial\Omega} \frac{\partial \boldsymbol{D}}{\partial t} \cdot \boldsymbol{ds} \tag{2.6}$$

$$\int_{\partial\Omega} \boldsymbol{D} \cdot \boldsymbol{ds} = \int_{\Omega} \rho dv \tag{2.7}$$

$$\int_{\partial\Omega} \boldsymbol{B} \cdot \boldsymbol{ds} = 0 \tag{2.8}$$

They can be expressed in differential form using rotational and divergence operators:

$$\nabla \wedge \boldsymbol{E} = -\frac{\partial \boldsymbol{B}}{\partial t} \tag{2.9}$$

$$\nabla \wedge \boldsymbol{H} = \frac{\partial \boldsymbol{D}}{\partial t} + \boldsymbol{J} \tag{2.10}$$

$$\nabla \cdot \boldsymbol{D} = \rho \tag{2.11}$$

$$\nabla \cdot \boldsymbol{B} = 0 \tag{2.12}$$

These equations govern the behaviour of an electromagnetic wave. For simple cases and with assumptions, some analytical solutions can be obtained, for more complex geometry, numerical method such as the finite element method has to be used in order to solve the field distribution for example or perform a parametric analysis in order to determine the optimal lengths of an antenna.

2.1.2 Energy of an electromagnetic wave

2.1.2.1 Poynting vector

To analyse the electromagnetic energy transported by an electromagnetic wave, the cross product between the electric field and magnetic field gives the instantaneous power density per unit area and is defined as the Poynting vector:

$$\boldsymbol{S}(t) = \boldsymbol{E}(t) \wedge \boldsymbol{H}(t) \tag{2.13}$$

The magnitude of $\boldsymbol{S}[Wm^{-2}]$ is the energy density of the electromagnetic field and its direction gives the electromagnetic wave propagation direction. For a sinusoidal field, the average real power per unit area is:

$$\boldsymbol{S}_{av} = \frac{1}{2} Re[\boldsymbol{E} \wedge \boldsymbol{H}^*] \tag{2.14}$$

with $\boldsymbol{E} = \boldsymbol{E_0} e^{-j\omega t}$ and $\boldsymbol{H} = \boldsymbol{H_0} e^{-j\omega t}$ the complex representation of the electric and magnetic field. In some applications it is useful to calculate this vector field to know the direction of the electromagnetic energy flow.

2.1.3 Electric and magnetic energy

Electric energy is stored in the electric field. For a linear isotropic homogenous lossless material, the electric flux density is proportional to the electric field. The variation of volumetric electric energy density is:

$$\boldsymbol{E} \cdot d\boldsymbol{D} = \boldsymbol{E} \cdot \epsilon d\boldsymbol{E} = \frac{\epsilon}{2} d\boldsymbol{E}^2 = dW_e \tag{2.15}$$

The electric energy $W_e[Jm^{-3}]$ density is defined by:

$$W_e = \frac{\epsilon}{2}\boldsymbol{E}^2 \tag{2.16}$$

with ϵ the electric permittivity of the medium.

In a similar way, energy is stored in the magnetic field and the variation of volumetric magnetic energy density is:

$$\boldsymbol{H} \cdot d\boldsymbol{B} = \boldsymbol{H}\mu \cdot d\boldsymbol{H} = \frac{\mu}{2} d\boldsymbol{H}^2 = dW_m \tag{2.17}$$

The magnetic energy $W_m[Jm^{-3}]$ density is:

$$W_m = \frac{\mu}{2}\boldsymbol{H}^2 \tag{2.18}$$

with μ the magnetic permeability of the medium.

2.1.4 Poynting theorem

To determine the transfer of electromagnetic energy for time varying fields for a given volume Ω of surface $\partial\Omega$, the divergence of the Poynting vector $\boldsymbol{S}$ is taken and Maxwell's equations 2.9 and 2.10 are used:

$$\nabla \cdot \boldsymbol{S} = \nabla \cdot (\boldsymbol{E} \wedge \boldsymbol{H}) = \boldsymbol{H} \cdot (\nabla \wedge \boldsymbol{E}) - \boldsymbol{E} \cdot (\nabla \wedge \boldsymbol{H}) \tag{2.19}$$

$$= -\boldsymbol{H} \cdot \frac{\partial \boldsymbol{B}}{\partial t} - \boldsymbol{E} \cdot \frac{\partial \boldsymbol{D}}{\partial t} - \boldsymbol{E} \cdot \boldsymbol{J} \tag{2.20}$$

with the first two terms being the time variation of electric and magnetic energy. The last term represents the energy transformed in a different form such as heat. The current density $\boldsymbol{J}$ is expressed as a function of the electric field with the conductivity σ by assuming that the material is linear, lossless, homogenous and isotropic.

$$\boldsymbol{J} = \sigma \boldsymbol{E} \tag{2.21}$$

$$\nabla \cdot \boldsymbol{S} = -\frac{\partial W_m}{\partial t} - \frac{\partial W_e}{\partial t} - \sigma E^2 \tag{2.22}$$

This equation of energy in differential form can be integrated over a volume Ω of surface $\partial\Omega$ to understand the significance of each term.

$$\int_{\partial\Omega} \boldsymbol{n} \cdot \boldsymbol{S} dA = -\frac{\partial}{\partial t}\int_{\Omega} (W_e + W_m) dV - \int_{\Omega} \sigma E^2 dV \tag{2.23}$$

This equation is referred as the Poynting theorem. The flux of electromagnetic power through the surface $\partial\Omega$ is equal to the decrease of electric and magnetic energy and minus the energy lost in other forms such as heat [26].

2.1.5 Dielectric materials

The generation of heat inside a material is due to the interaction of electromagnetic waves and the molecules of the material. Between a perfect conductor and a perfectly insulating material, there is a large class of materials called dielectrics.

2.1.5.1 Dielectric in an electric field

For an insulating material, electric charges are linked with atoms and molecules. When an electric field is applied, a force is applied on the electric charges but they are maintained by the chemical bonds of the atoms or molecules and can only move slightly from their equilibrium positions. The consequence is formation of an induced dipole moment and the material is said to be polarized. The electric flux density in any medium is then:

$$\boldsymbol{D} = \epsilon_0 \boldsymbol{E} + \boldsymbol{P} \tag{2.24}$$

where $\boldsymbol{P}$ is the polarized electric field and represents the effect of the displaced bound charges in the material. ϵ_0 is the electric permittivity of free space. The electrical behaviour of a material is linear if the polarization vector is proportional to the electric field. If the dielectric properties are independant of the location in the material, the material is homogenous.

If the properties are independent of the direction, in other words, there is no preferential direction, the material is isotropic. For our electromagnetic analysis, the material is always assumed to be homogenous and isotropic. The reason is that heat generation due to microwave interaction with the tissue is mainly a function of the water and ionic fluid content. The fluid inside a tissue, liver for example, is distributed approximately in a homogenous and isotropic manner. Hence, it is reasonable to consider a biological tissue as homogenous and isotropic from the point of view of microwave heating. Since, biological tissues are lossy dielectric materials with high water content, microwave energy is absorbed and heat is generated inside a volume of tissue.

During a microwave ablation the tissue dessicates, the water content decreases and the dielectric properties of the tissue change [22]. To take into account the changing dielectric property of the tissue, the dielectric permittivity of the tissue can be written as a function of a parameter such as the tissue temperature in order to model more accurately the energy deposited by microwave ablation during an ablation.

Since the electric field and polarized field are collinear for a homogenous and isotropic material, the polarized field is expressed as:

$$\boldsymbol{P} = \epsilon_0 \chi \boldsymbol{E} \tag{2.25}$$

with $\epsilon_0 = 8.8541 \times 10^{-12} Fm^{-1}$ the electric permittivity of vacuum and χ the proportional factor called the dielectric susceptibility. The electric flux density can be written by using

2.24 and 2.25:

$$\boldsymbol{D} = \epsilon_0(1+\chi)\boldsymbol{E} \tag{2.26}$$

where $(1+\chi)$ is the relative permittivity or dielectric constant of the medium. For a linear, homogenous and isotropic material the electric flux density is linked to the electric field of the material by:

$$\boldsymbol{D} = \epsilon_0\epsilon_r\boldsymbol{E} = \epsilon\boldsymbol{E} \tag{2.27}$$

with ϵ the permittivity of the medium and $\epsilon_r = 1+\chi$ is the relative permittivity.

2.1.5.2 Dielectric in a magnetic field

In a similar way to the electric and polarized electric field, the magnetic flux is defined by:

$$\boldsymbol{B} = \mu_0(\boldsymbol{H} + \boldsymbol{M}) \tag{2.28}$$

with $\boldsymbol{M}$ the magnetic polarization or magnetization, and $\mu_0 = 4\pi \times 10^{-7}\ Hm^{-1}$ the magnetic permeability of vacuum. For a linear homogeneous and isotropic medium, the magnetization is directly proportional to the magnetic field:

$$\boldsymbol{M} = \chi_m\boldsymbol{H} \tag{2.29}$$

with χ_m the magnetic susceptibility. The magnetic flux becomes by using 2.28 and 2.29

$$\boldsymbol{B} = \mu_0(1+\chi_m)\boldsymbol{H} = \mu_0\mu_r\boldsymbol{H} = \mu\boldsymbol{H} \tag{2.30}$$

For all biological tissues, the relative permeability is $\mu_r = 1$.

2.1.6 The constitutive equations

For a linear, homogenous and isotropic medium, the relationship between electric flux $\boldsymbol{D}$ and electric field $\boldsymbol{E}$ and between magnetic flux $\boldsymbol{B}$ and magnetic field $\boldsymbol{H}$ are given in equations 2.31 and 2.32.

$$\boldsymbol{D} = \epsilon\boldsymbol{E} \tag{2.31}$$

$$\boldsymbol{B} = \mu\boldsymbol{H} \tag{2.32}$$

$$\boldsymbol{J} = \sigma\boldsymbol{E} \tag{2.33}$$

with the conduction current density $\boldsymbol{J}$ expressed as a function of the conductivity σ and the electric field $\boldsymbol{E}$ in equation 2.33.

For a sinusoidal electromagnetic wave, the complex notation can be used to write the Maxwell's equation in the frequency domain. Each component of the electric and magnetic field in a given coordinate system oscillates at the angular frequency ω. For one component, the form of the time varying field component is:

$$A = A_0 e^{j\omega t + \phi} \tag{2.34}$$

with A the amplitude at instant t, A_0 the maximal amplitude and ϕ the phase of the component A of the field. To characterise the response of a material submitted to an electromagnetic wave, a convenient parameter is the complex permittivity. This parameter is described below with a wave propagating in a lossy medium.

2.1.7 Complex permittivity

The interaction of microwaves with tissue generates heat and the process of heat generation is mainly due to friction of dipolar water molecules during vibration and collision process [51], [62]. Within an electromagnetic field polar molecules attempt to align uniformly to the direction of the field. Molecules attempt to realign when submitted to the oscillating microwave field. This oscillating movement of polar molecules generates heat by friction.

The relative permittivity of a material indicates how much slower the electromagnetic waves propagate within the material compared to vaccum. The permittivity of a biological tissue is frequency dependant and changes with temperature during an ablation. For a lossy material the relative permittivity from equation 2.27 is a complex number and takes into account the electrical losses with the imaginary part $\epsilon^{''}$. It is written as:

$$\epsilon = \epsilon^{'} - j\epsilon^{''} \tag{2.35}$$

The real part $\epsilon^{'}$ is the dielectric constant and represent the material's ability to store electrical energy. The imaginary part $\epsilon^{''}$ is the loss factor which include the dissipation losses due to damping of vibrating dipole moments [56]. For a sinusoidal time varying electromagnetic wave, the circulation of the magnetic flux from Maxwell's equation 2.10 can be written with the complex permittivity as:

$$\begin{aligned} \nabla \wedge \boldsymbol{H} &= j\omega \boldsymbol{D} + \sigma \boldsymbol{E} && (2.36)\\ &= j\omega\epsilon \boldsymbol{E} + \sigma \boldsymbol{E} && (2.37)\\ &= j\omega\epsilon^{'} \boldsymbol{E} + (\omega\epsilon^{''} + \sigma)\boldsymbol{E} && (2.38)\\ &= j\omega \left(\epsilon^{'} - j\epsilon^{''} - j\frac{\sigma}{\omega}\right) \boldsymbol{E} && (2.39) \end{aligned}$$

From equation 2.38 the loss due to dielectric damping $\omega\epsilon^{''}$ and the conductivity loss σ are the total electric loss term. The term $\omega\epsilon^{''} + \sigma$ can be seen as the total effective

conductivity. The loss tangent is defined as:

$$tan\,\delta \;=\; \frac{\omega\epsilon^{''}+\sigma}{\omega\epsilon^{'}} \tag{2.40}$$

and is the ratio of total loss over the real part of the complex permittivity defined in equation 2.35.

Losses are due to translational motion of free charges and rotational motion of bound charges. As the frequency of the exciting wave increases, losses with the conduction current σ becomes negligible compared with the losses $\epsilon^{''}$ due to dielectric damping.

Biological tissues have water content of around 70 % by mass [22]. At a driven frequency of 2.45 GHz significant heat is generated inside the tissue by friction of the vibrating dipole molecules. This effect is used in the food industry with microwave ovens and used in microwave thermal ablation for cancer treatment.

2.2 Antenna principles and waveguide

2.2.1 Dipole antenna

The main element of a microwave applicator is its distal radiating section which is a type of microwave antenna. The radiating section is located at the distal end of the coaxial wave guide placed in the tumour and radiates microwave energy into the tissue.

An antenna is an element of a circuit with a variable current distribution which emits or radiates electromagnetic waves in the desired medium making the transition between a guided and radiated wave. The applicator radiates microwaves in the medium and they are absorbed in the tissue.

To understand the radiating process, a simple filament with a sinusoidal current as shown in figure 2.1 is described. The magnetic vector potential in phasor form (sinusoidal form) is used to calculate the electric field radiated by the dipole.

The dipole has a sinusoidal charge variation; the current can be expressed in phasor form $\boldsymbol{I}$ as:

$$\boldsymbol{I} = j\omega\boldsymbol{q} \tag{2.41}$$

with ω the angular frequency and $\boldsymbol{q}$, the charge phasor. The length l of the dipole is assumed much smaller than the wavelength of the wave so that current is uniform and the phase independent of z coordinates. With polar coordinates, the magnetic vector potential in a point P with $r \gg l$ is [27]:

$$\boldsymbol{A}(r,\theta) = l\frac{\mu}{4\pi r}\boldsymbol{I}e^{-j\beta z}\boldsymbol{e}_z = \left(l\frac{\mu}{4\pi r}\boldsymbol{I}e^{-j\beta z}\right)(cos\theta\boldsymbol{e}_r - sin\theta\boldsymbol{e}_\theta) \tag{2.42}$$

with β the wave number of the medium or propagation constant. In the case of a microwave applicator the assumption $r \gg l$ can not be used because most of the electromagnetic

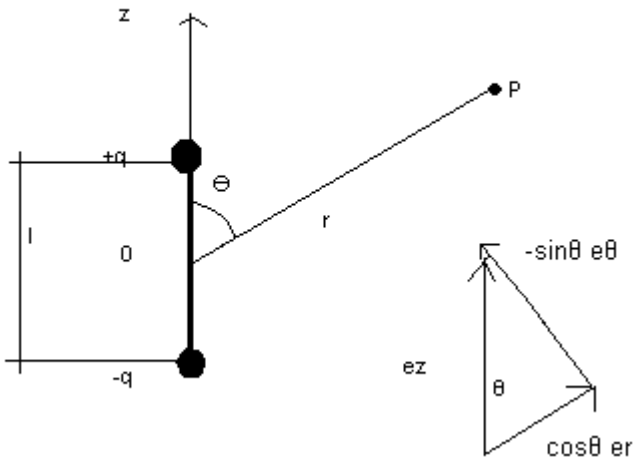

Figure 2.1: Dipole antenna of length l with a sinusoidal charge variation. The $\boldsymbol{e}_z$ vector is expressed in function of the radial $\boldsymbol{e}_r$ and tangential $\boldsymbol{e}_\theta$ direction

energy radiates from the ceramic antenna to the adjacent tissue closed to the antenna. However, analytical expressions of the electric vector cannot be obtained easily so the expression of the electric field far from a dipole is derived to understand the propagation mechanisms. By taking the curl of the magnetic potential, the magnetic field is obtained:

$$\boldsymbol{H} = \frac{1}{\mu}(\nabla \wedge \boldsymbol{A}) = \frac{jl\beta \boldsymbol{I}}{4\pi r}\left(1 + \frac{1}{j\beta r}\right)(sin\theta)e^{-j\beta r}\boldsymbol{e}_\phi \tag{2.43}$$

and by substituting the expression for the magnetic field 2.43 in Maxwell's equation 2.10 without the displacement current, the electric field is:

$$\begin{aligned} \boldsymbol{E} &= \frac{1}{j\omega\epsilon}(\nabla \wedge \boldsymbol{H}) \qquad (2.44) \\ &= l\sqrt{\frac{\mu}{\epsilon}}\frac{\boldsymbol{I}}{2\pi r^2}\left(1 + \frac{1}{j\beta r}\right)cos\theta e^{-j\beta r}\boldsymbol{e}_r + jl\sqrt{\frac{\mu}{\epsilon}}\frac{\boldsymbol{I}\beta}{4\pi r}\left(1 + \frac{1}{j\beta r} - \frac{1}{\beta^2 r^2}\right)sin\theta e^{-j\beta r}\boldsymbol{e}_\theta \end{aligned}$$

$\sqrt{\frac{\mu}{\epsilon}} = \eta$ is the intrinsic impedance of the medium. The field amplitude is a sinusoidal function and depends on the angle between the long axis of the wire and the point of observation. Depending on the value of the distance r, the terms $\frac{1}{r}$ and $\frac{1}{r^3}$ become dominant for respectively large and small values or distance r. These three terms are:
-terms in $\frac{1}{r}$ with slow decrease of electric field amplitude are radiating terms at long distances, this region is called the far field. This term is dominant for large value of r.
-terms in $\frac{1}{r^2}$ which are linked with induction phenomena.
-terms in $\frac{1}{r^3}$ are dominant for short distance and decrease in amplitude quickly with the distance.

In the far field region where $\beta r \gg 1$, the expression for the magnetic and electric field

can be reduced to:

$$\boldsymbol{H} = \frac{jl\beta \boldsymbol{I}}{4\pi r} sin\theta e^{-j\beta r} \boldsymbol{e}_\phi \tag{2.45}$$

$$\boldsymbol{E} = \frac{jl\eta\beta \boldsymbol{I}}{4\pi r} sin\theta e^{-j\beta r} \boldsymbol{e}_\theta \tag{2.46}$$

Equations 2.45 and 2.46 show that the electromagnetic field propagates in the radial direction and that only transverse components exist. The electric and magnetic fields are perpendicular to each other meaning that the wave is a transverse spherical electromagnetic wave [29]. The Poynting vector is real and only in the radial direction:

$$\boldsymbol{S} = \frac{I^2 l^2}{32\pi^2 r^2} \beta^2 \eta sin^2\theta \boldsymbol{e}_r \tag{2.47}$$

The power density decreases with r^2 and is radiated in the radial direction. Conservation of energy implies that the overall radiated power is independent of the distance. With an adequate design of the applicator, reflected power is minimized and most of the microwave energy is radiated into the tissue. The near field is encapsulated in the high permittivity ceramic of the radiating section of the applicator and the far field is in the tissue surrounding the applicator tip.

To know how a wave attenuates in a material, the penetration depth is defined as the distance where the amplitude is attenuated by a factor $\frac{1}{e}$.

2.2.2 Skin depth

For a wave propagating in the y direction, the magnitude of the field in the z direction attenuates as follows:

$$|E_z|(y) = E_0 e^{-\alpha y} \tag{2.48}$$

with E_0 the peak amplitude of the electric field and α the attenuation constant.

To measure how the wave attenuates in a medium, the penetration depth δ of the electric field is defined as the distance that the field has to traverse to achieve an attenuation of $\frac{1}{e}$. By definition of the skin depth, we have:

$$|E_z|(\delta) = E_0 e^{-\alpha\delta} = E_0 e^{-1} \tag{2.49}$$

hence, the skin depth δ is related to the attenuation constant α of the wave by:

$$\delta = \frac{1}{\alpha} \tag{2.50}$$

2.2.3 Coaxial wave guide

In the applicator described later in this thesis, the transport of microwave energy from the microwave source to the radiating section is made through two coaxial guides which

are composed of two conductors separated by a dielectric material. The first wave guide from the microwave output source to the applicator connector is a flexible coaxial cable with low electric losses. A connector connects the cable to the smaller semi rigid coaxial cable of the applicator. Electromagnetic waves propagate between these two conductors and different modes of propagation exist for different frequencies. At 2.45 GHz, it is the fundamental mode (transverse electromagnetic wave) that propagates.

It is possible to know the propagating mode and expression of the electric field by solving Maxwell's equation with appropriate boundary conditions [14].

Four important parameters for choosing a wave guide are: the operating frequency band which will determine the geometry, the dielectric material between the inner and outer conductor of the wave guide, the amount of power to be transferred, and the amount of losses that are expected [57].

2.3 Equation of heat conduction

In microwave hyperthermia, the microwaves are the source of heat and the process of heating a tissue is by direct heating from the microwave field, heat conduction through the tissue and heat transport via internal fluid such as water and blood.

To have a better understanding of the heat transfer by conduction, it is useful to consider the heat transfer conduction equation in cartesian, cylindrical and spherical coordinates. To simplify calculation the assumption of the conduction in only one direction is often realistic for a cylindrical or spherical geometry, because the heat transfer in the other directions can be assumed to be very small compared to the direction of the main heat flux (for example a spherical heat source or a long cylinder).

For a given volume of a solid as shown in figure 2.2, conservation of energy states that the rate of energy storage $\dot{E}_{st}$ inside the volume is equal to the rate of inflow energy $\dot{E}_{in}$ minus the rate of outflow energy $\dot{E}_{out}$ plus the rate of energy generated inside the solid $\dot{E}_{gen}$ [36].

$$\dot{E}_{st} = \dot{E}_{in} - \dot{E}_{out} + \dot{E}_{gen} \tag{2.51}$$

In the case of microwave heating, the energy generation inside the volume is due to the microwave field. The energy storage is related to the temperature by the density and specific heat of the tissue. The inflow and outflow energy are related to the gradient of the temperature and the thermal conductivity of the material.

For an infinitesimal control volume $dxdydz$ the conservation of energy is applied to obtain a differential equation.

$$\dot{E}_{st} = q_x + q_y + q_z - (q_{x+dx} + q_{y+dy} + q_{z+dz}) + \dot{e}_{gen} dxdydz \tag{2.52}$$

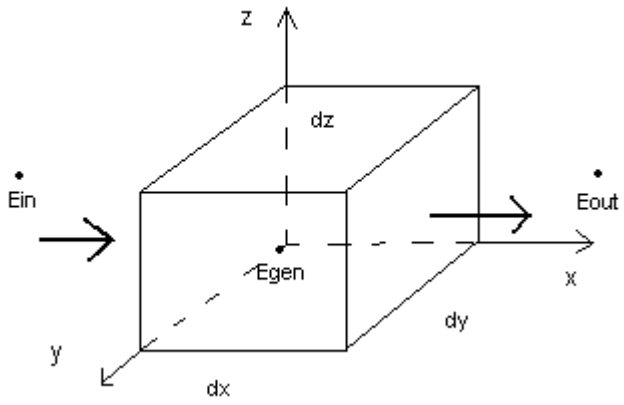

Figure 2.2: Infinitesimal volume dxdydz used to write the energy balance. $\dot{E}_{gen}$ is the power generated inside the volume, $\dot{E}_{in}$ and $\dot{E}_{out}$ are the input and output power

with $\dot{e}_{gen}$ $[Wm^{-3}]$ the heat generated in the volume. q_x, q_y, q_z are the heat flux in the x, y and z direction respectively on faces $x = 0$, $y = 0$ and $z = 0$ of the control volume. Similarly, q_{x+dx}, q_{y+dy}, q_{z+dz} are the heat flux in the the x, y and z direction respectively on faces $x = 0 + dx$, $y = 0 + dy$ and $z = 0 + dz$ of the control volume. The heat flux in x+dx is:

$$q_{x+dx} = q_x + \frac{\partial q_x}{\partial x} dx \tag{2.53}$$

for a homogenous and isotropic material with constant thermal properties, from Fourier's law the heat flux is directly proportional to the gradient of temperature on each face of the infinitesimal volume

$$q_x = -k \frac{\partial T}{\partial x} dydz \tag{2.54}$$

$$q_y = -k \frac{\partial T}{\partial y} dxdz \tag{2.55}$$

$$q_z = -k \frac{\partial T}{\partial z} dxdy \tag{2.56}$$

$$\tag{2.57}$$

with $k[WK^{-1}m^{-1}]$ the thermal conductivity of the material and T the temperature at the given location.

The storage energy $\dot{E}_{st}$ varies with time and is expressed as a function of rate of temperature change and the specific heat capacity $C[Jkg^{-1}K^{-1}]$ and density $\rho[kgm^{-3}]$.

$$\dot{E}_{st} = \rho C \frac{\partial T}{\partial t} \tag{2.58}$$

Hence, conservation of energy for an infinitesimal volume dxdydz gives:

$$\rho C \frac{\partial T}{\partial t} = \frac{\partial}{\partial x}\left(k \frac{\partial T}{\partial x}\right) + \frac{\partial}{\partial y}\left(k \frac{\partial T}{\partial y}\right) + \frac{\partial}{\partial z}\left(k \frac{\partial T}{\partial z}\right) + \dot{e}_{gen} \tag{2.59}$$

With the divergence operator the equation of conduction is:

$$\rho C \frac{\partial T}{\partial t} = \nabla \cdot (k \nabla T) + \dot{e}_{gen} \tag{2.60}$$

In cylindrical coordinates the equation of heat conduction with constant thermal conductivity k in the radial direction becomes:

$$\rho C \frac{\partial T}{\partial t} = \frac{k}{r} \frac{\partial}{\partial r} \left(r \frac{\partial T}{\partial r} \right) + \dot{e}_{gen} \tag{2.61}$$

In spherical coordinates the equation of heat conduction in the radial direction is:

$$\rho C \frac{\partial T}{\partial t} = \frac{k}{r^2} \frac{\partial}{\partial r} \left(r^2 \frac{\partial T}{\partial r} \right) + \dot{e}_{gen} \tag{2.62}$$

The term $\dot{e}_{gen}$ is the source of heat coming from the vibration and friction of dipole molecules due to the driving electromagnetic field in the case of microwave heating. The time average power dissipated in a homogenous and isotropic material per unit volume is:

$$\dot{e}_{gen} = \frac{1}{2} \omega \left(\epsilon^{''} + \frac{\sigma}{\omega} \right) |\mathbf{E}|^2 \tag{2.63}$$

$$= \frac{1}{2} (\omega \epsilon^{''} + \sigma) |\mathbf{E}|^2 \tag{2.64}$$

$$= \frac{1}{2} \omega \epsilon^{'} tan\, \delta |\mathbf{E}|^2 \tag{2.65}$$

with $\mathbf{E}$ the complex amplitude of the microwave electric field and $||$ is the modulus of the complex number. $\epsilon^{''}$ is the imaginary part of the complex permittivity and ω the angular frequency of the microwave field. σ is the electrical conductivity of the material. The last equation is obtain by using the definition of the loss tangent (equation 2.40). The dissipated power is often defined as a function of the real part $\epsilon^{'}$ of the permittivity and the loss tangent $tan\, \delta$.

2.4 Heat transfer in fluids

In addition to heat generation and heat transport in tissue, this project involves the cooling of the applicator itself by flowing gas. We therefore also need to consider the problem of heat transfer in fluids.

Heat transfer through a fluid involves the thermal properties of the fluid and the fluid velocity field. To obtain the temperature field in a fluid domain, the fluid solution needs to be obtained first. For the following example, the annular flow geometry has been chosen as an application of the cooling circuit used later for the construction of the gas cooled applicators.

Figure 2.3: Parabolic profile of velocity in an annular channel for a laminar flow

2.4.1 Fluid in an annular geometry

A fluid regime can be laminar or turbulent depending on the geometry and the velocity of the fluid. The regime can be determined with the Reynolds number by knowing a characteristic length of the geometry and a characteristic velocity of the fluid. In the laminar flow regime the flow can be seen as very thin concentric layers which slide past each other in an axial direction [31]. For this laminar flow, heat will only be transferred, apart from radiation, by thermal conduction in the flow especially in the direction perpendicular to the flow.

For turbulent flow, the fluctuation of velocity and the mixing motion of fluid considerably enhanced the heat transfer between the fluid and the wall of the tube. Transition from laminar to turbulent flow occurs when velocity reaches the critical Reynolds number. Its lowest value ($Re = 2300$) occurred for an agitated and perturbed inlet condition for a tube geometry [37]. For other cases the critical Reynolds had typical values between 3000 or 4000 or even higher [31].

A gas can also be considered as an incompressible fluid at low velocity. At higher velocity, the compressibility effect has to be taken into account. The ratio between the velocity and the local speed of sound allows us to decide whether or not the gas can be assumed incompressible. This ratio is called the Mach number. In our case, the gas flow can be considered incompressible if this ratio is lower than 0.5. Typical values for Mach number were $M = \frac{140}{340} = 0.41$ with a $140\,ms^{-1}$ input velocity corresponding to $5\,lmin^{-1}$ flow rate. Calculation showed that the difference on the stagnation pressure (the stagnation pressure on a streamline is where the velocity is 0) is less than 1 % if $M \leq 0.2$ between an incompressible and compressible gas. The difference between incompressible and compressible gas on the stagnation pressure is less than 10 % if $M \leq 0.6$ [67].

For simple geometries and using some assumptions on the flow regime, it is possible to calculate the temperature in the fluid along the direction of travel by solving the energy equation. The classical problem of determining the mean temperature of a fluid moving on a plate at a constant temperature is called the Graetz problem [25].

To understand the problem of heat transfer in an annular cylinder, it is instructive to

examine the fluid equation and energy equation. The Navier Stokes equations govern the behaviour of a fluid by describing the relationship between the velocity field, the pressure drop, the external forces and the dissipation term due to the fluid friction. Navier Stokes equations in cylindrical coordinates for an incompressible fluid with constant viscosity are given in Appendix A.

By solving the Navier Stokes equations for a one dimensional steady incompressible laminar flow with constant viscosity and velocity function only in the radial direction, the equation obtained from Appendix A after simplification is:

$$\frac{1}{r}\frac{d}{dr}\left(r\frac{dv_z}{dr}\right) = \frac{1}{\mu}\frac{dp}{dz} \tag{2.66}$$

r is the radial variable, v_z is the velocity in the z direction, p[Pa] is the pressure and $\mu[kgs^{-1}m^{-1}]$ the viscosity of the fluid. The boundary conditions at the inner and outer wall of the annular flow are: $v_z(r_i) = v_z(r_o) = 0$. The velocity profile obtained for the fluid between two cylinders of inner radius r_i and outer radius r_o is:

$$v_z(r) = \frac{1}{4\mu}\frac{dp}{dz}\left(r^2 - r_i^2\right) + \frac{1}{4\mu}\frac{dp}{dz}\left(r_0^2 - r_i^2\right)\frac{(\ln r_i - \ln r)}{\ln\left(\frac{r_0}{r_i}\right)} \tag{2.67}$$

The parabolic velocity profile in a concentric annular duct was already found in textbooks from Wien [81] and Lamb [45] is shown in figure 2.3. In the appendix A, it is shown that for an annular laminar flow, the pressure drop is given by the equation 2.68:

$$\frac{dp}{dz} = -\frac{8\mu \ln k v_m}{r_0^2[\ln k(1+k^2) + 1 - k^2]} \tag{2.68}$$

with $k = \frac{r_i}{r_o}$ the ratio of the inner and outer radius of the annular channel and v_m the mean velocity. The pressure drop is a function of the ratio of the inner and outer radius of the annular duct, the mean velocity and the viscosity of the fluid. For constant geometry of tube and constant viscosity, the pressure gradient is a linear function of the mean velocity of the fluid. The volume flow rate $\dot{V}$ is related to the mean velocity v_m by:

$$v_m = \frac{\dot{V}}{\pi(r_0^2 - r_i^2)} = \frac{\dot{V} r_0^2}{\pi(1-k^2)} \tag{2.69}$$

The pressure drop in function of the flow rate is:

$$\frac{dp}{dz} = -\frac{8\mu \ln k \dot{V}}{[\ln k(1+k^2) + 1 - k^2][\pi(1-k^2)]} \tag{2.70}$$

The pressure drop for a flow rate of 5 $lmin^{-1}$ was 2.8 bars with a 2D axisymmetric finite element model and the pressure drop calculated using equation 2.70 was 2.71 bars. To know the pressure drop required to sustain an internal flow the friction factor is a convenient dimensionless parameter:

$$f = -\frac{\frac{dp}{dx}D}{\rho\frac{u_m^2}{2}} \tag{2.71}$$

it is defined as the pressure drop over the kinetic energy of the fluid with D the internal diameter of the tube. For turbulent flow and a non smooth tube, it can be obtained experimentally for different relative roughness of tube and plotted in function of Reynolds number in a Moody diagram [52]. In this diagram, the friction factor of the tube is plotted in function of the Reynolds number and the relative roughness of the tube. The friction factor is a useful parameter and can be used to determine the power required for a pump in a fluid engineering application for example.

2.4.2 Thermal conduction in fluids

To obtain the temperature field, the conservation of energy is expressed for a fluid particle or a volume of fluid in the general case [60]:

$$\frac{De}{Dt} + p\frac{D}{Dt}\frac{1}{\rho} = \frac{1}{\rho}\phi - \frac{1}{\rho}\nabla \cdot \boldsymbol{q} = \frac{1}{\rho}\phi + \frac{1}{\rho}\nabla \cdot (k\nabla T) \tag{2.72}$$

Capital letter D is the total derivative, e is the internal energy of the fluid particle, ρ is the density of the fluid, $\boldsymbol{q}$ is the heat flux which is expressed as a function of the thermal conductivity k and the temperature gradient with Fourrier law. $\phi = \boldsymbol{\tau} : \nabla(\vec{v})$ is the dissipation term with $\boldsymbol{\tau}$ the stress tensor defined by:

$$\boldsymbol{\tau} = \begin{pmatrix} \sigma_{xx} & \tau_{xy} & \tau_{xz} \\ \tau_{yx} & \sigma_{yy} & \tau_{yz} \\ \tau_{zx} & \tau_{zy} & \sigma_{zz} \end{pmatrix} \tag{2.73}$$

with σ_{ij}, $i = x, y, z$, $j = x, y, z$ the stress component of a fluid particle in the i direction located on the face $j = 0$ of a infinitesimal control volume. σ_{xx}, σ_{yy}, σ_{zz} are the normal stress components and σ_{ij} with $i \neq j$ the tangential stress components of a fluid particle.

The velocity tensor defined by:

$$\nabla(\vec{v}) = \begin{pmatrix} \frac{\partial v_x}{\partial x} & \frac{\partial v_y}{\partial x} & \frac{\partial v_z}{\partial x} \\ \frac{\partial v_x}{\partial y} & \frac{\partial v_y}{\partial y} & \frac{\partial v_z}{\partial y} \\ \frac{\partial v_x}{\partial z} & \frac{\partial v_y}{\partial z} & \frac{\partial v_z}{\partial z} \end{pmatrix} \tag{2.74}$$

with v_x, v_y, v_z are the components of the velocity vector $\boldsymbol{v}$. Terms on the left of the energy equation gives the variation of internal energy and mechanical energy per unit mass and time. On the right side, the variation of heat is given by the dissipation term from shearing stress and heat transferred by conduction to the fluid particle. The shearing stress components are equals to the viscosity times the derivative of the velocity v_z over the tangential direction r.

If the velocity is zero, equation 2.72 becomes the equation of heat conduction for a fluid at rest. The heat propagates in the fluid is like a solid with the same thermal properties. The equation of energy becomes in the case of a fluid at rest:

$$\rho\frac{\partial e}{\partial t} = -\nabla \cdot \boldsymbol{q} \tag{2.75}$$

In the case of an incompressible steady flow regime, the total derivative of energy becomes with the internal energy expressed in function of temperature $e = C_p T$ with C_p the specific heat capacity of the fluid:

$$\frac{De}{Dt} = \frac{\partial e}{\partial t} + \boldsymbol{v} \cdot \ \nabla e \tag{2.76}$$

The second term of equation 2.76 is an advection term where energy is transported with the fluid velocity field, the equation energy 2.72 becomes:

$$\rho\, C_p\, \boldsymbol{v} \cdot \nabla T = \phi + \nabla \cdot (k \nabla T) \tag{2.77}$$

The equation is detailed below for the fluid flowing in the z direction, in a steady state regime for an incompressible fluid with constant viscosity. The dissipation term is the product of the stress tensor τ and the velocity tensor $\nabla(\boldsymbol{v})$ [61].

For a one-dimensional fluid moving in the z direction, the stress tensor in cylindrical coordinates is:

$$\boldsymbol{\tau} = \begin{pmatrix} 0 & \mu \frac{\partial v_z}{\partial r} & 0 \\ \mu \frac{\partial v_z}{\partial r} & 0 & 0 \\ 0 & 0 & 0 \end{pmatrix} \tag{2.78}$$

and the gradient of velocity is:

$$\nabla(\boldsymbol{v}) = \begin{pmatrix} 0 & \frac{\partial v_z}{\partial r} & 0 \\ 0 & 0 & 0 \\ 0 & 0 & 0 \end{pmatrix} \tag{2.79}$$

The product of these two tensors gives for the dissipation term

$$\phi = \mu \left(\frac{\partial v_z}{\partial r} \right)^2$$

with μ the viscosity of the fluid.

For fluid flowing in a tube, the temperature is only a function of z and r coordinates. The thermal fluid equation for an ideal gas of thermal conductivity k obtained from the energy equation 2.72 is:

$$\rho\, C_p\, v_z \frac{\partial T}{\partial z} = \mu \left(\frac{\partial v_z}{\partial r} \right)^2 + k \left(\frac{\partial^2 T}{\partial^2 z} + \frac{1}{r} \frac{\partial}{\partial r} \left(r \frac{\partial T}{\partial r} \right) \right) \tag{2.80}$$

The field velocity is known from the previous calculation from equation 2.67 in an annular duct made in appendix A and temperature is the unknown. The term of viscous dissipation is neglected because for low velocity flow, the heat generated by fluid friction is much lower than the heat flux coming from a temperature gradient between the fluid and the wall. With $\alpha = \frac{k}{\rho C_p}$ the thermal diffusivity of the fluid, the equation 2.80 is reduced to :

$$v_z \frac{\partial T}{\partial z} = \alpha \left(\frac{\partial^2 T}{\partial^2 z} + \frac{1}{r} \frac{\partial}{\partial r} \left(r \frac{\partial T}{\partial r} \right) \right) \tag{2.81}$$

This equation can be scaled in terms of non dimensional variables. This is useful for making assumptions and potentially neglecting some terms. New variables are defined by: $\xi = \frac{z}{r_0 Pe}$, $\eta = \frac{r}{r_0}$, $v_\xi = \frac{v_z(r)}{v_0}$, $Pe = \frac{\rho C_p v_0 r_0}{k} = \frac{r_0 v_0}{\alpha}$, $\theta = \frac{T - T_w}{T_0 - T_w}$. With v_0 the maximal velocity and k the thermal conductivity of the fluid, T_w is the temperature of the inner wall and T_0 is the inlet temperature of the fluid. In dimensionless form, the one dimensional equation of energy becomes:

$$v_\xi(\eta)\frac{\partial\theta}{\partial\xi} = \frac{1}{\eta}\frac{\partial}{\partial\eta}\left(\eta\frac{\partial\theta}{\partial\eta}\right) + \frac{1}{Pe^2}\frac{\partial^2\theta}{\partial^2\xi} \tag{2.82}$$

Davies [17] developed several solutions of convective diffusion problems with axial conduction with the confluent hypergeometric function. The Peclet number Pe is the ratio between the rate of energy transported by convection and the rate of energy transport by conduction inside the fluid. The Peclet number is directly proportionnal to fluid velocity. $Pe = Re \times Pr$ with Re the Reynold number defined by: $Re = \frac{\rho V L}{\mu}$ which can be interpreted as the ratio of inertia to viscous forces. Pr is the Prandtl number defined by $Pr = \frac{C_p \mu}{k}$ which is the ratio of momentum and thermal diffusivities. Axial conduction can be neglected if $Pe \geq 100$. For a flow rate of $5\, lmin^{-1}$ at room temperature of air the average velocity at the entrance of the channel is $140\, ms^{-1}$. The Peclet number is: $Pe = Re \times Pr = 1771 \times 0.7 = 1239$. This renders the last term in equation 2.82 negligible which means that axial conduction inside the fluid in the direction z of the moving fluid can be neglected. The equation of energy becomes:

$$v_\xi\frac{\partial\theta}{\partial\xi} = \frac{1}{\eta}\frac{\partial}{\partial\eta}\left(\eta\frac{\partial\theta}{\partial\eta}\right) \tag{2.83}$$

This equation gives a relationship between the variation of temperature along the z axis and the variation of temperature in the radial direction for a given velocity field. From equation 2.83, as the velocity (or flow rate) increases the gradient of temperature in the axial z direction decreases. The temperature field $T(r,z)+T_0$ is also a solution of equation 2.83, it means that for this problem, the inital temperature of the fluid does not modify the shape of the temperature profile for an adiabatic boundary condition. This equation can be solved by a method of separation of the variables and an orthogonal expansion technique [34].

For each channel, the velocity field needs to be calculated and then inserted in the equation 2.83.

For two counter annular flows separated by a tube of a small thickness, two equations of the form 2.83 need to be solved with appropriate boundary conditions to obtain the temperature field through the whole geometry. On the wall of the outside tube, the adiabatic condition can be used for simplification. At the center of the tube, the adiabatic condition is used because the geometry is axisymmetric so there is no heat flux in the center line. At the interface represented by a thin copper tube, the heat flux is continuous.

For complex geometries like a counter annular flow, numerical techniques are well adapted to solve the energy equation. For our cooling circuit, the use of a finite element package was chosen to solve the energy equation and obtain the temperature field for both the fluid and solid part of the applicator. By using a specific fluid element incorporating the energy equation, a finite element package allows solving the energy equation for both the fluid and solid part of the model. The purpose of this finite element model is to test for different input temperatures and flow rates and to improve the geometrical design. Modelled temperatures obtained with this finite element package for different configurations are described in chapter 5.

Chapter 3

5 mm water cooled microwave applicator

3.1 Introduction

In this chapter, a 5 mm in diameter microwave applicator is presented. This applicator is designed to be used with open surgery or laparoscopic procedure.

In general, three types of surgery are used to remove or destroy tumour cells, they are presented in the order from the most invasive to the least invasive procedure.

The older and most used operative mode of surgery is open surgery. This surgery is done through a large incision with traditional instruments. It is invasive but flexible with direct access to the organ. In cancer therapy open surgery has the best outcomes for survival rates because it minimizes the possibility of local recurrence. But for some old or weak patients the open surgery method is too risky because of the trauma associated with the operation which can lead to complications such as excessive bleeding.

Laparoscopic surgery is surgery done using instruments with a limited diameter inserted through holes in the abdominal wall from 5 mm to 10 mm diameter. The use of a laparoscope (surgical telescope) allows the surgeon to operate with the instruments. This surgery is less invasive but less flexible than open surgery. The surgeon needs to have the skills to manipulate the instruments through the skin. It is sometimes the only method available to operate on weak patients.

The last kind of surgery is carried out with the use of a device inserted directly into the tissue, for example a radiofrequency probe or microwave applicator. This procedure is called percutaneous surgery or interventional radiology. It is far less invasive than open surgery. To be effective the device needs to be placed in the correct position to be sure to treat the tumour. An imaging system such as a CT scanner is usually used to help to place the device inside the tumour of the organ.

Because the cooling circuit is not closed and water is released into the tissue, the applicator is also called an open loop cooled applicator. This applicator is used with the laparoscopic technique to ablate liver tumours from 4 to 8 cm diameter at high power and in a short time. The structure of the chapter follows the development phases of this laparoscopic microwave applicator. Firstly, the laparoscopic procedure which gives some constraints and specifications required for the applicator is examined. Then, the applicator design itself is explained. Finally, the applicator performances were tested in order to check that the specifications were filled.

3.2 The laparoscopic technique

The procedure is performed via three trocar ports as shown in figure 3.1. Typically one of the ports carries a camera. The second port is used to introduce a light source. The third port is used to insert the operating instrument, a microwave applicator in our case. In this methodology for liver treatment, the abdomen is inflated using CO_2 gas in order to add space between organs and facilitate the manipulation of the instruments on the target organ.

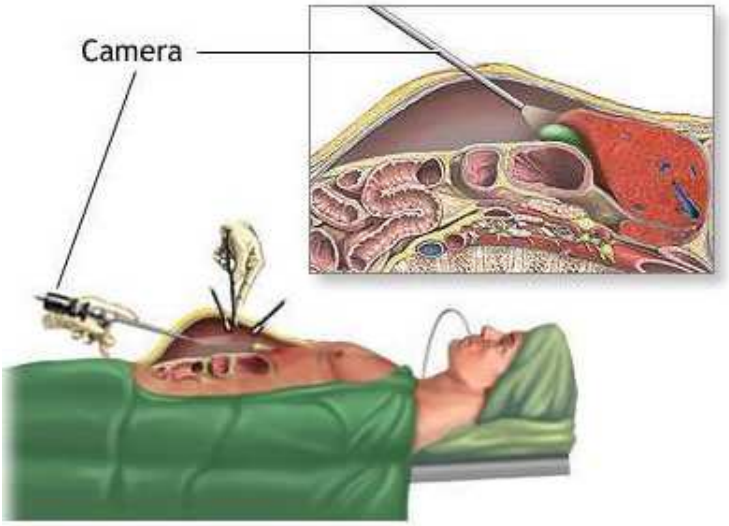

Figure 3.1: Schematic of a laparoscopic procedure with three ports in an inflated abdomen for easy access to an internal organ [78]

3.3 Specifications

The use of the laparoscopic method places certain design restrictions on any applicators we may design. These are:
a) Diameter no greater than 10 mm through the trocar.
b) Length at least 30 cm to have access to the organ in an inflated abdomen.
c) A sharp cutting tip is required to enter the organ and the tumour without excessive force.
d) The temperature of the shaft needs to be not too hot to avoid burns of the normal tissue surrounding the trocar tube.

Studies show that the size of the tumour is an important factor determining the local recurence rate [53]. Larger tumours may be more difficult to treat with a one centimetre margin of normal tissue because of the limited volume of tissue that can be ablated. When more then one treatment is needed to ablate a tumour, higher risk of local reccurence has been described [1].

The use of high power to ablate large tumours up to 8 cm in one session with a safe margin of 1 cm of normal tissue is definately an advantage and minimizes the risk of local recurence. This means that the applicator must be capable of delivering a power of 100 to 200 watts at 2.45 GHz. This is based on the work performed by Swift *et al* [70] where porcine liver ablations have been performed at 100 and 150 watts to treat lesions up to 6 cm in diameter in 3 minutes. Design parameters are summarised in figure 3.2.

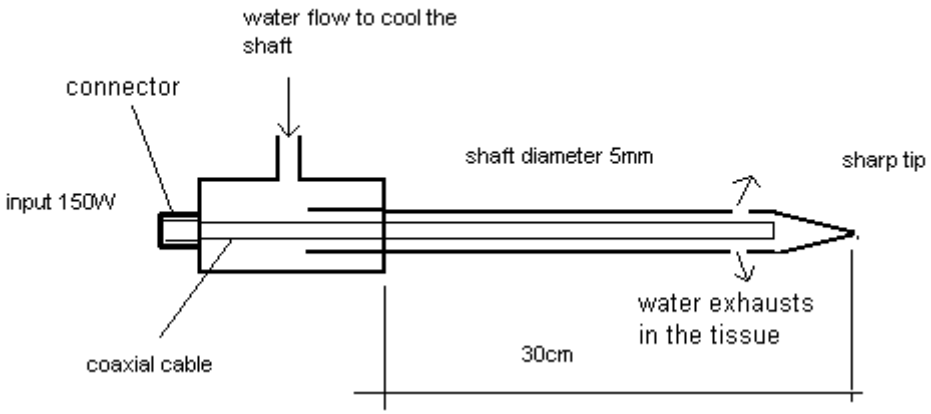

Figure 3.2: Specifications for a laparoscopic 5 mm applicator

3.4 Applicator design

3.4.1 Principle of operation

The applicator is the interface between the coaxial cable and the tissue, it transmits energy into a local domain, the tumour. This process of transmitting the microwave energy is achieved by a modified dipole antenna which radiates microwaves into the tissue.

The particular design of the radiating dipole antenna adopted is shown in figure 3.3. This choice of antenna occurred from the need to perform spherical ablation and the simplicity of the design. The design utilizes a form of folded dipole radiator. The two halves of the dipole are formed by a length of stripped cable, approximately a quarter of wavelength of microwaves at 2.45 GHz in air in length and a section of the outer conductor of the cable also approximately a quarter wavelength in length. Both elements are encapsulated in a ceramic trocar cutting tip.

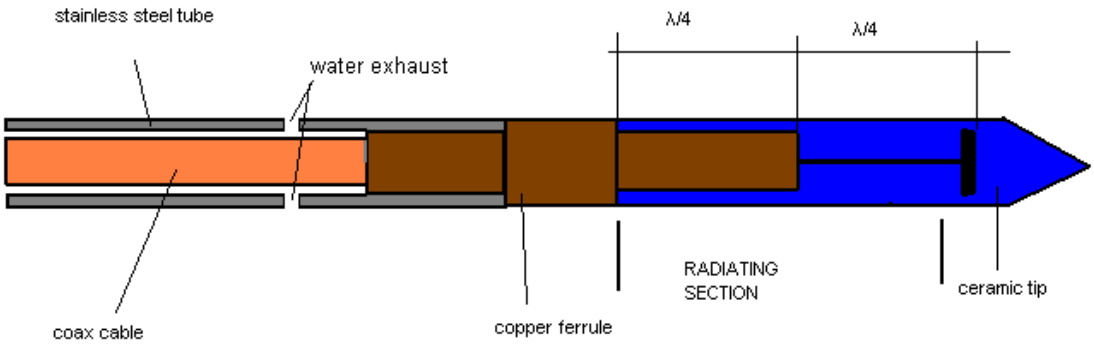

Figure 3.3: Diagram of the radiating section with shaft, coaxial cable, copper ferrule, ceramic tip and washer. The two branches of the dipole have the length of a quarter of wavelength in air at 2.45 GHz

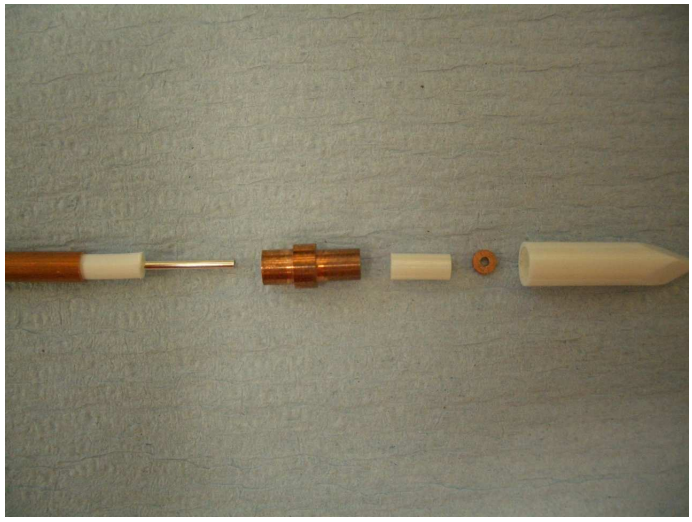

Figure 3.4: Components of the radiating section of the 5 mm applicator, coax, copper ferrule, ceramic cylinder, washer and ceramic tip

The ceramic selected was an yttrium stabilised tetragonal zirconia polycrystalline with the trade name of Technox 2000®. Zirconia is also a good low loss material ceramic with a relative permittivity of $\epsilon_r = 20$ which shortens the required lengths of the dipole elements. Because the ceramic is a low loss material with high permittivity, it is not directly heated by the microwaves and is adequate to effectively transmit the microwave energy into the tissue.

The washer is a tuner element which is used to improve the match between the antenna and the tissue. Its effects on the design is to shorten the length of the radiating section.

The mechanical properties and robustness of the ceramic enable a very thin sharp tip to be formed and facilitate the insertion into the tissue.

In order to maintain the shaft of the applicator below a temperature safety limit of 42 °C, water flows in the annular interspace between the coaxial cable and the stainless steel shaft. The water drains into the organ of the patient by four small holes located in the end of the shaft near the ceramic tip.

3.4.2 Geometry

The semi rigid coaxial cable has an inner and outer diameter of 3 mm and 3.6 mm respectively. It is made of two copper conductors insulated by a PTFE dielectric. Microwave energy propagates along this coaxial cable from the connector to the radiating section.

The copper ferrule, which is basically a copper tube, fits on to the coaxial cable on one end and fits into the ceramic on the other end. It forms one of the branches of the dipole antenna and it is directly connected to the ceramic tip. It also has a mechanical function

by being the mechanical joint between the shaft, the coaxial cable and the ceramic tip.

The extremity of the centre conductor is inserted in a ceramic cylinder which fits into the ceramic tip and is located in the centre of the radiating section. The low loss and high permittivity ceramic material allows an efficient transmission of the microwave energy into the tissue.

The washer, which is a small copper ring soldered at the end of the center conductor, is a tuner element acting like a reflector for the microwaves and is useful to shorten the length of the radiating section.

The ceramic tip is a hollow cylinder with a sharp trocar end to penetrate the tissue. It encapsulates the ceramic cylinder, the washer and partially the copper ferrule. A picture of the components is shown in figure 3.4.

The non radiating elements are the stainless steel shaft and the handle. These components are shown in figure 3.5 in the built applicator. The shaft is a stainless steel 316 grade tube that confers a good stiffness and solidity.

The handle is basically a tube that provides a mechanical connection between the shaft and the coaxial cable. It is ergonomic because the surgeon manipulates the applicator by the handle. It is also a chamber with the input port for the water that flows in the annular inter space between the coaxial cable and the shaft.

The working part of the applicator is the radiating section which is an assembly of five elements with specific dimensions obtained with a finite element model at the driven frequency of 2.45 GHz.

Figure 3.5: Components of the 5 mm laparoscopic applicator. From top to bottom, the handle, the coaxial cable with the radiating section components, the stainless steel shaft, and the built applicator

3.4.3 Electromagnetic model with HFSS

HFSS® (High Frequency Structure Simulator) is a finite element software package for electromagnetic analysis produced by Ansoft Corporation. The principle of the finite element method is to reduce a continuous in time and space equation of equilibrium into a linear equation discrete in time and space that can be solved by using classical methods of numerical analysis. The finite element method is examined in more detail in appendix C. With this software the electromagnetic field of a given configuration can be calculated.

By choosing specific lengths with the help of a finite element Software such as HFSS for electromagnetic analysis, it is possible to design an effective radiating tip.

HFSS allows running a parametric analysis in which critical lengths are set as parameters and the simulation performed for each combination. Then the optimal geometry can be determined for the driving frequency of 2.45 GHz. Following a parametric optimization with HFSS software, dimensions of the applicator components in table 3.1 associated with figure 3.6 were derived. As shown in figure 3.6, the two most important lengths are the lengths l_2 and h_1 of the branches of the dipole antenna. They are approximately a quarter of a wavelength length.

The HFSS model includes an air gap between the center conductor and the ceramic of dimension e, between the ceramic tip and the ceramic cylinder of dimension e_2 and between the ceramic and the washer with the dimension e_4. These air gaps were obtained

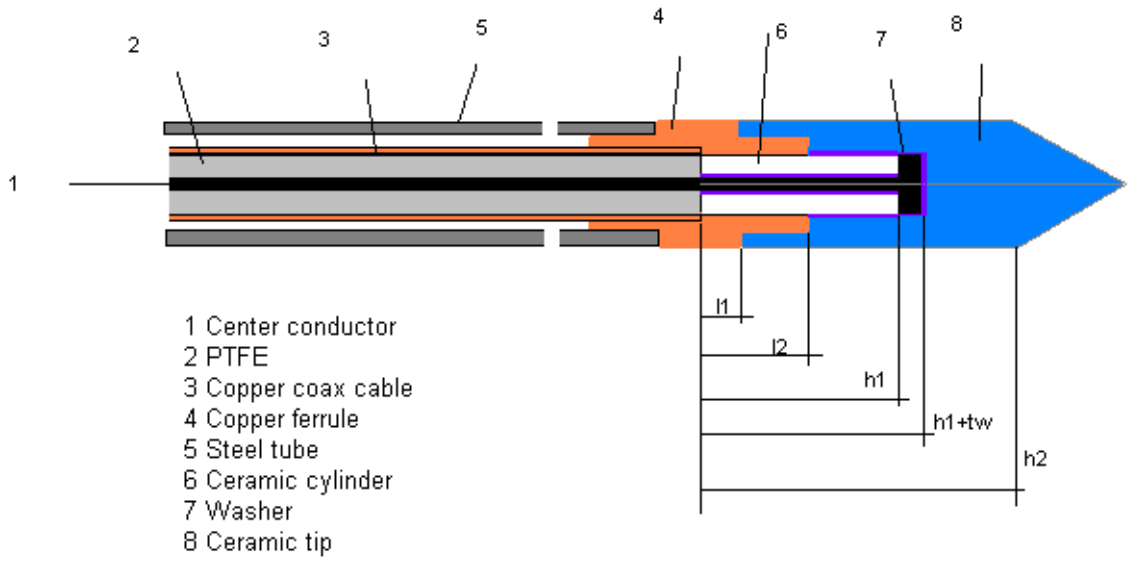

Figure 3.6: Dimensions of the 5 mm applicator radiating section. Length h1 and l2 are branches of the antenna which are the most critical for the electromagnetic design

from the machining tolerances. They have to be included in the model to give more accurate prediction of the electric field distribution and $|S_{11}|$ parameter.

Dimensions	[mm]
Radius center conductor	0.512
Radius dielectric	1.492
Radius coax cable	1.7905
Radius shaft	2.5
Radius washer	1.4
l1	8
l2	14
h1	24
h2	26
tw	0.5
e air gap center	0.02, 0.06, 0.1
e2 air gap cylinder	0.04, 0.07, 0.1
e4 air gap washer	0.1, 0.4, 0.7

Table 3.1: Dimensions of the 5 mm applicator obtained with a parametric analysis with HFSS model

3.4.3.1 Return loss

For high frequency circuits, a convenient form to express the relationship between the incident wave and reflected wave for a multi input multi output circuit is a matrix of reflection coefficients. S parameters are voltage wave ratios corresponding to reflection and transmission coefficient. When the signals are normalized by the square root of the characteristic impedance of the line, the matrix becomes the scattering matrix. For example for a four port circuit with two inputs and two outputs, S parameters are defined by [58]:

$$\begin{aligned} S_{11} &= \rho_{11} \\ S_{12} &= \tau_{12}\frac{\sqrt{Z_{c2}}}{\sqrt{Z_{c1}}} \\ S_{21} &= \tau_{21}\frac{\sqrt{Z_{c1}}}{\sqrt{Z_{c2}}} \\ S_{22} &= \rho_{22} \end{aligned} \tag{3.1}$$

where ρ_{ij} are reflections and τ_{ij} transmissions located at port j for an input wave sent to port i. Z_{c1} and Z_{c2} are the characteristic impedances of lines 1 and 2. The magnitude of the reflection coefficient or S_{11} referred to above is the ratio between the amplitude of the reflected wave and the amplitude of the incident wave on a single input/output system [28].

The incident power and reflected power on a line can be expressed in terms of voltage and characteristic impedance by:

$$\begin{aligned} P_{in} &= \frac{1}{2}\frac{V_{in}^2}{Z_0} \\ P_{refl} &= \frac{1}{2}\frac{V_{refl}^2}{Z_0} \end{aligned} \tag{3.2}$$

Hence, the ratio of reflected and incident power is equal to the square of the S_{11} magnitude:

$$\frac{P_{refl}}{P_{inc}} = \frac{V_{refl}^2}{V_{inc}^2} = |S_{11}|^2 \tag{3.3}$$

by definition of the S_{11} parameter which is the ratio between the reflected and incident voltage wave. The magnitude of the return loss parameter can be defined by the ratio between the reflected power and incident power. In decibels the magnitude of the return loss is:

$$RL[dB] = 10\,log\left(\frac{P_{refl}}{P_{inc}}\right) = 10\,log\left(|S_{11}|^2\right) = 20\,log\left(|S_{11}|\right) \tag{3.4}$$

For example, a return loss of -10 dB means that the ratio between the reflected power and the input power is equal to 0.1. In other words, 90 % of the input power is transmitted to the load. For the applicator design, a match typically lower than -10 dB is required to avoid too much reflected power which would decrease the heating performance of the applicator and heat the coaxial cable.

3.4.3.2 Electromagnetic field

HFSS finite element software allows us to perform an electromagnetic analysis and graphically display the results. The electromagnetic analysis is essential in the design of the applicator and allows especially:
- the visualization of the shape of the electric field distribution.
- to check for any excessive high field regions in the tissue.
- to run a parametric analysis to choose the dimensions of the radiating antenna that minimize the reflected power (or minimize $|S_{11}|$).
- to test different materials by changing the value of the loss tangent and electrical permittivity of the material.
- to design an antenna which has a return loss not too sensitive to the variation of frequency around the operating frequency in order maintain a good transmission of energy in the tissue during the dessication process of a thermal ablation.

The time averaged magnitude of the electric field for the design is shown in figure 3.7. The input power on the port of the coaxial cable is 1 watt and the frequency is 2.45 GHz. The domains with high electric field (in red in figure 3.7) are concentrated between

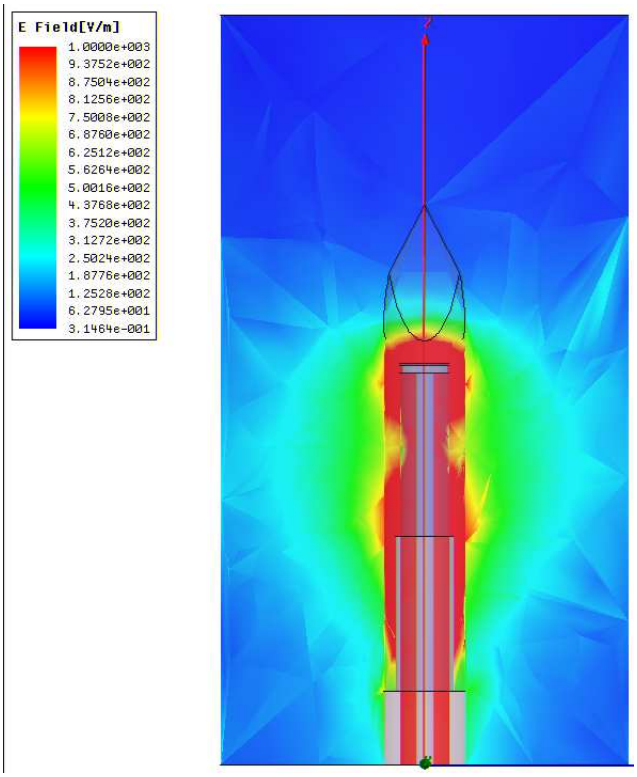

Figure 3.7: Time average magnitude of the electric field. The red zone is where the field intensity is greater than $1000\,Vm^{-1}$. The input power is 1 watt. The relative permittivity of the tissue is 43 and the loss tangent is 0.28 [11]

the center conductor and the outer conductor of the coaxial cable and in the ceramic tip. There are two areas with high intensity in the tissue in contact with the ceramic near the washer and near the junction between the copper ferrule and the ceramic.

In figure 3.8 and 3.9, the electric and magnetic field at 2.45 GHz from the radiating section of the applicator are plotted. The electric field lines are mainly in the axial direction, forming a spherically symmetric distribution centred approximately in the middle of the ceramic cylinder between the copper ferrule and the washer. The magnetic field lines have a cylindrical distribution centered around the radiating section.

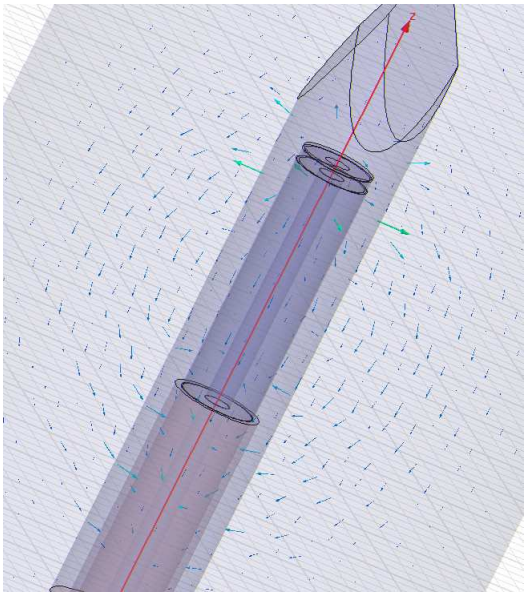

Figure 3.8: Electric field of the radiating section

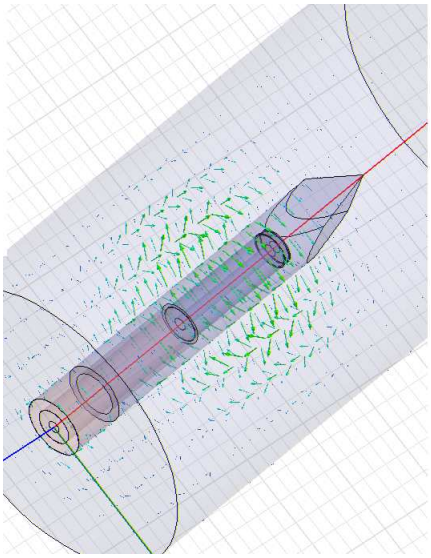

Figure 3.9: Magnetic field of the radiating section

3.4.3.3 SAR field

To know the distribution of microwave power deposition in a lossy dielectric, a convenient parameter for microwave hyperthermia is the Specific Absorption Rate (SAR). This is a measure of the amount of electromagnetic energy absorbed in a lossy dielectric material (assuming a homogenous and isotropic material). It is a scalar field and is the power absorbed by the tissue per kilogram (SAR in Wkg^{-1}). The SAR is expressed as a function of the time rms average electric field E, the conductivity σ, and density ρ of the tissue.

$$SAR = \frac{\sigma E^2}{2\rho} \tag{3.5}$$

As can be seen in figure 3.10, the SAR pattern is roughly spherical and centred on the mid part of the radiating dipole. The regions in the tissue near the washer and the copper ferrule have the higher intensity as expected from the electric field distribution.

3.4.4 Mechanical consideration

In addition to the electromagnetic properties needed for a satisfactory laparoscopic applicator, there are also essential mechanical requirements related to the mechanical robustness of the device. A cooling circuit is also required to keep the shaft and the assembly of the radiating section at a reasonable temperature.

The shaft is a stainless steel tube with a length at least 30 cm, it needs to be rigid and strong enough to support a reasonable bending stress.

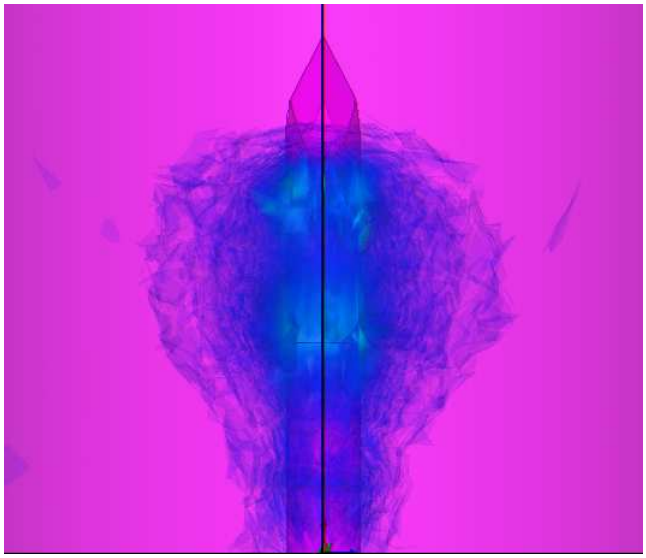

Figure 3.10: SAR distribution in the tissue. The tissue has liver properties with a relative permittivity $\epsilon_r = 43$ and a loss tangent of 0.28. The input power is 1 watt

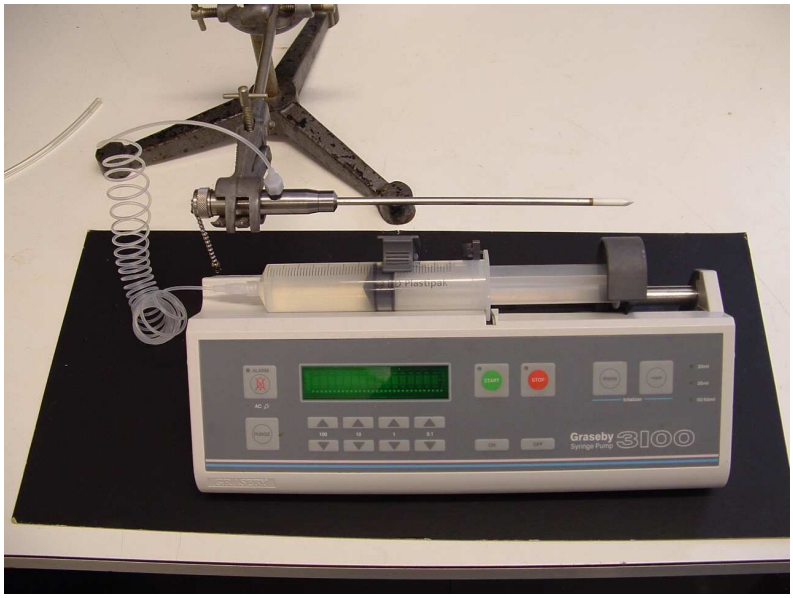

Figure 3.11: Syringe pump and 5 mm open loop water cooled applicator

The water is delivered by an electric syringe pump (Graseby® 3100) as shown in figure 3.11. A plastic tube is connected to a hole located in the handle and the water circulates between the steel tube and the coax cable and terminates in the tissue as shown in figure 3.2. A sealed joint is obtained with an rubber ring between the handle and the shaft.

The ceramic tip and the copper ferrule are assembled together with high temperature ceramic adhesive (Ceramabond®). This ceramic glue is especially suited for the junction between the copper ferrule and the ceramic tip because the glue resists to high temperatures and has a low loss tangent which prevents direct heating of the glue substrate by

the microwave field.

From a linear stress analysis as described in Appendix B, the wall thickness of the ceramic has to be thick enough to prevent excessive thermal stress inside the ceramic material. During the heating, the difference in thermal expansion between the copper and the ceramic generates a compressive stress inside the copper wall and a tensile stress inside the ceramic wall.

3.5 Applicator testing

3.5.1 S_{11} measurements with the Vector Network Analyser

To measure the magnitude of the reflection coefficient S_{11} of the applicator, a Vector Network Analyser was used. The measurement instrument shown in figure 3.12 is a Wiltron 37269A vector network analyser with a frequency range from 40 MHz to 40 GHz. By measuring voltage and current at the port of the applicator, the reflection coefficient can be obtained.

In figure 3.13, the curve with the markers is the $|S_{11}|$ parameter measured by a Vector Network Analyser (VNA) with the applicator tip in a water load ($\epsilon_r = 80$ and loss tangent $tan\,\delta = 0.15$ [11]). The black smooth curve is the $|S_{11}|$ parameter obtained from the finite element model. The minimum is -19 dB at 2.8 GHz for the measurement and -14 dB for the model at 2.75 GHz.

The bandwidth of the device (defined in the frequency range for which $|S_{11}| \leq -10dB$) is from 2.1 to 3 GHz. The curve of the predicted $|S_{11}|$ parameter from HFSS model follows the $|S_{11}|$measurement in water of the applicator despite a difference of amplitude. The two apparent differences between the measurement and the prediction from the model are:
- the model curve is a smooth line whereas the measurement curve is wiggly.
- they don't follow each other exactly.
The reason for the first difference is that there exist small standing waves between the antenna and the connector which are not modelled with HFSS.

The reason for the second is that differences of amplitude are exagerated in decibel scale. The difference of amplitude below -10 dB become less and less significative in absolute term. For example in the frequency range 2.5 GHz to 2.9 GHz of figure 3.13 the measured $|S_{11}|$ is -15 dB and the calculated $|S_{11}|$ is -20 dB. Hence by using equation 3.4, the reflected power is 3 % of the input power for the measurements and 1 % for the calculated one.

The HFSS model is sensitive to the air gaps as shown in figure 3.14 where the magnitude of S_{11} is plotted versus the frequency of the microwave signal. The built prototype can have different air gaps or some slightly different lengths. Thickness of the air gaps was evaluated from the machining tolerance of the antenna components, the copper ferrule,

Figure 3.12: Vector network analyser Anritsu Wiltron model 37269A 40 MHz to 40 GHz

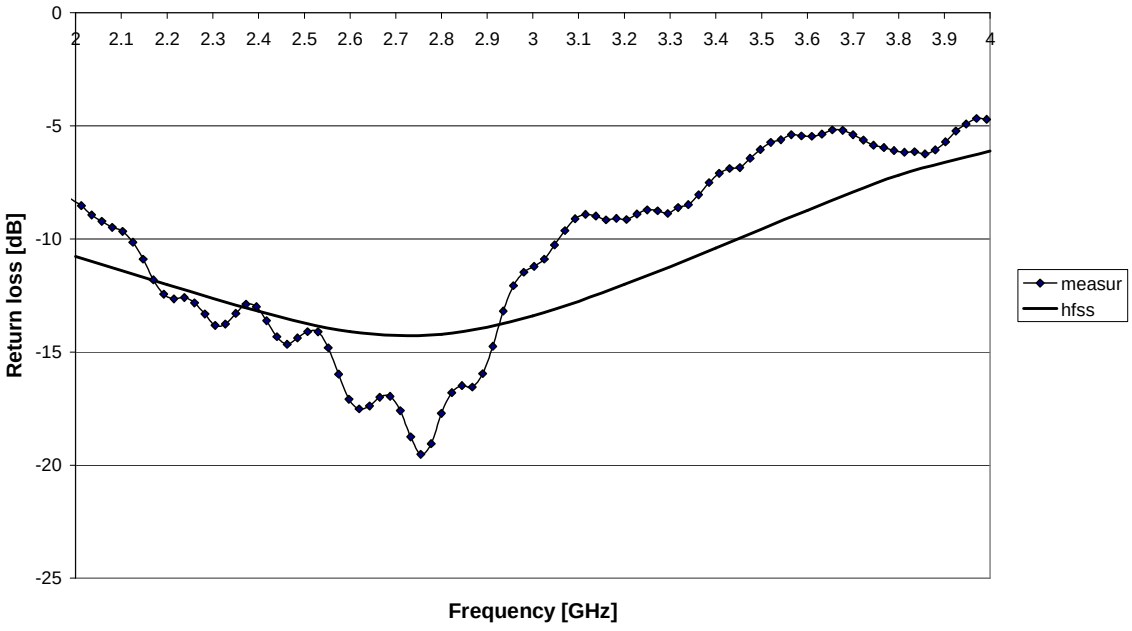

Figure 3.13: $|S_{11}|$ parameter coefficient in decibel (dB) against frequency for the 5 mm applicator from HFSS model (smooth line) compared to measured values in water (markers)

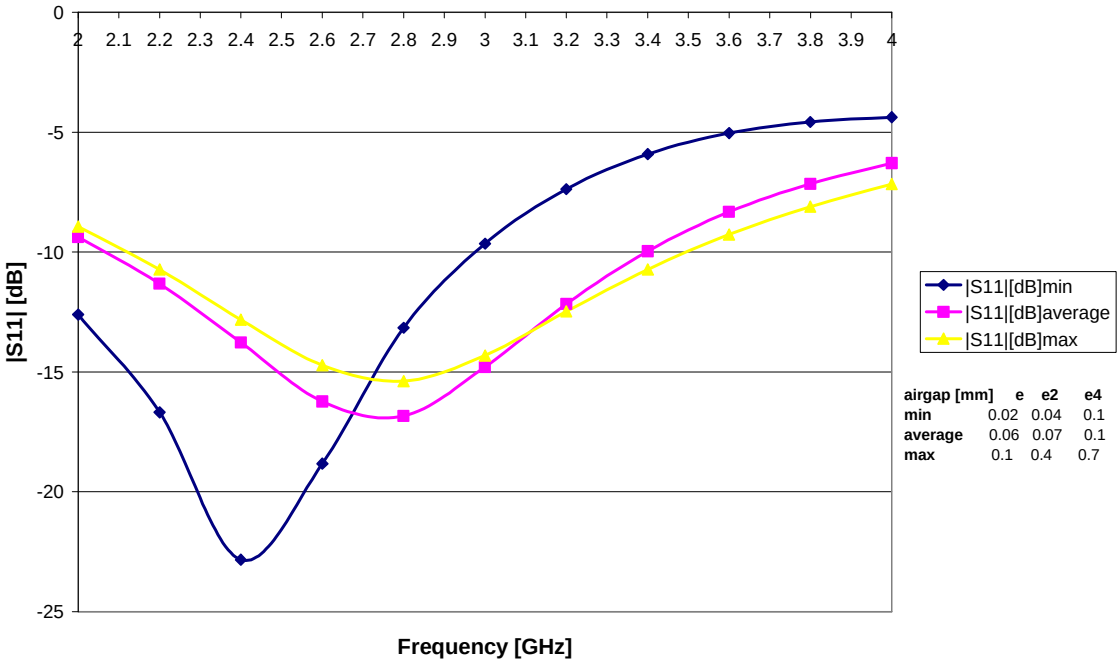

Figure 3.14: $|S_{11}|$ parameter obtained with HFSS model for three different air gap

the ceramic tip and the washer. The three air gaps are the air gap between the ceramic cylinder and the ceramic tip, the air gap between the center conductor and the cylinder and the air gap between the washer and the ceramic.

A parametric analysis had shown that the air gap along the center conductor changed the amplitude of the S_{11}. The air gap between the ceramic cylinder and the ceramic tip shifts the curve to higher frequency. The $|S_{11}|$ is minimum for the configuration with smaller air gap as shown with the blue curve in figure 3.14. As shown in figure 3.14 by comparing the blue curve with the two other curves, an increase of the size of the air gap lead to a higher $|S_{11}|$ and a shift of the minimum $|S_{11}|$ to higher frequency.

Careful control of machining tolerances is therefore essential to maintain a repeatable return loss of a given applicator design tip.

3.5.2 Microwave source

In figure 3.15 is shown the microwave source system used in these tests which consist of a high frequency sweep oscillator, that generates low power microwaves at 2.45 GHz and the travelling wave tube amplifier that amplifies the microwave signal to 60 or 80 watts for example. Microwaves are transmitted from the microwave source to the applicator through a flexible coaxial cable.

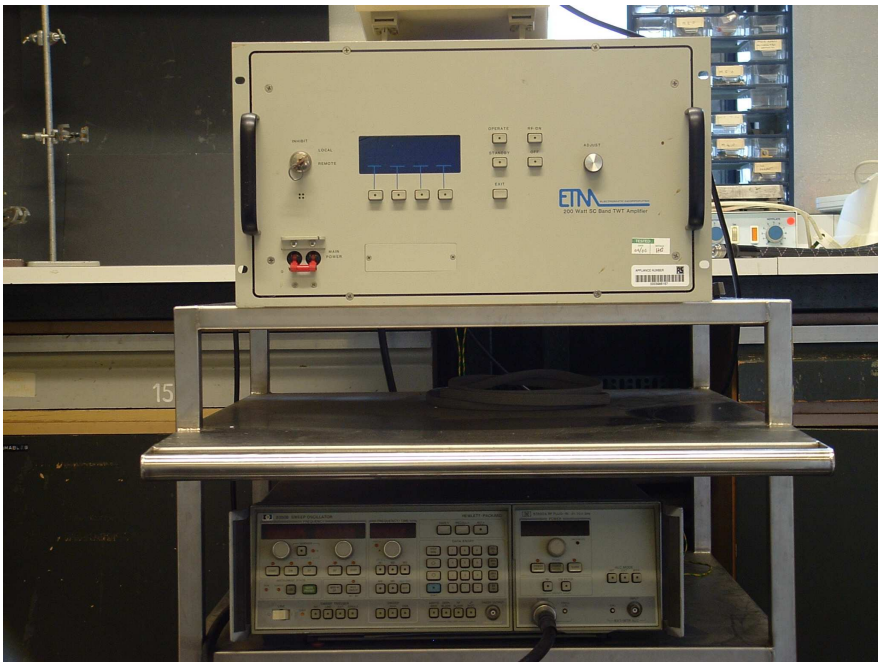

Figure 3.15: Source Hewlett-Packard HP8350B sweep oscillator combined with the amplifier, an ETM SC band travelling tube

3.5.3 Tissue phantom

A number of microwave runs have been performed in a phantom tissue to demonstrate the heating pattern of the applicator. The first set of tests used a Polyacrylamide gel (PAG) incorporating a colour changing surfactant agent to enable the visualization of the heating pattern of the applicator. This material is a transparent and high water content gel that has similar electric and thermal properties to tissue [3], [7].

A run was conducted at 50 watts for 3 minutes in PAG. This test showed a good spherical distribution of heat proving that the microwave energy distribution was localized around the ceramic radiating section as shown in figure 3.16.

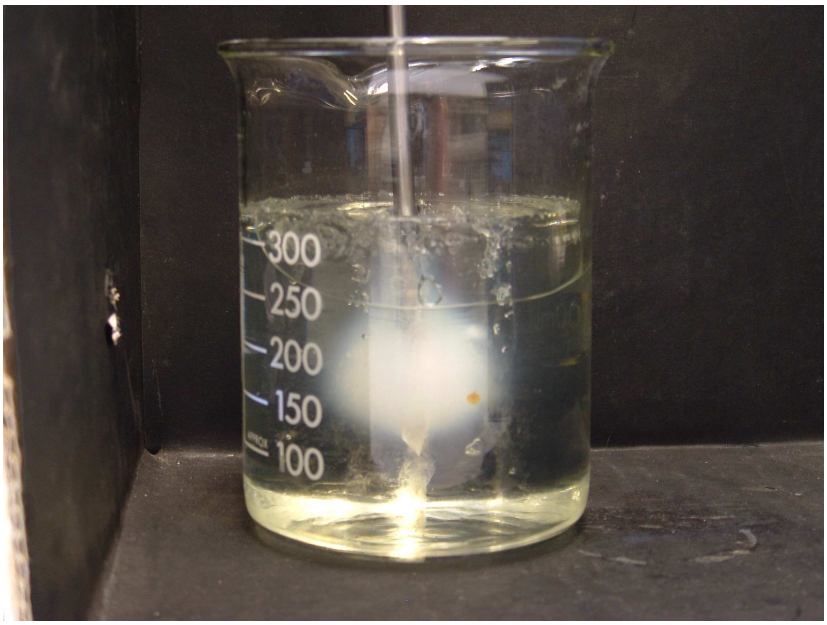

Figure 3.16: Temperature distribution in PAG after 3 minutes at 50 watts

3.5.4 Ex vivo bovine liver

Liver ablation has been performed in bovine liver to determine the effectiveness of the applicator. The liver was at an initial temperature around 10 °C (for practical reason). The duration of the ablation was 4 minutes and the different power used were 50 watts, 100 watts and 150 watts.

During the ablation, the shaft needs to remain below 42 °C to avoid burning the normal surrounding tissue. A water flow rate of $190\,ml\,h^{-1}$ was delivered, with the water exiting at the end of the applicator by small holes.

The liver was cut into two pieces along the track of the applicator insertion. Transverse sections of liver burns can be seen in figure 3.17, 3.18 and 3.19, the lesion diameter is reported in table 3.2. The ablated volume was calculated by assuming that the burn is an ellipsoid with two minor radius of length "a" and one major radius of length "b". The volume calculated from the dimensions of the ablation is $V = \frac{4}{3}\pi a^2 b$.

The shape of the burns is slightly ellipsoid and centred around the ceramic tip. As expected, there is a significant increase in size of volume ablated between the run at 50 watts and 150 watts as shown in figure 3.17 and 3.19. The ratio between the energy input and the ablated volume is nearly constant. For 150 watts a carbonized tissue region appears at the location of the ceramic tip. These ex vivo liver ablations have demonstrated that the 5 mm applicator performs large ablations of 4 to 7 cm diameter in a short time and at a high power of 150 watts.

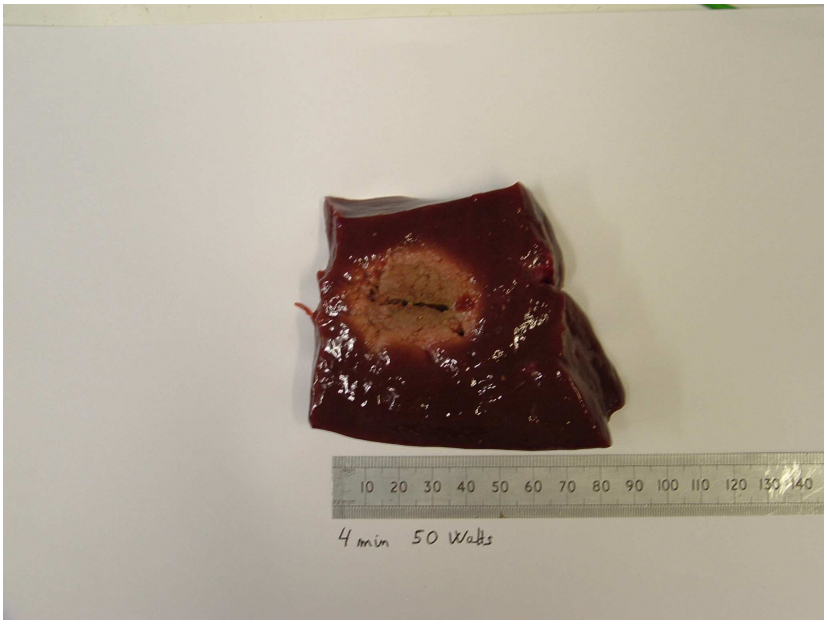

Figure 3.17: Liver ablation at 50 watts for 4 minutes

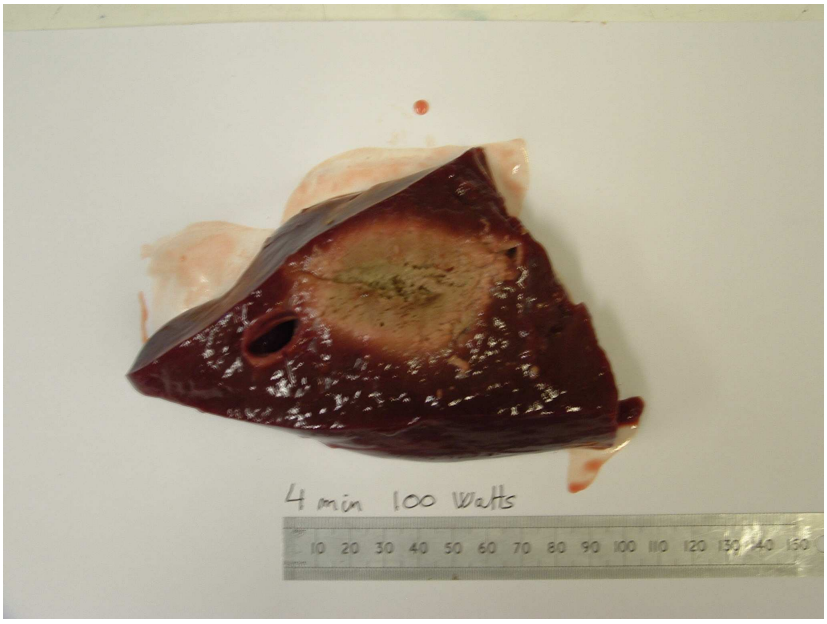

Figure 3.18: Liver ablation at 100 watts for 4 minutes

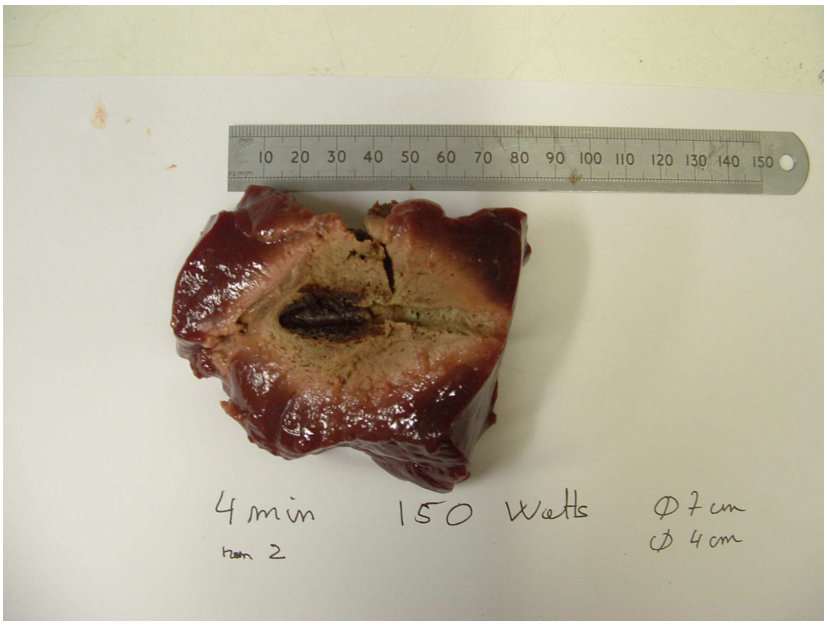

Figure 3.19: Liver ablation at 150 watts for 4 minutes

Minor and major diameter [cm] $\pm 2\,mm$	Duration of the ablation [min] $\pm 1\,\%$	Power [W] $\pm 2\,\%$	Volume of ablation $[cm^3]$	Energy [kJ] $\pm 3\,\%$
3.1-4.2	4	50	21.1±3.7	12
4-5.9	4	100	49.4 ±6.6	24
4.5-7.4	4	150	78.5±8.6	36

Table 3.2: Volume of liver tissue ablated for different input power

3.6 Summary

A 5 mm laparoscopic applicator was developed and produced spherical burns in ex vivo bovine liver. This applicator could be used with a laparoscopic procedure in order to ablate large tumours in a short time of 4 minutes at power of 100 and 150 watts.

The ability to perform large tumour ablation minimizes local recurrence by treating a large tumour in one session with a safety margin of normal tissue.

Chapter 4

2.4 mm water cooled percutaneous applicator

4.1 Introduction

The wish to ablate a spherical volume inside the organ with microwaves has led to the design of a small applicator that radiates efficiently into the tissue. The ideal applicator would be a source of microwaves located in the tumour powerful enough to ablate the overall tumour and which can be inserted in the tissue by percutaneous route. These requirements lead to the development of a 2.4 mm applicator which is close to this ideal applicator.

The development of this antenna design was originally carried out by Prof N. Cronin, Dr P. Clegg and M.Boix from the Medical Technology Group of Bath University. The design and the electromagnetic model are presented here because this applicator and the 2.4 mm gas cooled applicator described later use the same radiating section. Furthermore, it has been studied intensively over the last three years and is undergoing clinical trials with an interventional radiologist.

4.2 Application and medical procedure

Open surgery for liver cancer consists of the removal of the tumour by cutting and separating the tumour from the surrounding tissue. To minimize the risk of local recurrence, a margin of 1 cm between the tumour and the normal tissue is usually taken. This method has the best outcomes concerning the survival rates and the rate of local recurrence [53]. However for some patients, open surgery does not apply. These patients are considered

inoperable for one or a combination of the following reasons:
- the patient is too weak or old and the risk associated with open surgery is too high.
- the liver of the patient is in too poor condition.
- the patient has bipolar liver tumours (tumours in both sides of the organ).
For these cases, percutaneous surgery avoids the need for laparoscopy by introducing the device through the skin and locating the radiating tip inside the tumour. It is a much less invasive technique than either an open surgery or a laparascopic procedure.

The first step performed by the radiologist is the accurate localization of the tumour inside the organ. This is done by performing a computed tomography scan (CT scan) of the abdomen of the patient before starting the insertion of the applicator. The position of the tumour relative to a series of markers positioned on the skin of the patient is determined. The surgeon also uses an ultrasound probe applied on the surface of the abdomen to help the localization of the tumour and the placement of the applicator.

Once, the position of the tumour in the organ relative to the markers has been determined, the insertion of the device can be performed. The insertion is facilitated by a sharp tip and rigid shaft of small diameter.

The second step before the start of the treatment, is verification of the correct location of the radiating section in the tumour by taking further CT scan images. Because the ceramic material has high reflectivity, the radiating section is clearly identified on a CT scanner picture. If the ceramic tip is not in the tumour, the applicator needs to be repositioned.

The last step is the actual treatment which involves setting the power source to the required level for a time duration of a few minutes depending on the volume of tissue that needs to be ablated.

From this procedure description, a set of properties required for the applicator can be extracted.

4.3 Specifications

To facilitate the insertion of the applicator through the skin and the organ, the applicator needs to have a sharp cutting trocar tip. This trocar tip as shown in figure 4.1 is made of three cutting planes that cut the tissue during the insertion.

The device needs also to be relatively light and robust to facilitate its manipulation and its positioning into the organ.

Tumours have variable sizes from a few millimetres to a few centimetres. For this reason, it is desirable to achieve a 5 cm diameter ablation with a percutaneous device to have a safety margin of 1 cm between the normal tissue and the tumour [70].

The diameter of the device also needs to be small to minimize the incision performed

Figure 4.1: Trocar tip geometry. Sharp tip with three cutting edges in order to penetrate easily the tissue

during the percutaneous procedure.

Finally, the treatment requires the ablation of the tumour only and a protection of the normal surrounding tissue. For this reason, the shaft needs to be cooled by a fluid in order to maintain a shaft temperature below a safety limit set by the regulatory authority below 42 °C.

4.4 Applicator design

4.4.1 Principle of operation

The principle of operation of the radiating section is the same as that described in section 3.4.1 of the 5 mm applicator. The critical lengths l_1, l_2, h_1 and h_2 are adjusted to give a good microwave match at this diameter. The particular design adopted is shown in the figure 4.2.

4.4.2 Geometry

The 2.4 mm applicator consists of similar components previously described for the 5 mm applicator. The radiating section is composed of the coaxial cable with the center conductor forming a branch of the antenna. The washer is soldered at the end of the

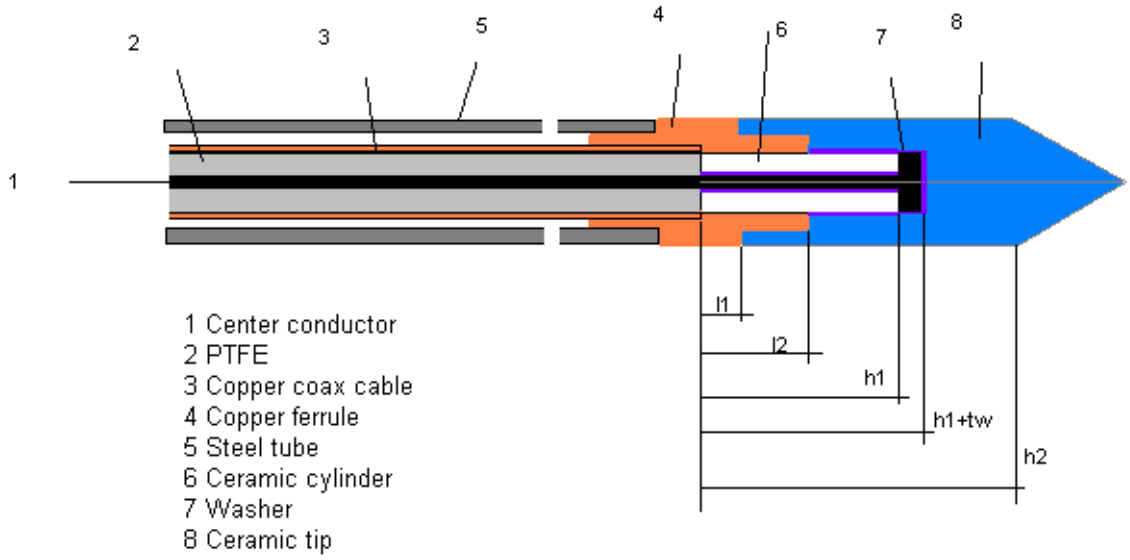

Figure 4.2: Dimmensions of the radiating section of the 2.4 mm applicator

Dimensions	[mm]
Radius center conductor	0.25
Radius dielectric	0.75
Radius coax cable	0.89
Radius shaft	1.2
Radius washer	0.7
l1	4.5
l2	8.5
h1	14.2
h2	17.7
tw	0.5
e air gap center	0.06
e2 air gap cylinder	0.01
e4 air gap washer	0.04

Table 4.1: Dimensions of the 2.4 mm applicator tip

center conductor. Between the copper ferrule connected to the coaxial cable and the washer, the ceramic cylinder is inserted with the center conductor in his core. The end of the applicator, from the copper ferrule to the washer, is covered with a ceramic yttrium zirconia tip as shown in figure 4.3. Dimensions of the radiating section of the current 2.4 mm open loop applicator obtained with HFSS package are given in table 4.1.

The handle is a tube made of polymer Acetal material with a chamber enabling the fluid to be injected in the annular space between the shaft and the coaxial cable. It also has an ergonomic design for manipulation by the surgeon. In figure 4.4, the different parts of the percutaneous applicator are shown.

The coaxial cable shown in figure 4.4 is a low loss cable made of a hollow copper tube filled with PTFE dielectric (Rhophase® low loss cable 070LL-183-strip) and a copper wire in the middle. It has a cut off frequency much higher then the 2.45 GHz operating frequency used for our application. The coaxial cable of the 2.4 mm applicator has an inner and outer radius respectively of 0.25 mm and 0.75 mm with a dielectric constant $\epsilon_r = 1.7$.

Different modes of propagation exist for wave guides. The dominant mode is the mode that propagates at the lowest frequency. For the coaxial line wave guide type, the dominant mode is the TEM mode (Transverse electromagnetic wave). For a coaxial line, the TEM mode always exists and propagates from zero to high frequency. To avoid higher propagating modes with different propagating constant it is useful to know when the first higher mode starts to propagate.

The first higher mode is TE_{11} whose cutoff frequency is 36 GHz. Therefore only the TEM mode will exist in the coaxial line for a frequency range from 0 GHz to 36 GHz.

Cut off frequencies of progating modes can be obtained by solving the Laplace equation to obtain a potential function solution ϕ. Then the field solution can be derived from the potential function.

The shaft obtained is stainless steel grade 316 shaft of 2.4 mm diameter that provides stiffness and robustness. The shear forces appearing at the interface shaft/ tissue during the insertion of the applicator are minimized by using a coating polymer covering the shaft. The application of a coating polymer on the shaft of the device gives a low friction coefficient at the shaft-tissue interface and facilitates the insertion and the removal of the applicator in the tissue.

4.4.3 Finite element electromagnetic model with HFSS

The HFSS software package was used to determine the dimensions of the components to achieve a good microwave radiation pattern in the tissue and low reflected power. The electric material properties used for the model are given in the table 4.2. All the components are non magnetic and have therefore a relative magnetic permeability $\mu_r = 1$.

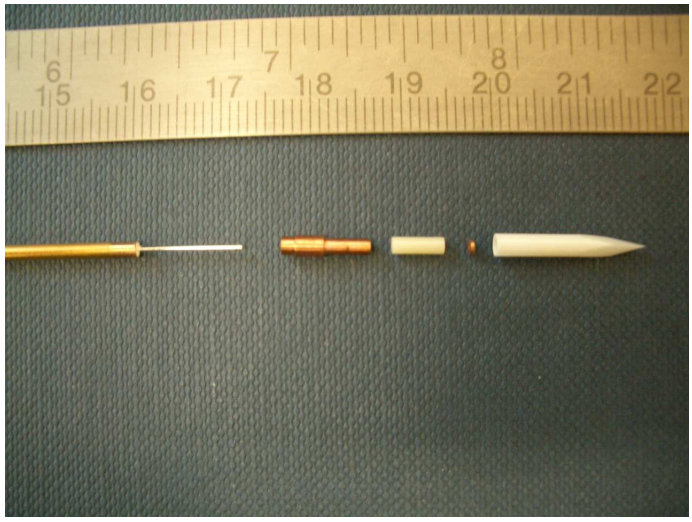

Figure 4.3: Components of the radiating section of the 2.4 mm applicator

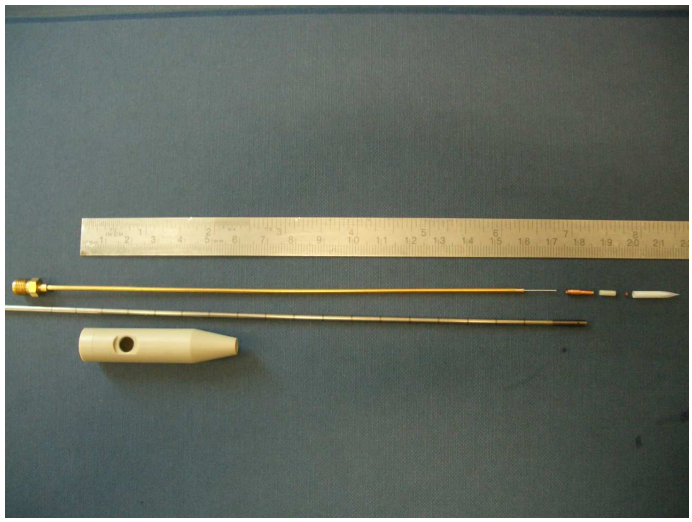

Figure 4.4: Components of the 2.4 mm open loop applicator

All materials are assumed to be lossless (tan δ=0), except for the PTFE dielectric. The values in table 4.2 were used for the field distribution and $|S_{11}|$ parameter calculations.

Material	Component	ϵ_r	μ_r	$tan\,\delta = \frac{\epsilon''}{\epsilon'}$
Copper	washer, coaxial cable	1	1	0
Ceramic	cylinder, trocar tip	20	1	0
PTFE	dielectric	1.7	1	0.001

Table 4.2: Electromagnetic material properties used in the 2.4 mm applicator HFSS model

4.4.3.1 S_{11} parameter

The return loss or $|S_{11}|$ parameter is the main parameter to characterize a good transmission microwave energy from the radiating section of an applicator to the load. The significance of S_{11} parameter is explained in section 3.4.3 of chapter 3.

In water, at 2.45 GHz the $|S_{11}|$ is -9 dB and is below -10 dB in bovine liver. It has been observed that the curve of the $|S_{11}|$ parameter is shifted from 0.1 GHz to 0.5 GHz to the left. During applicator activation, the complex permittivity of the liver changes due to the dessication of the tissue. For this type of applicator using a dipole antenna, this shift of the minimum of the $|S_{11}|$ to lower frequencies during the dessication of the tissue lead us to design the microwave applicator with a $|S_{11}|$ below -10 dB until 3 GHz.

In figure 4.5, the magnitude of modelled and measured $|S_{11}|$ parameter are plotted. The value of complex permittivity of deionized water used for the model is $\epsilon_r = 78.6 - 11.6j$ [11]. In general there is a good agreement between measured and calculated S_{11}. Oscillations seen in the measurements are due to a reflected wave between the source and the load.

From the measurements, oscillations occur and the difference of frequency between two maxima is $\Delta\nu = 0.14\,GHz$. Let ν_n be the frequency at which there are n half - wavelengths in the line of length L.

$$n\frac{\lambda_n}{2} = L \tag{4.1}$$

$$\nu_n = \frac{nc}{2L} \tag{4.2}$$

with λ_n the wavelength of the wave and c the celerity of the wave. From equation 4.2, the difference of frequency is:

$$\Delta\nu = \nu_{n+1} - \nu_n = \frac{c}{2L} \tag{4.3}$$

The distance between the port and the reflection point can be expressed in function of the difference of frequency between two maximas.

$$L = \frac{c}{2\Delta\nu} = \frac{3E8}{\sqrt{1.7} \times 2 \times 0.14E9} = 0.82\,m \tag{4.4}$$

where $c = \frac{c_0}{\sqrt{\epsilon_r}}$ is the velocity of the wave in the dielectric of the coaxial line, and $\Delta\nu$ is the difference of frequency between two extremas for one oscillation of figure 4.5. The measured distance between the port of the vector network analyser and the radiating section of the applicator is 83 centimetres. The difference between the measured and calculated distance can be explain by the inaccuracy of the material permittivity value. So, the oscillation of the magnitude of the S_{11} on the measurement are due to a reflected wave occurring between the radiating section of the applicator and the port of the VNA.

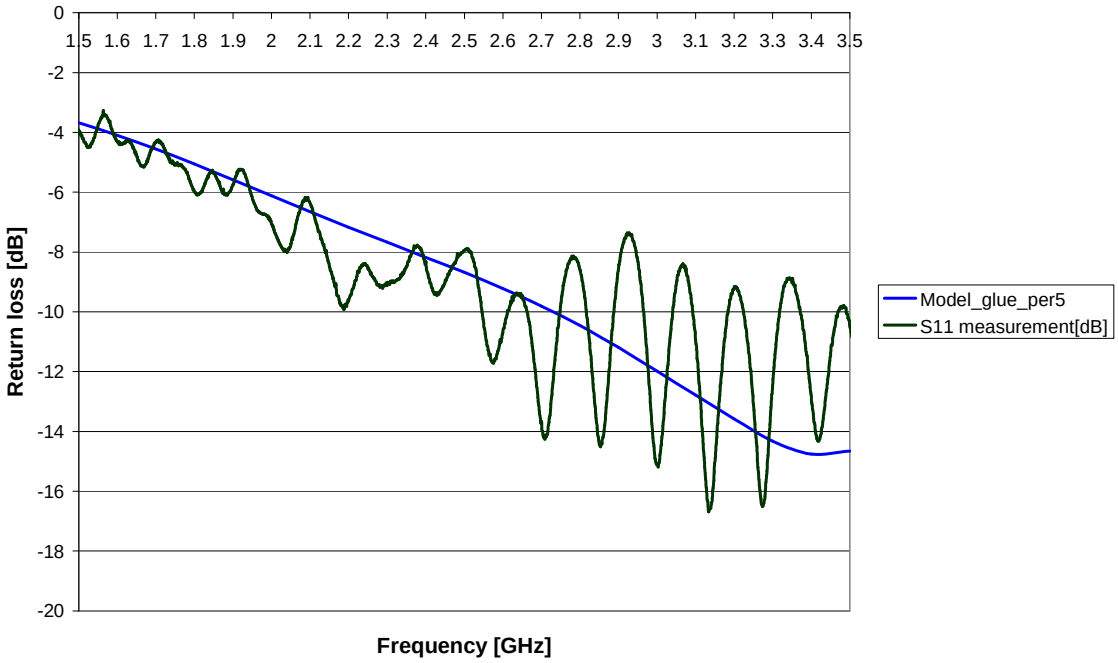

Figure 4.5: Loss return [dB] modelled and measured in water

4.4.3.2 Electric field

The time average amplitude of the electric field is plotted in figure 4.6. The model shows an ellipsoid electric field distribution with high intensity in the neighbouring of the washer and copper ferrule branches. The electric field is lower in the ceramic trocar tip with a decrease of the electric field amplitude after the washer element.

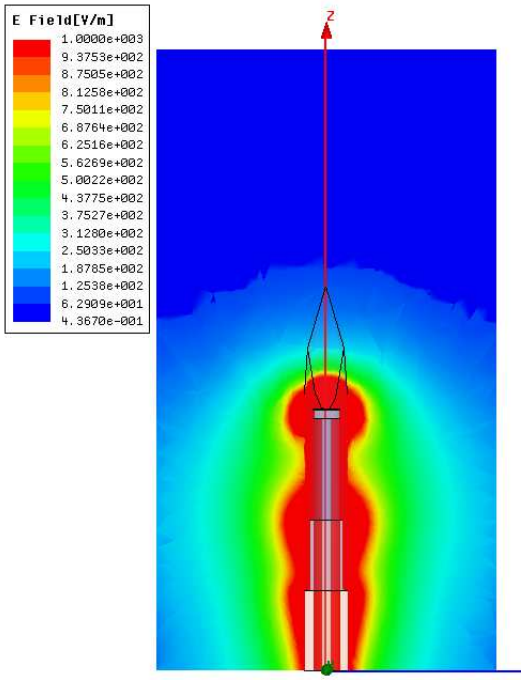

Figure 4.6: Magnitude of the electric field. The red zone is where the field intensity is superior to 1000 V/m. The input power is 1 watt, the relative permittivity of the tissue is 43 and the loss tangent 0.28 [22]

4.4.3.3 Energy or SAR field

In figure 4.7 high energy density occurs near the washer and copper ferrule branches with an ellipsoidal energy distribution. The figure 4.8 show the symmetrical SAR density around the z axis. For this model the electric and thermal properties are constant against temperature and the input microwave power is 1 watt. Because the SAR is proportional to the input power, the SAR scale needs to be multiplied by the real power, 60 watts for example, to know the corresponding energy distribution in the tissue.

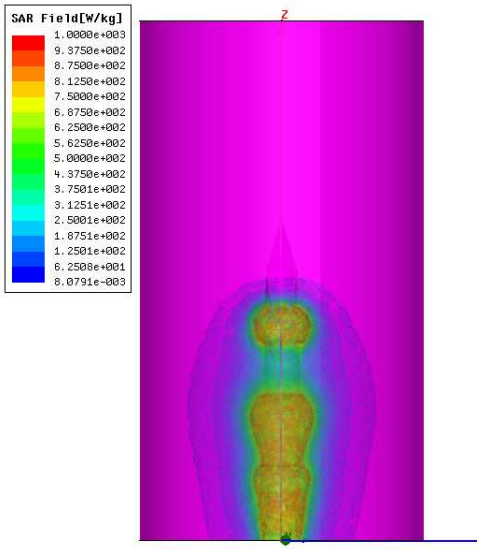

Figure 4.7: Specific Absorption rate (SAR)

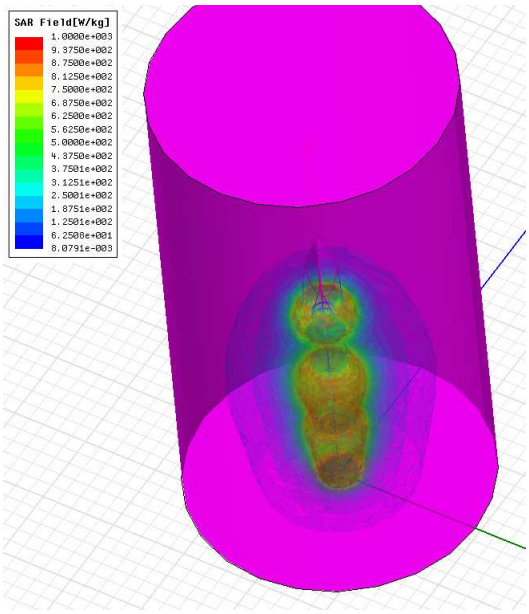

Figure 4.8: SAR distribution around the radiating tip

4.4.4 Mechanical consideration

Figure 4.9: Labcoter Parylene Deposition System

To prevent sticking and adhesion of tissue on to the applicator, a thin layer of the polymer Parylene N (poly-para-xylylene) is deposited on its surface of the applicator. The deposition and formation of Parylene on a substrate occurs in a vacuum chamber. (Parylene deposition system PDS 2010 Labcoter 2, see figure 4.9) and can be viewed as a condensation process occuring at room temperature and low pressure.

The Parylene deposition system consists of two main parts. The pyrolysis furnace where the solid Parylene powder sublimes into a gas monomer. This heats and cleaves the

gaseous Parylene dimer into a monomer form.

The vacuum chamber is where the polymerization of the gaseous monomer occurs at room temperature as the Parylene deposits as a polymer onto the applicator shaft.

The pressure inside the vacuum chamber is the most important factor that will affect the quality of the substrate coating quality. The quality of the coating increases when the pressure is low. Excessive coating pressure will lead to formation of coating nodules, impurity and a bad coating quality [13].

To guarantee the best adhesion of the polymer on the surface, the surfaces need to be very clean and an adhesion promoter is used. The promotion solution is applied on the shaft of the applicator before the parylene procedure. The promotion solution is made of Isopropyl alcohol and deionised water in the same proportion. 0.5 % of Silane A -174 is added to the solution.

4.5 Applicator testing

To characterise the working of the applicator various tests were performed:
- measurement of the magnitude of S_{11} to calculate the reflected power.
- a calorimetry test in which a known quantity of water is heated.
- a field test in tissue phamtom to control the pattern of the energy radiation of the radiating section.
- microwave ablations in ex vivo bovine liver to test effectively the applicator.

4.5.1 $|S_{11}|$ measurement in ex vivo bovine liver

The $|S_{11}|$ measurement in ex vivo bovine liver is shown in figure 4.10. At 2.45 GHz the match is -11.3 dB and continuously decreases at higher frequency. The applicator has a good match, which improves during the dessication of the tissue. At 2.6 GHz, the match is -12 dB, which means that only 6.3 % of the input power is reflected.

The wavelength in an isotropic and homogenous medium is given by:

$$\lambda = \frac{c_0}{\sqrt{\epsilon_r}} \frac{1}{f} \tag{4.5}$$

with c_0 the speed of light in the vacuum, ϵ_r the relative electrical permittivity of the medium and f, the frequency of the electromagnetic field.

Let be ϵ_{r1} the relative permittivity of normal bovine liver and ϵ_{r2} the relative permittivity of dessicated bovine liver at 2.45 GHz. λ_1 and λ_2 are the wavelengths of the electromagnetic waves in normal and dessicated liver respectively. Because, the dessicated tissue has a lower water content than normal tissue, the relative electrical permittivity is lower in dessicated tissue than in normal tissue [65]. Equation 4.5 implies that $\lambda_2 > \lambda_1$. The wavelength in dessicated tissue will be longer than the wavelength in normal tissue.

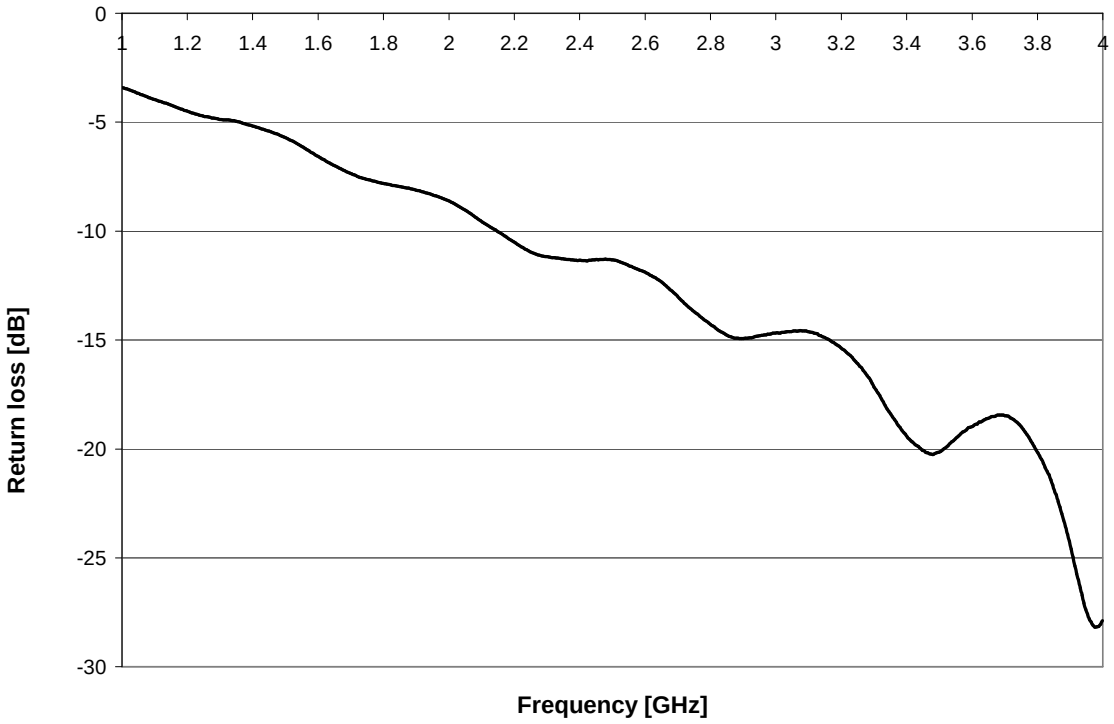

Figure 4.10: Magnitude of the S_{11} parameter of the 2.4 mm applicator in ox liver tissue

This means that in dessicated tissue, the antenna should run at a frequency lower than 2.45 GHz. In other words, the $|S_{11}|$ curve has shifted from right to left of figure 4.10. For this reason, to ensure an improving match in tissue during the dessication process, it is good to have a continuously decreasing $|S_{11}|$ toward higher frequencies ($\frac{\partial|S_{11}|}{\partial f} < 0$).

4.5.2 Calorimetry

To verify that most of the microwave energy is deposited in the tissue load and to characterise the efficiency of an applicator, a calorimetry test has been performed.

It consists of heating a known quantity of water contained in a thermal insulated bucket. With the thermal specific heat of water and the difference of temperature between the final and initial time it is possible to calculate the energy deposited in the water load and compare with the microwave energy input.

This test allows calculation of the overall efficiency of the applicator, for a given input power, the rise of water temperature gives the energy deposited into the water load. The ratio between the energy deposited into the load and the input energy gives the overall efficiency of the applicator. (The loss of the coaxial cable is taken into account).

The ceramic tip of the applicator was immersed into the water enclosed in an insulated recipient. The mass of water was 0.2 kg and the intial temperature of water was 20.6 °C. The specific heat of water at 20 °C is $4182\,Jkg^{-1}K^{-1}$. The input power was 20 Watts

for one minute. After the run, the temperature was recorded and was 21.8 °C. Hence the energy deposited into the water is:

$$Q = 0.2 \times 4182 \times (21.8 - 20.6) = 1004\ J \tag{4.6}$$

The microwave energy input at the applicator is:

$$E = 20 \times 60 = 1200\ J \tag{4.7}$$

hence , it can be concluded that most of the microwave energy radiates into the water and the efficiency of the applicator with these figures is:

$$\epsilon = \frac{1004}{1200} = 0.84 \tag{4.8}$$

It is interesting to check the conservation of energy through the applicator. From the figure 4.5, the S_{11} at 2.45 GHz in water is -8.5 dB. By using the definition 3.4, the reflected power is 2.8 Watts for a 20 Watts input power. From E.21 of Appendix E, the loss in a 20 cm length of coaxial cable are 0.8 Watts. Hence, the power which radiates from the antenna is:

$$P_{rad} = 20 - 2.8 - 0.8 = 16.4\ W \tag{4.9}$$

The energy radiated from the applicator for one minute is:

$$E_{rad} = 16.4 \times 60 = 984\,J \tag{4.10}$$

This result is in good agreement to the 1004 J calculated with the calorimetry measurements and proves that the measurements of $|S_{11}|$ and energy cable loss are correct.

4.5.3 Tissue phantom PAG

Once the working of the applicator was checked with the $|S_{11}|$ measurement and the calorimetry test, a transparent polyacrylamide gel phantom tissue sensitive to heat was used to evaluate the field pattern of the applicator [3]. The phantom tissue PAG has similar electrical and thermal properties to biological tissues such as bovine or human

Polyacrylamide gel	
Density$[kgm^{-3}]$	1030
Specific heat capacity $[Jkg^{-1}K^{-1}]$	4187
Thermal conductivity $[Wm^{-1}K^{-1}]$	0.41
Complex permittivity at 7 GHz $[Fm^{-1}]$	$(48.2 - j21.8)\epsilon_0$

Table 4.3: Thermal properties of polyacrylamide gel [7]

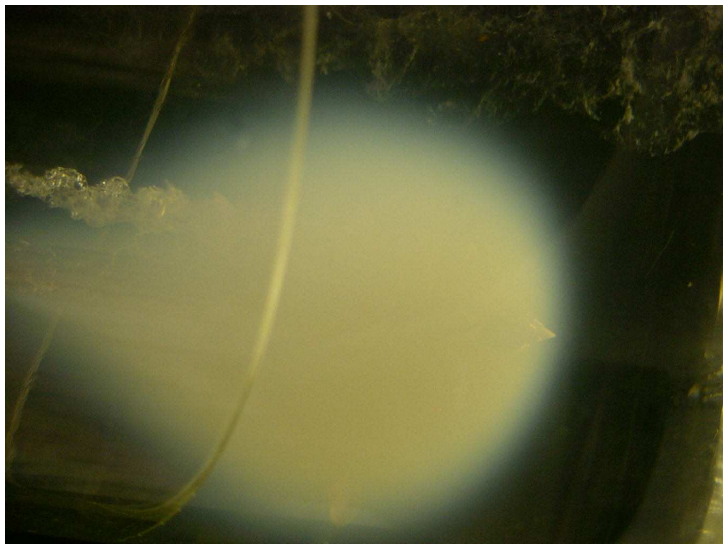

Figure 4.11: Spherical energy distribution in Polyacrylamide phantom tissue

liver. The value of density, specific heat, thermal conductivity and complex permittivity are given in the table 4.3.

At the beginning of the run the energy distribution is ellipsoid as shown by the HFSS model. At the end of the run and for a larger radius, the energy is transferred radially from the radiating source to the outside by conduction and the energy pattern in PAG is more and more spherical as shown in figure 4.11.

4.5.4 Ex vivo bovine liver

Ex vivo bovine liver ablation at various powers and time were performed to check the performance of the applicator in conditions close to the operation theatre. $180\,mlh^{-1}$ of water was flowing in the annular space between the coaxial cable and the inner shaft. In figure 4.12 is a cross section of an ablation in an ex vivo bovine liver after a run of 60 watts during 4 minutes. The brown tissue is the ablation area and the dimensions of the two axis of the ellipsoid are 4 cm and 5 cm for a run at 60 watts for 4 minutes.

In figure 4.13, the ceramic location can be seen clearly and carbonized tissue is observed due to high temperature during the run at 80 watts for 8 minutes. Because the volume is proportional to the cubic radius, a small increase of the diameter of the cross section of the burn leads to a significant increase of ablated volume.

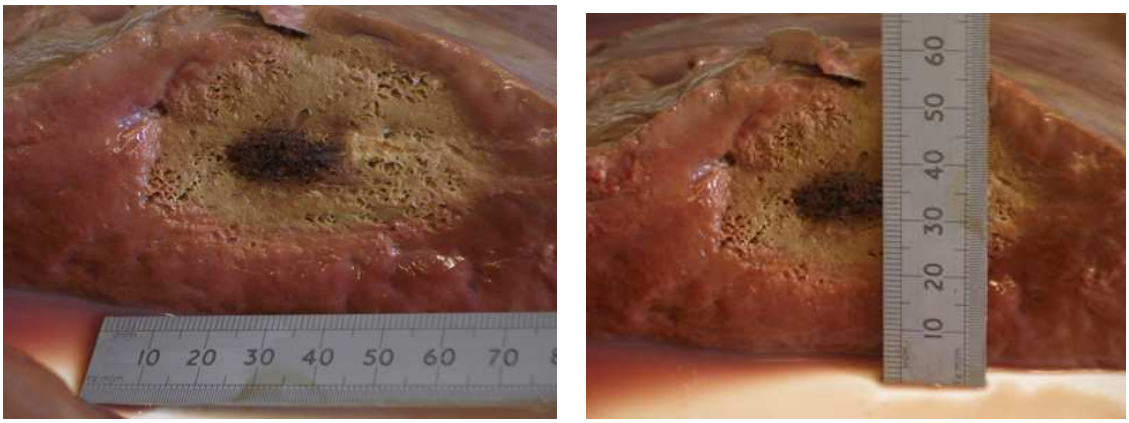

Figure 4.12: Bovine liver ablation 4 minutes, 60 watts

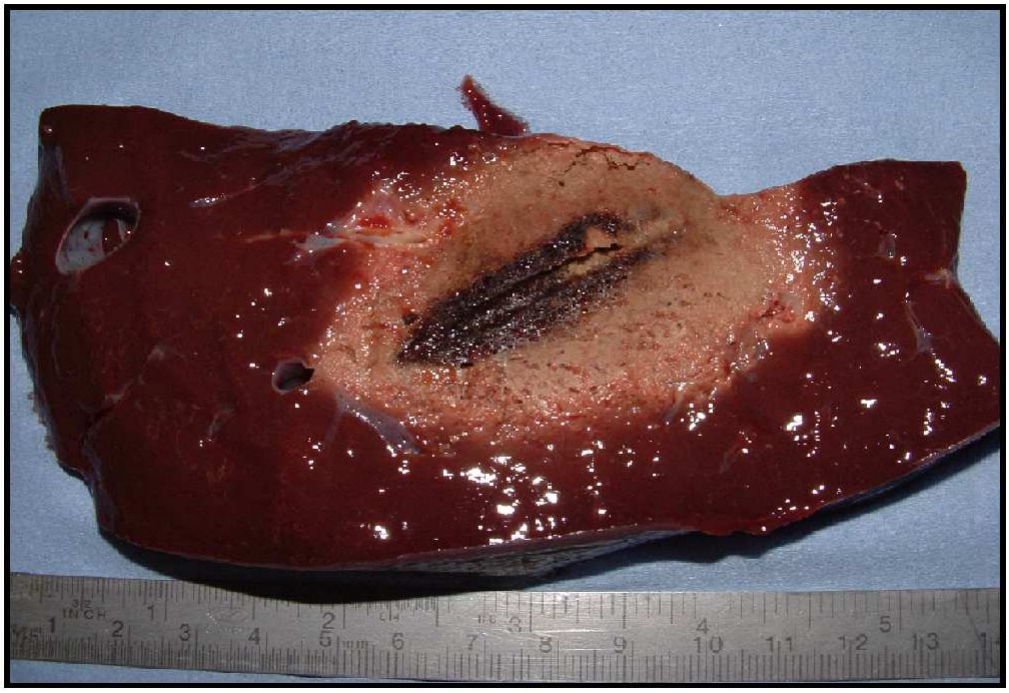

Figure 4.13: Bovine liver ablation 8 minutes, 80 watts

4.5.5 Conclusion

$|S_{11}|$ measurements in water and in ex vivo bovine liver have shown a good microwave energy transmission into the tissue with a match below $-11\,dB$ at 2.45 GHz. The match improves at higher frequency which gives a good energy deposition during the tissue dessication.

Calorimetry test has proved that the energy effectively deposited into the water is between 80 % and 90 % of the input power and higher in the liver tissue.

Tissue phamtom tests in PAG material have shown an energy density pattern similar to the finite element model.

Finally, ex vivo bovine liver ablation have been performed at 60 and 80 watts for 4 minutes showing the good working of the applicator.

In the next section, fluid movements occuring during a thermal ablation are discussed together with potential risks.

4.6 Fluid movement during thermal ablation

During a microwave thermal ablation, temperatures in the range of 150 °C to 250 °C [80] occurred in the tissue surrounding the radiating section of the applicator. Temperature of fluids present in the ablation volume increases and a fraction is heated above 100 °C and is transformed into vapour. The exact process of tissue change and fluid movements during an ablation is not well known and the complex structure of the liver renders quantitative analysis of fluid movement and structural changes of the tissue very challenging.

For the following discussion the temperature of phase change will be assumed to be 100 °C which is the temperature of vaporization for water at one atmosphere. In reality this temperature is probably higher because pressure inside the ablation volume is higher than the atmospheric pressure. The second reason is that the fluid is a composition of water and blood. Its temperature of vaporization can differ slightly from 100 °C.

Thorvaldsson and Janestad [73] developed a one dimensional model for simultaneous heat, water and vapour diffusion inside food during heat processing. Dincov *et al* [21] have developed a multiphase transport porous model by coupling the electromagnetic field and the heat transfer through a change in dielectric properties to predict the drying behaviour of porous media. Dielectric properties and thermal properties of a tissue are strongly dependant on the moisture content [65], [22].

4.6.1 Structure of the liver tissue

Liver tissue consists of a solid phase and fluid phase with blood, ions content and water. The liver is a complex hierarchical structure with arteries, veins and capillaries.

Mass transport of fluid, nutriments and minerals are achieved by diffusion within the tissue. For this reason, energy transport in tissues can be modelled using the fluid and heat transfer model in a porous media, a review of porous media used in modelling flow and heat transfer is given by Khaled and Vafai [42]. For flow in soft connective tissue, perfused muscle and tumours, Darcy model which gives a linear relationship between the flow and the pressure gradient through a material of a given porosity can be used to model flow transport in a porous media.

Vankan *et al* [76] have developed a finite element model for hierarchical porous media in order to model fluid flow and deformation of the tissue. The blood perfused biological tissue is described as a mixture in which the fluid phase is the blood and the surrounding

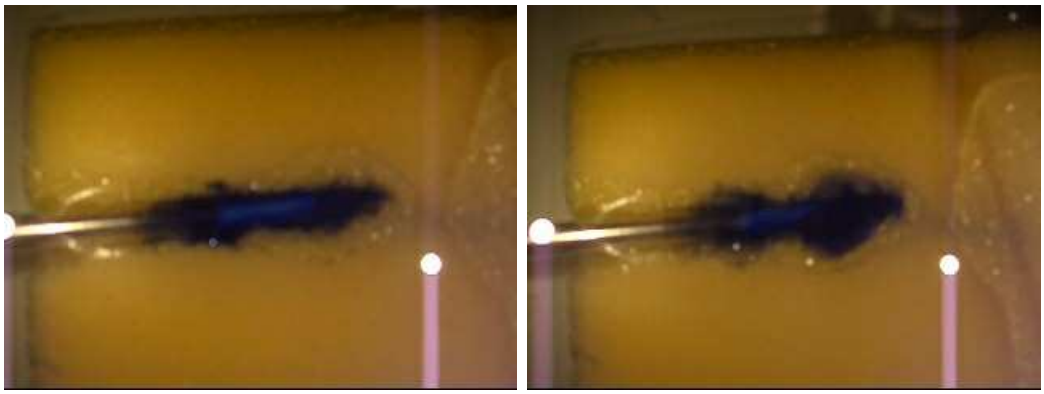

Figure 4.14: Applicator inserted in a sponge with ink in the vicinity of the tip, beginning of the run

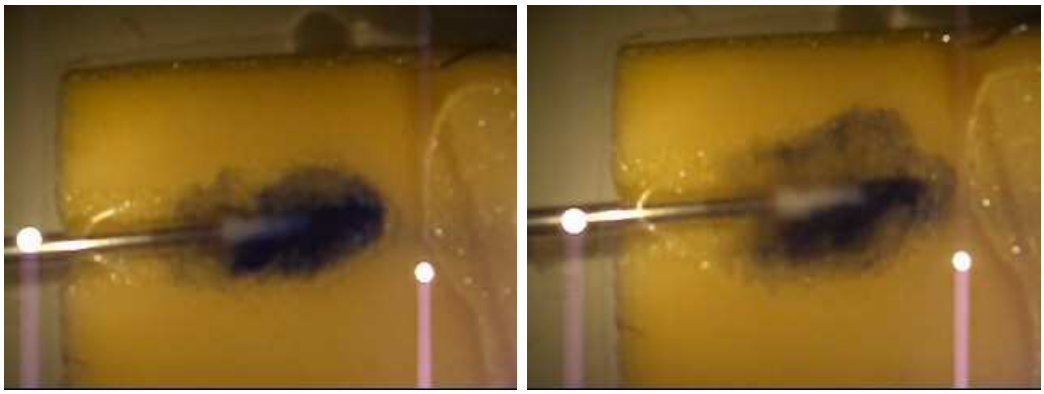

Figure 4.15: Applicator inserted in a sponge, end of the run

tissue is the solid phase. Vascular properties such as vessel diameter, wall thickness and stiffness vary over the hierarchy.

4.6.2 Effect of water dilatation

Below 100 °C, fluid movement occurs when the water temperature increases, the volume of water increases by dilatation and leads to water movement. To visualize the effect of microwave heating of water near the ceramic tip, an experiment with a porous sponge was performed. The applicator was inserted in a sponge full of water and ink was deposited with a syringe around the radiating section. Figures 4.14 and 4.15 show the ink fluid moving through the sponge during microwave heating. Fluid movement occurred radially under a pressure gradient due to the thermal dilatation of the fluid in the vicinity of the radiating section of the applicator.

4.6.3 Steam generation in bovine liver tissue

Since the temperature in the tissue near the ceramic tip is above 100 °C, some water is transformed into vapour. Conservation of mass requires that the water initially in the

Time[s]	x distance [mm]	y distance [mm]
0	32	32
90	176	96
180	110.4	230

Table 4.4: Distance evolution of the radioisotope fluid in the x and y direction during a microwave ablation in bovine liver

tissue before the thermal ablation moves outward into the surrounding tissue during the ablation. Above 100 °C, the water changes into vapour generating a pressure gradient which causes fluid movement. These fluid movements flow preferentially along the lowest resistance flow path such as veins, arteries or capillaries and occur in the proximity of the applicator tip in the tissue. As a result, significant changes in water content in the ablation volume occurr [82]. An experiment was conducted by D. Hardie [30] to try to measure the distance travelled by the water during an ablation located near a large blood vessel.

4.6.3.1 Experimental set up

In ex vivo bovine liver a tagged isotope solution (Technetium) was injected in the surrounding of the radiating tip prior to ablation. Then, an ablation was performed at 100 watts for 3 minutes.

The tracking of the radioisotope fluid was possible during the ablation by recording the radioactive radiation from the ablation zone with a gamma camera.

Three picture were taken at different times. The first one was taken just before the microwave source was switched on. The second was taken in the middle of the run and the last one was taken at the end of the run (3 minutes after the microwave source was switched on). These three pictures are presented in figure 4.16.

4.6.3.2 Results

For each picture, the maximal diameter in the x and y directions was measured and is shown in table 4.4.

From the figure 4.16, the water diffuses outward through the liver tissue. In the y direction, after 3 min, particles of the radioisotope fluid can be found 23 cm from the insertion of the tip.

4.6.3.3 Conclusion

The experiment proves that radial fluid movements occur during an ablation. Its moves radially through the porous tissue and moves also preferentially through the least

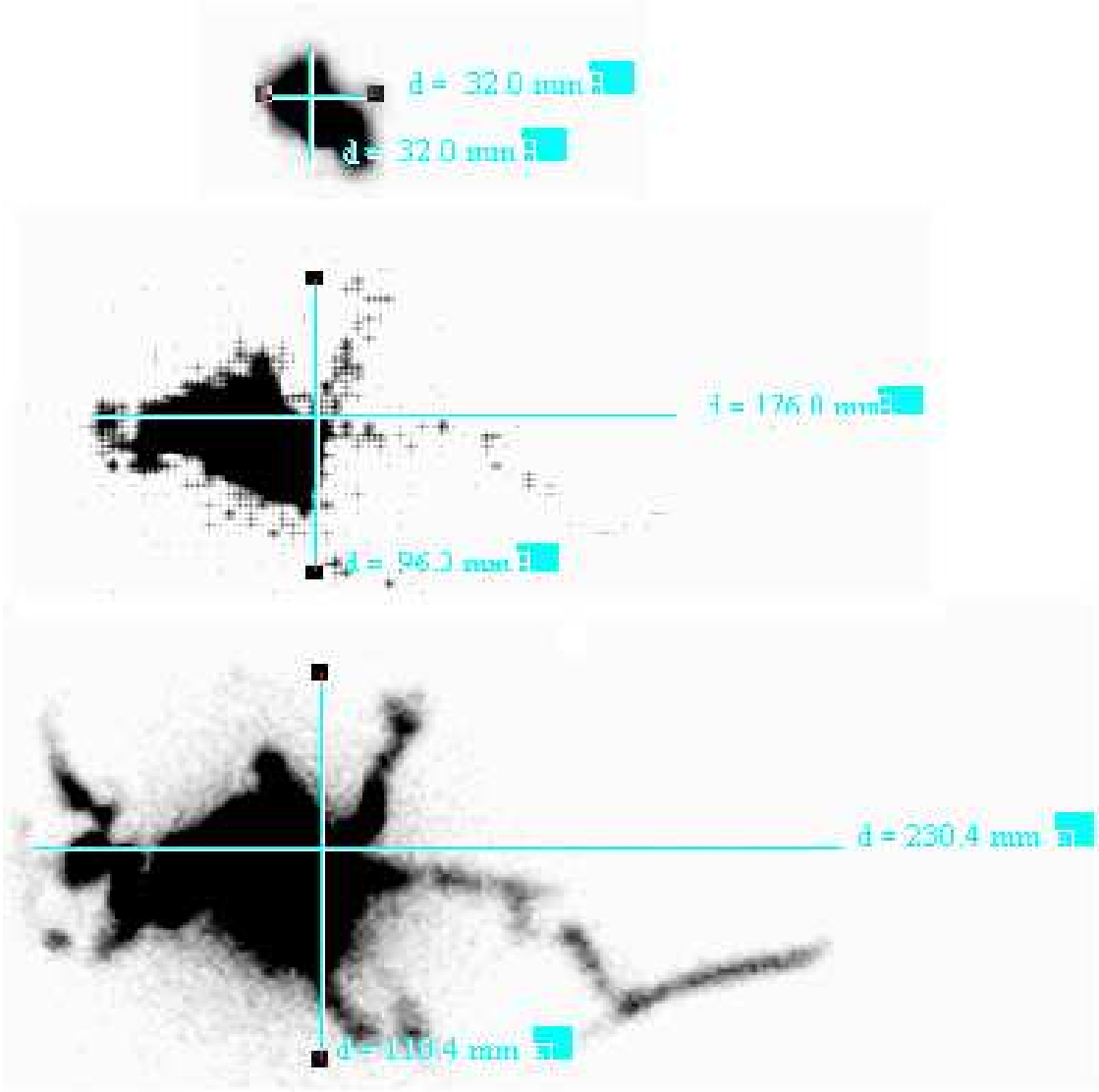

Figure 4.16: Ex-vivo bovine liver tissue, a tagged isotope is injected in the ablation volume to analyse the movement of fluid during microwave ablation for an input power setting of 100 watts for 3 minutes [30]

resistance path, such as a blood vessel. If a fluid moves radially, it means that a pressure gradient exist through the ablation zone. This pressure gradient is due to a elevation of temperature and water vapor generation in the ablated zone.

4.6.4 Energy required to vaporize water

For the 2.4 mm open loop applicator, a small amount of water, (flow rate from 120 mlh^{-1} to 180 mlh^{-1}) terminates in the tissue near the ablation volume in order to cool the shaft. For a typical 5 minutes thermal ablation, the amount of water deposited

is between 10 ml and 15 ml. If a too large quantity of water is in the ablation volume, there is a potential risk of hot fluid movement along a low resistance path, such as veins or arteries, generating a potential burn outside the ablation zone. However, external water in the volume ablation maintained the tissue wet and improve the overall efficiency of the thermal ablation process. The large latent heat of water limits the temperature of the tissue between 100 °C and 120 °C as the transformation of water to vapor requires a large amount of energy. Nevertheless, the undesirable and unpredictible potential burns from hot fluid movements along vessels gives a preference to a closed loop cooled applicator which avoids water drainage in the ablation zone.

It is instructive to calculate the amount of energy required to transform 10 ml of water into vapour. The vaporization temperature of the fluid inside the tissue is assumed to be 100 °C. The energy required to heat 10 ml of water from body temperature to 100 °C is:

$$Q_1 = mC_p\Delta T = 0.01 \times 4198 \times (100 - 37) = 2645\ J \tag{4.11}$$

m is the mass of the water and C_p is the specific heat of water. The energy required to transform this mass of liquid water at 100 °C to vapor at 100 °C is:

$$Q_2 = mH_{fg} = 0.01 \times 2257000 = 22570\ J \tag{4.12}$$

H_{fg} is the latent heat of vaporization taken from Incropera and Dewitt [38]. Transformation of liquid water to vapour requires a large amount of energy due to the phase change. In this case, the amount of energy necessary to vaporize the water is nearly 10 times higher then the energy used to heat the water inside the tissue from 37 °C to the boiling point at 100 °C. For example, for 60 watts of microwave energy absorbed in the tissue for 5 minutes, the total energy is $E = 18000\ J$. This means that only a fraction of liquid water could be vaporized.

During the development of this applicator, the exit holes for the water exit were placed a few centimetres away from the radiating tip, in order to decrease the quantity of liquid in the ablation volume. The drawback of this modification of the location of the holes is that the coaxial cable after these holes is not as cool and the temperature of radiating section components is higher than the version with the holes closer to the copper ferrule.

For some organs such as lung, bone and brain, water deposition is not desirable. For this reason and the wish to minimize potential hot fluid movement in surrounding capillaries, veins or arteries network, the need of a closed loop cooling applicator appears.

4.7 Summary

The 2.4 mm applicator has been developed over the last 4 years in the Medical Technology Group at Bath University, it allows liver ablation up to 5 centimetres in diameter

at 80 Watts in 4 minutes. It is a thin device and may be used for percutaneous surgery or interventional radiology.

To minimize hot fluid movements in liver organ and to increase the range of thermal ablation on different organs, a gas cooling circuit has been developed and implemented for both applicators which is described in the next following chapters.

Chapter 5

Air filled coaxial cable

5.1 Introduction

In this chapter a design for the cooling circuit of a closed loop applicator is presented which avoids the deposition of the cooling fluid in the ablation zone. Water is an efficient cooling fluid due to the large thermal specific heat. However, because of its electric conductive properties and dielectric properties, water cannot be used inside a coaxial cable.

The choice of a gas as the cooling fluid allows the use of the space between the inner and outer conductor of the coaxial cable and therefore the construction of a small shaft diameter applicator. An important constituent of the gas cooled applicator is an air filled coaxial cable which allows space for the passage of the cooling gas. The cable is composed of an inner copper wire conductor and outer hollow copper tube conductor. The air filled coaxial cable is required to transmit microwave energy to the radiating section with low loss and the gas has to sufficiently cool the shaft and the internal part of the applicator.

An important parameter of any cable is its characteristic impedance. To achieve an efficient microwave energy transmission from the source to the antenna with low reflected power, the characteristic impedance should match that of the flexible feed cable between the source and the applicator. In this chapter the characteristic impedance is calculated and the effect of small holes in the coax outer conductor of the coax cable is investigated by determining the reflection coefficients or S parameters.

A fluid and thermal analysis of the overall circuit is also performed in order to show that gas cooling is a feasible solution. Temperatures along the shaft were recorded in steady state and transient condition for different flow rates. This technical solution has been implemented for the 2.4 mm and 5 mm applicators and is described in chapter 6 and chapter 7.

The use of gas such as air or CO_2 as a cooling fluid for medical device has been implemented on some medical devices. Yeh et al [83] have developed and tested an intracavitary

microwave antenna array system with air cooling system for the hyperthermia treatment of prostate cancer. Eppert and Trembly [23] investigated theoretically and experimentally the effect of air flowing between an interstitial microwave antenna and a catheter. Deardorff *et al* [18] have studied and developed an air cooled ultrasound applicator for interstitial hyperthermia, showing that the use of an internal air flow lowers the surface temperature of the applicator increasing the radial depth of therapeutic heating since the applicator can be used at higher ultrasound energy.

At the time of writing, an air coaxial cable used for the closed loop cooling circuit of the percutaneous applicator has not been implemented elsewhere.

5.2 Electromagnetic properties of the coaxial line

In this section, the effect of the geometry of the air filled coaxial cable on the microwave propagation and the variation of impedance with the eccentricity of the inner conductor is discussed.

5.2.1 Geometry

The coaxial cable considered consists of a copper centre conductor insulated by a polytetrafluoroethylene (PTFE) heat shrink tubing (Adtech polymer PTFE 0.86-0.38 mm) with diameter 0.9 mm surrounded by an outer copper hollow tube conductor of inner diameter 1.5 mm. The gap between the two conductors forms an eccentric annular channel for a cooling gas flow, as shown in figure 5.1

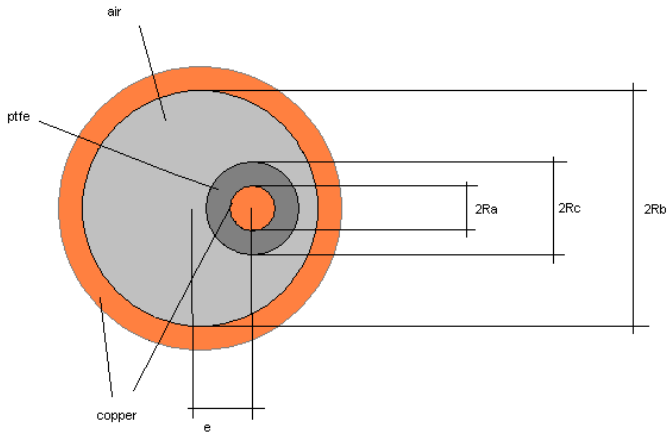

Figure 5.1: Dimensions of the eccentric coaxial line Ra = 0.25 mm, Rb = 0.75 mm, Rc = 0.45 mm

5.2.2 The characteristic impedance

Transmission line equations describe the behaviour of voltage and current waves along a transmission line given the geometry and electrical properties of the materials. Solutions for the current and voltage wave equations have two terms corresponding to incident and reflected travelling waves. The ratio between the amplitude of the incident voltage wave and incident current wave at any point on the line is called the characteristic impedance. In order to minimize power reflection from a termination the characteristic impedance needs to be matched to the network or load connected to the transmission line.

An air filled coax line has minimum attenuation for characteristic impedance of 77 Ω and the maximum power capacity due to voltage breakdown occurs for 30 Ω impedance. A characteristic impedance of 50 Ω gives a compromise between minimum attenuation and maximum power capacity [57]. Value of the ratio between the outer conductor and inner conductor $\frac{R_b}{R_a}$ for minimum attenuation and maximum power capacity are described in appendix E.

Normally in an air filled coax the inner conductor must be central. However in our design, the inner conductor is unsupported leading to an eccentricity relatively to the outer conductor. The variation of characteristic impedance with the eccentricity of the centre conductor was investigated and it was shown that the eccentricity has a small influence on the characteristic impedance.

To calculate the impedance of a coaxial line shown in figure 5.1 with a diameter of 0.5 mm for the center conductor and 1.5 mm for inner conductor a model was created with a finite element package (HFSS, Ansoft®). The characteristic impedance was calculated for different values of eccentricity.

The variation of the characteristic impedance with the eccentricity of the inner con-

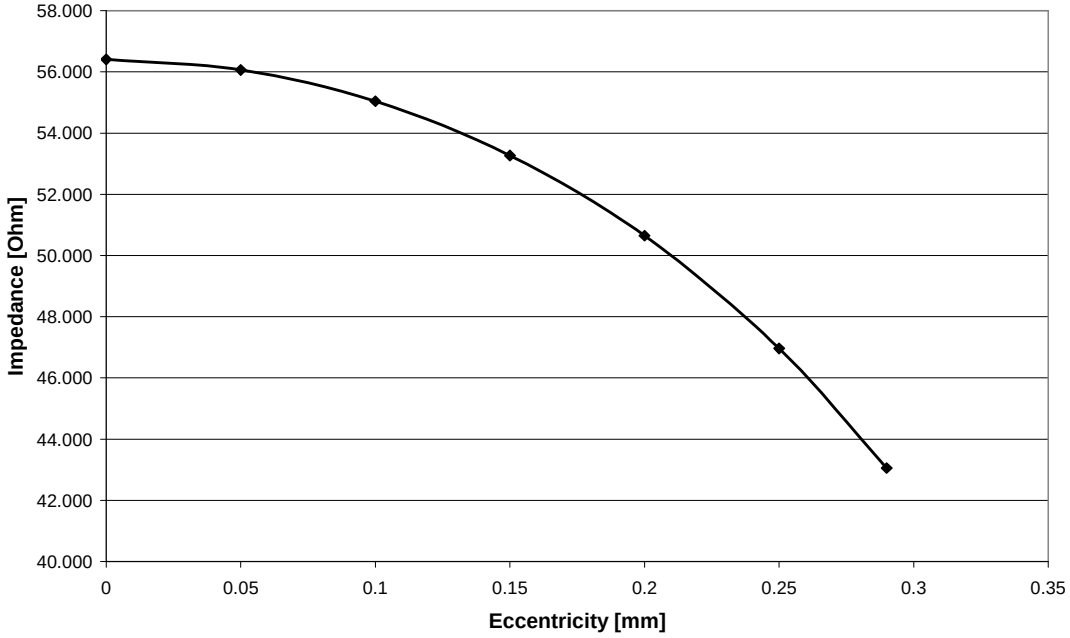

Figure 5.2: Variation of the characteristic impedance with the inner conductor ecccentricity

ductor is plotted on the graph in figure 5.2. The x axis is the eccentricity distance from the center of the coaxial cable. The y axis is the amplitude of the characteristic impedance. A parametric analysis was performed for different values of eccentricity and the characteristic impedance calculated for each configuration.

In figure 5.3, the characteristic impedance relative to the impedance with zero eccentricity is plotted against the relative eccentricity. It can be seen that the characteristic impedance is not very sensitive to distance variation. For example a 50 % distance variation results in a 14 % decrease in the impedance.

An analytical calculation of the characteristic impedance of an eccentric coaxial cable was also performed in Appendix D. It gives a very good agreement between the numerical results and the analytical calculation. For the purposes of this calculation, copper can be considered as a perfect conductor. The characteristic impedance is calculated as the square root of the ratio of the inductance over the capacitance per unit length. The calculated value is 56.4 Ω for the centred air coaxial line of figure 5.1. In his paper Das et al [16] gives two methods using conformal transformation to calculate the impedance of an eccentric coaxial cable with a dielectric surrounding the eccentric centre conductor. In appendix D a conformal transformation method used by Das *et al* [16] is employed to calculate the characteristic impedance with respect to the eccentricity of the center conductor.

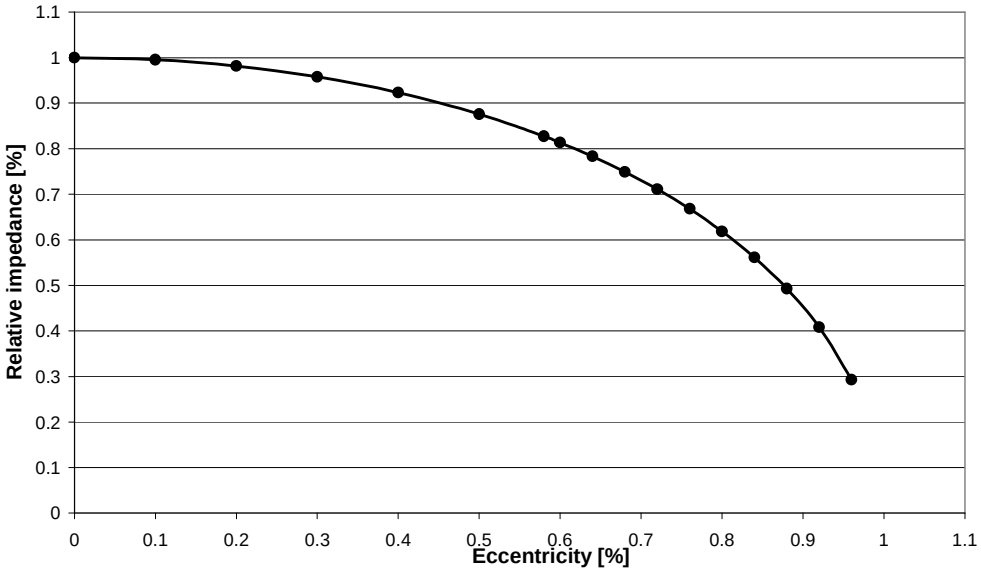

Figure 5.3: Relative impedance against of centered relative distance

5.2.3 Gas input and output to the cable

The low sensitivity of impedance with the eccentricity distance allows the use of this type of cable with an inner conductor not exactly centered in the middle of the outer conductor in the building of an air cooled applicator. A second major modification of the basic gas cable is the presence of four holes located at both extremities in order to have a gas input and output to the cable.

Four holes of 0.6 mm diameter were drilled at both ends of the coax. The configuration analysed consisted of two pairs of diametrically opposite holes of diameter 0.4 to 0.6 mm aligned on orthogonal axes with a distance between the axes varying from 1 to 6 mm as shown in figure 5.4. This range of distance is the distance gap used during the realisation of the prototype.

5.2.3.1 Model set up

To measure the effect of the four holes on the electromagnetic wave propagating inside the coaxial cable, a finite element model (HFSS, Ansoft®) was used to calculate the reflection coefficient on the input and output ports located at both ends of the coax cable. The first port is defined by the area located at the entrance of the coaxial cable between the two conductors. This area includes the dielectric and air material. The second port is defined by the same area, but is located at the other extremity of the coax cable.

A parametric analysis was performed for holes with radii of 0.2 mm and 0.3 mm and the distance between each pair of holes varying from 1 to 6 mm by increments of 1 mm to determine the influence of these holes on the reflection coefficient for different

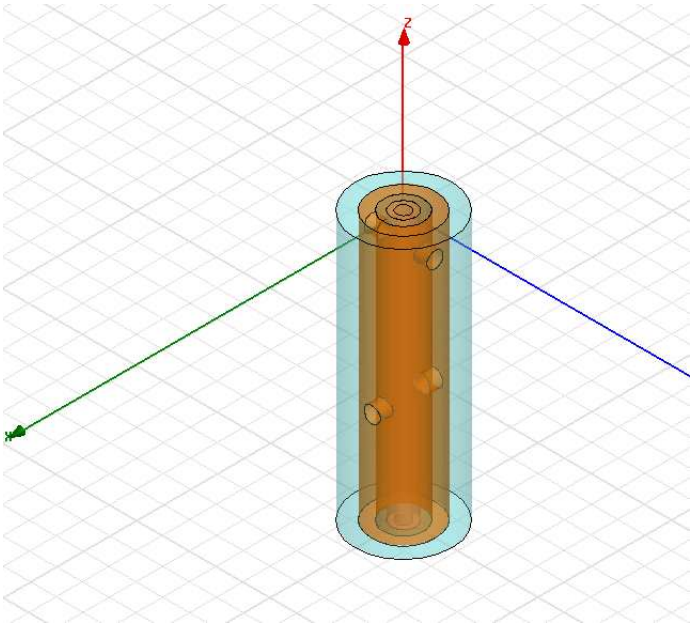

Figure 5.4: Coaxial line with holes

configurations.

$|S_{11}|$ is the ratio between the reflected voltage wave and incident voltage wave at a given port or reflection coefficient. The incident power and reflected powers are expressed as a function of the voltage: $P_{inc} = \frac{V_i^2}{2Z_0}$ and $P_{refl} = \frac{V_{refl}^2}{2Z_0}$. Hence the ratio of incident and reflected power is equal to the square of the magnitude of the S_{11} parameter:

$$\frac{P_{refl}}{P_{inc}} = \frac{V_r^2}{V_i^2} = |S_{11}|^2 \tag{5.1}$$

5.2.3.2 Results

Results showed that the higher value of the S_{11} for port 1 occurs for a distance $d = 6\,mm$ and radius of $0.3\,mm$ for the hole. S_{11} is 0.0041 or -47.7 dB inferring that very little microwave energy is reflected back along the coaxial wave guide.

A second model was defined by using four ports to evaluate the microwave leakage around the coaxial cable. Ports 1 and 2 are the input and output port as defined previously. Port 3 is located at z = 0 and is the area between the outside coax and the air, port 4 is located at the end and is defined by the area between the coax and the surrounding air. S_{13} gives the ratio of the transmitted voltage wave located at port 3 over the incident voltage wave located at port 1. The scattering matrix obtained for the magnitude of S

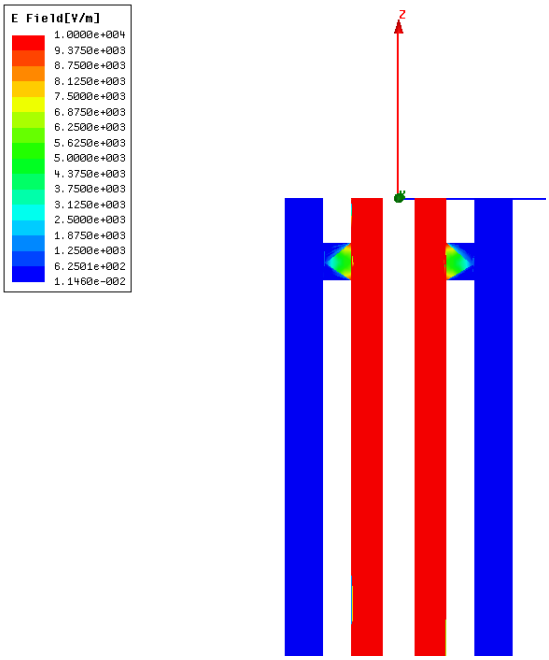

Figure 5.5: Time average electric field for holes at 1 mm location

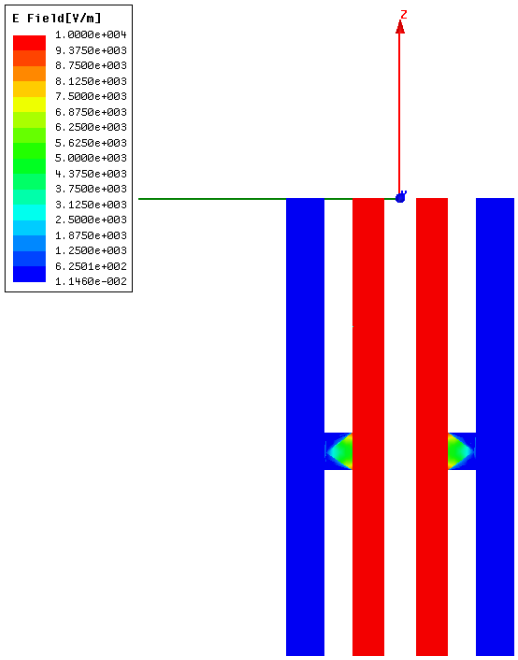

Figure 5.6: Time average electric field for holes at 6 mm location, the red zone is where the field is higher than 10000 V/m

parameters is given below:

$$\begin{pmatrix} |S_{11}| & |S_{12}| & |S_{13} & |S_{14}| \\ |S_{21}| & |S_{22}| & |S_{23} & |S_{24}| \\ |S_{31}| & |S_{32}| & |S_{33} & |S_{34}| \\ |S_{41}| & |S_{42}| & |S_{43} & |S_{44}| \end{pmatrix} = \begin{pmatrix} 0.0036 & 0.99 & 0.000013 & 0.00012 \\ 0.99 & 0.0036 & 0.00005 & 0.000021 \\ 0.000013 & 0.000005 & 0.77 & 0.084 \\ 0.00012 & 0.000021 & 0.084 & 0.77 \end{pmatrix}$$

The $|S_{21}|$ parameter is the ratio between the transmitted voltage wave at port 2 and the incident voltage wave sent from port 1. The value for $|S_{21}|$ is nearly 1 and it shows that the four small holes have little effect on the electromagnetic loss in the coaxial cable. $|S_{31}|$, $|S_{32}|$, $|S_{41}|$, $|S_{43}|$ are ratios between transmitted waves at port 3 and 4 from air surrounding the coax and incident waves sent at port 1 and 2 of the coaxial cable. They have very low amplitude suggesting that most of the microwave energy propagates inside the wave guide.

5.2.4 Cable connector

The connection to the air filled coaxial cable is made with a standard SMA connector. To build an air coax cable, the connector was dismantled from a standard coaxial cable and then connected with solder manually. There is little reflection due to the mismatch of impedance between the PTFE standard line 50 Ω and the 56 Ω air filled line.

The total voltage and current on the line are the sum of incident and reflected waves [58]:

$$V(z) = V_0^+ e^{-j\beta z} + V_0^- e^{j\beta z} \tag{5.2}$$

$$I(z) = \frac{V_0^+}{Z_0} e^{-j\beta z} - \frac{V_0{}^-}{Z_0} e^{j\beta z} \tag{5.3}$$

where V_0^+ and V_0^- are the amplitude of the incident and reflected wave at the origin $z = 0$, β is the imaginary part of the propagation constant, assuming a lossless transmission line, the real part of the attenuation constant is zero. Z_0 is the characteristic impedance of the coaxial line. The load impedance can be expressed in function of voltage and current:

$$Z_L = \frac{V(0)}{I(0)} = \frac{V_0^+ + V_0^-}{V_0^+ - V_0^-} Z_0 \tag{5.4}$$

The amplitude of the reflected wave V_0^- is :

$$V_0^- = \frac{Z_L - Z_0}{Z_L + Z_0} V_0^+ \tag{5.5}$$

In our case, the standard PTFE line has an impedance $Z_0 = 50\,\Omega$ and the connected air coaxial line can be considered as the load with an impedance $Z_L = 56\,\Omega$. Hence, the coefficient can be calculated with 5.5:

$$\Gamma = \frac{V_0^-}{V_0^+} = \frac{56 - 50}{56 + 50} = \frac{6}{106} = 0.056 \tag{5.6}$$

The reflection coefficient due to the interface PTFE and air is less than 0.06, so there is little microwave reflection at the connector junction.

In the next part, a thermal analysis was performed when air was flowing inside the coaxial cable in order to test if the gas had enough cooling capacity for the applicator.

5.2.5 Conclusion

There is some electric field leakage through the holes, but the field attenuates quickly from high field intensity inside the coax to low field intensity, below a few hundred volts per meter, inside the air holes. Outside the region of the holes, the field is approximately 0 as shown in figure 5.5 and figure 5.6.

Because the diameter of the four holes is much smaller than the wavelength, it was established that most of the microwaves propagate inside the coaxial cable and little microwave energy leaks through the holes. For this reason, an air filled coaxial cable could be used for both microwave transmission and internal cooling. Overall, the air filled coaxial cable is an efficient wave guide and is appropriate for the 2.4 mm applicator.

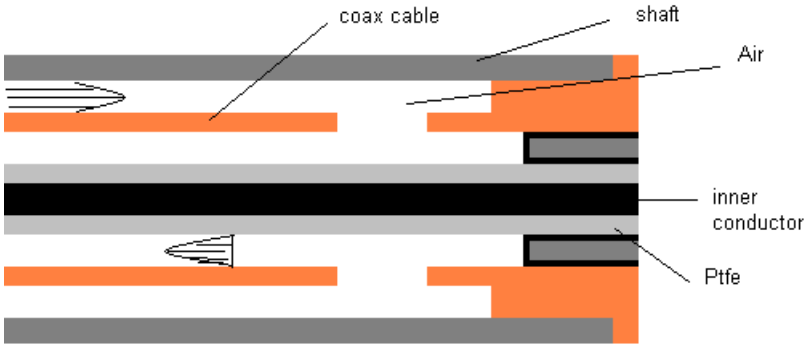

Figure 5.7: Double counter flow geometry of the gas cooled applicator

5.3 Temperature measurements of the shaft

To assess the cooling efficiency of an air flow inside the coax cable and between the shaft and the coax, a series of temperature measurements along the shaft was performed for different flow directions and flow rates.

5.3.1 Geometry

The geometry of the gas cooling circuit is composed of the air filled coaxial cable and the shaft. The air flows in the annular space between the inner and outer conductor of the coaxial cable and then flows through the annular space between the outer conductor and the shaft. This geometry for the gas cooling circuit is a double annular counter flow heat exchanger and is shown in figure 5.7.

5.3.2 Experimental set up

Measurements of temperature of the shaft were performed to evaluate the effectiveness of the gas flow to cool the shaft and to compare temperature values with the model. A temperature of 100 °C was applied on the ceramic with an oil bath at 100 °C.

5.3.2.1 Location of the thermocouples on the shaft

The shaft was insulated with polystyrene material and eight thermocouples were attached with aluminium tape at given locations as indicated in figure 5.8. Figure 5.9 shows the locations of the thermocouples near the ceramic tip and the overall device insulated with polystyrene material is shown in figure 5.10.

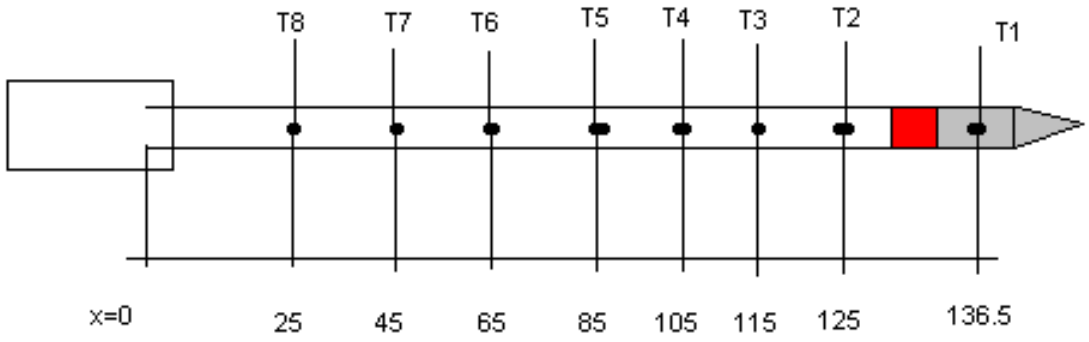

Figure 5.8: Location of thermocouples with distance interval

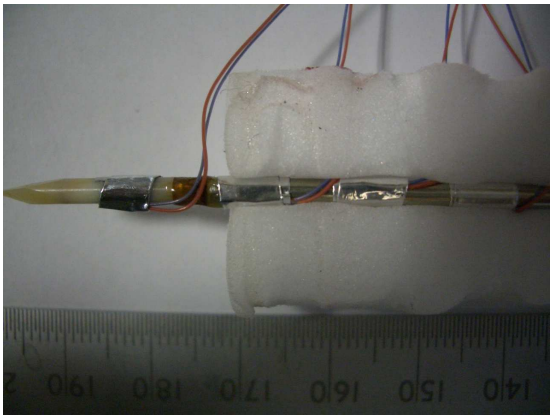

Figure 5.9: First three thermocouples near the radiating section

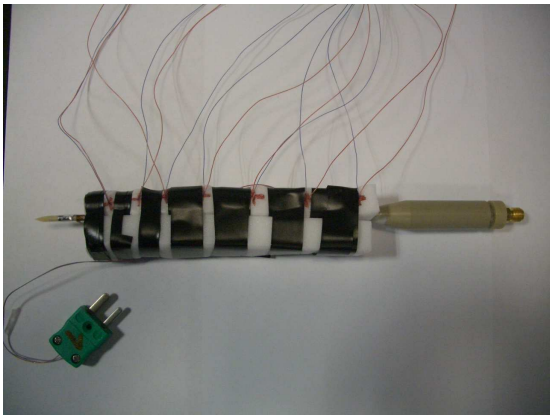

Figure 5.10: Thermocouples along the insulated shaft

5.3.2.2 Heat source

The heat source was a vegetable oil bath maintained at 100 °C with an electric hot plate as shown in figure 5.11. A stirring magnet allowed the maintenance of 100 °C on the ceramic tip of the applicator as shown in figure 5.12.

A sheet of polystyrene was inserted between the oil surface and the copper ferrule in order to minimize hot air convection with consequential heat transfer to the ferrule. For the same reason, a piece of cardboard was put between the oil bath and the applicator.

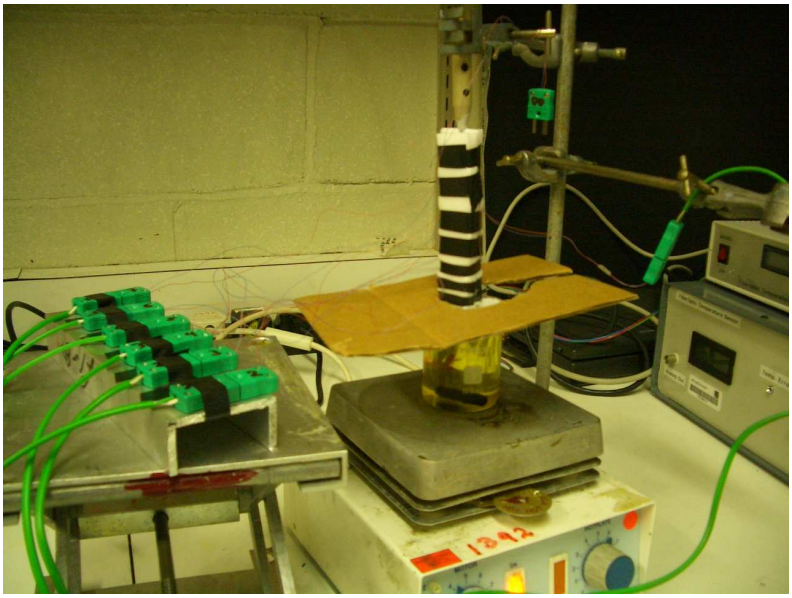

Figure 5.11: Installation with the electric hot plates

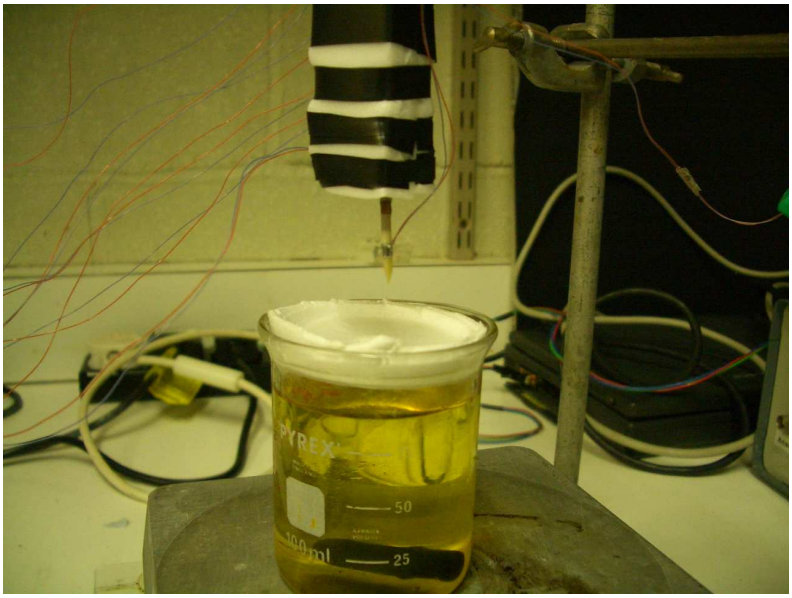

Figure 5.12: Vegetable oil bath at 100 °C with a stirring magnet

5.3.2.3 Instruments

The air pressure was measured at the output of the compressed air bottle with a gauge pressure transducer (Gems® 010VDC, 0 to 4 bars). This sensor gives an output voltage proportional to the pressure difference between the input and atmospheric pressure. The voltage output is 0 to 10 volts full scale and the pressure range is from 0 to 4 bars.

The volume flow rate was measured with a thermal mass flow meter (Red y, Vogltin Instruments®). The sensor gives a voltage output proportional to the mass flow rate inside the device. The principle of operation of the mass flow meter is based on a thin wire that is maintained at constant temperature while the gas flows through the tube. The electric power expended to maintain the wire at constant temperature is proportional to the mass flow rate. The mass flow meter was calibrated for Air and CO_2 and for volume flow rates at standard conditions from 0 to 10 $lmin^{-1}$. The pressure transducer and the thermal mass flow meter sensor are shown in figures 5.13 and 5.14.

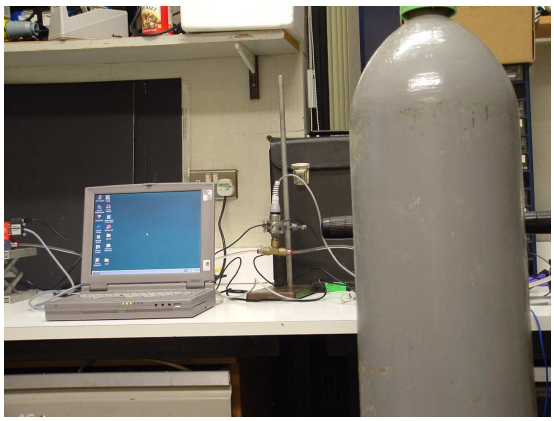

Figure 5.13: Pressure sensor and compressed air bottle

Figure 5.14: Thermal mass flowmeter Red y, Vogltin instruments®

5.3.3 Measurement inaccuracy

Imprecision for the temperature measurements comes from mainly three sources:
- the thermocouples give a measurement inaccuracy of $\pm 1\,°C$. The estimated overall temperature inaccuracy was assumed to be $\pm 1.5\,°C$.
- the thermocouples are located on the shaft with aluminium tape, the spatial error is around $\pm 2\,mm$.
- the temporal error at the start of the transient measurement was estimated around $\pm 1\,s$.

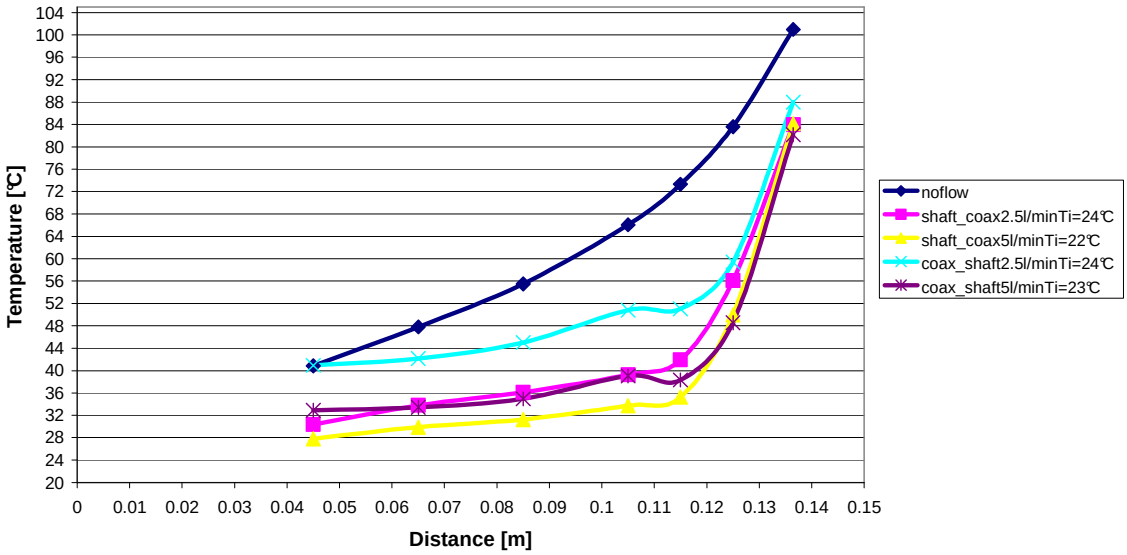

Figure 5.15: Measured temperature along the shaft, input temperature: 23 °C

5.3.4 Measured temperatures in the steady state regime

Temperature measurements were performed with the seven thermocouples along the shaft. Thermal equilibrium was achieved and for each thermocouple, the temperature was averaged over a time period of 20 seconds. Then the temperature was plotted versus the distance along the shaft by interpolating the temperature values between each thermocouple. The first thermocouple recording the temperature shaft was located at 4.5 cm from the gas entrance which was inside the handle. For this reason, all measured temperatures started at 4.5 cm from the gas entrance.

There were two possible directions for the gas to flow inside the applicator. If the gas flows first between the shaft and the coax and returns inside the coax, the direction of the flow will be designated as direction shaft/coax. Similarly, if the gas flows first inside the coax and then returns in the annular space between the shaft and the coaxial cable, the flow direction will be designated as direction coax/shaft.

5.3.4.1 Air entry at room temperature

In figure 5.15, temperature along the shaft is plotted when no air is flowing inside the device and for four different configurations at room temperature. As expected, temperatures are lower with a flow rate of 5 $lmin^{-1}$ (yellow and brown curves) compared with a flow rate of 2.5 $lmin^{-1}$ (blue light and pink curves).

The configuration where the air flows first between the shaft and the coaxial cable and then goes back inside the coax is more efficient to cool the shaft. The difference is shown in figure 5.15 by comparing the blue curve and pink curve for a flow rate of 2.5 $lmin^{-1}$

and the yellow and brown curve for a flow rate of $5\,lmin^{-1}$.

Until a distance of 11 cm from the origin, temperature of the shaft is maintained below 52 °C for a flow rate of $2.5\,lmin^{-1}$ in the coax-shaft configuration (blue curve) and below 40 °C for the shaft-coax configuration (pink curve).

With a flow rate of $5\,lmin^{-1}$, the temperature remains below 38 °C for the coax-shaft configuration (brown curve) and below 35 °C for the shaft-coax configuration (yellow curve).

In the region $11\,cm \leq x \leq 12\,cm$ there is a local minimum on the temperature-distance curve for the direction of flow coax/shaft with a flow rate of $2.5\,lmin^{-1}$ and $5\,lmin^{-1}$ as shown by the light blue and brown curve in figure 5.15. At this particuliar location $x = 11.5\,cm$ the temperature is approximatly between 1 °C and 3 °C lower than the surrounding points. The location of air holes at $x = 11.5\,cm$ explains this local minimum of temperature. At this particular location, the totality of the air flow moves in the radial direction and cools directly the shaft wall. This phenomenon does not occur in the configuration shaft/coax because the gas flow remains parallel to the shaft in the annular channel and then enters inside the coaxial cable through the holes.

5.3.4.2 Air entry at −20 °C

In a second experiment, the input air was cooled to −20 °C and the flow rate was set to $5\,lmin^{-1}$. Both configurations of direction of flow were tested. As shown in figure 5.16, the temperature of the shaft remains below 13 °C for the coax-shaft configuration (pink curve) and below 1 °C for the shaft-coax configuration (yellow curve).

Measurements of temperature in steady regime show that a cold air flow efficiently cools the shaft of the applicator. For low temperature gas entry, the direction of flow coax/shaft is preferred to the direction shaft/coax because it avoids a too low temperature of the shaft that could be potentially harmful for the normal surrounding tissue during the percutaneous procedure.

For the same reason as described in the case at room temperature, the pink curve from figure 5.16 outlines a local minimum near $x = 12\,cm$ which is due to the direction coax/shaft of the flow and the location of the air holes in the coaxial cable.

5.3.4.3 Conclusion

An air flow of $2.5\,lmin^{-1}$ and $5\,lmin^{-1}$ at room temperature of 22 °C cools signifcantly the coax cable and the steel shaft. The difference of temperature between the uncooled coax and the configuration with an air flow of $5\,lmin^{-1}$ is 24 °C at 4 cm from the heat source.

As expected, a higher flow rate extracts more heat and maintains a lower shaft tem-

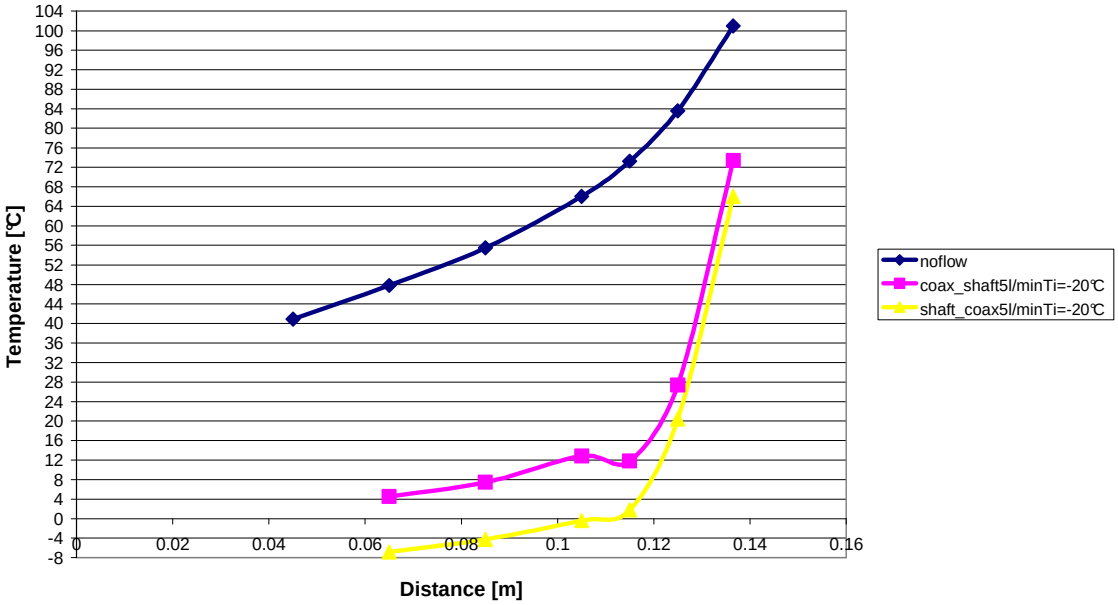

Figure 5.16: Measured temperature along the shaft, input temperature: $-20\,^{\circ}\mathrm{C}$

perature. The configuration shaft/coax gives a lower temperature ($2\,^{\circ}\mathrm{C}$ to $4\,^{\circ}\mathrm{C}$) than the configuration coax/shaft.

At $-20\,^{\circ}\mathrm{C}$ entry temperature, the configuration shaft/coax is prefered to avoid excessively cool temperatures on the shaft.

Flow rate and air entry temperature of air are the two main factors that affect the shaft temperature. A higher flow rate decreases the magnitude of the temperature gradient in the axial direction.

The air entry temperature is the initial condition of the temperature field and does not affect the temperature profile. It has a tendency to shift the curve in the vertical direction of the graphs.

The flow rate is direclty related to the velocity field, as the flow rate increase the temperature gradient decrease.

These two observations are consistent with the equation 2.83 from the theory of chapter 2.

5.3.5 Measured temperature in transient regime

Temperature was recorded for each thermocouple when the applicator was plunged into the oil bath. This could simulate the heat source coming from a microwave ablation when a sudden amount of energy is deposited in the tissue creating a fast temperature rise.

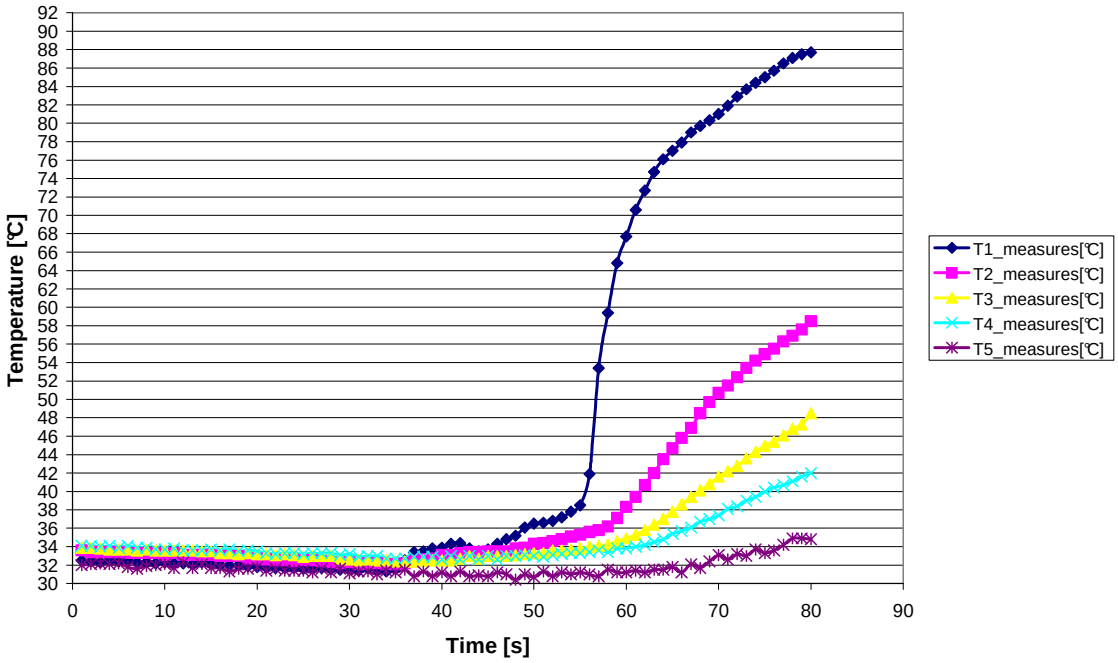

Figure 5.17: Measured temperature in transient regime with no Air flow

5.3.5.1 Initial conditions

Measurements were performed with no air flow and with an air flow of $5\,lmin^{-1}$ with air entry at room temperature. The temperature of the oil bath was 100 °C.

Location of thermocouples are given by figure 5.8 with the first thermocouple along the shaft was thermocouple T7 at 4.5 cm from the origin of the tube.

5.3.5.2 No air flow

The ceramic tip of the applicator was immersed in oil while shaft temperatures were recorded. Temperature measurements are shown in figure 5.17 for the case with no air flow. The rate of temperature change at a given thermocouple location decrease as the distance between this thermocouple and the ceramic tip increase. By comparing the slope of the blue, pink and yellow curves of figure 5.17 respectively associated with thermocouple T1, T2 and T3, the rate of temperature of T1 is higher than T2 which is higher than T3.

If the coax and shaft were perfect thermally conducting material with zero thermal heat capacity and with adiabatic boundaries with the environnment, the rate of temperature change for each thermocouple along the shaft would be the same. As the constant heat flux propagates through the beam, the mass of material with a finite thermal and specific heat increases linearly with the length. The energy conservation implies that the temperature change is smaller far from the heat source than closer to the heat source. From table 5.1, a significant increase of temperature for T1 and T2 can be seen whereas the increase

Temperature [°C] — Time [s]	t = 55	t = 60	t = 65
T1 [°C]	38.5	67.7	77
T2 [°C]	35.3	38.3	44.7
T3 [°C]	33.8	34.9	37.8
T4 [°C]	33.3	33.8	35.4
T5 [°C]	31.2	31.2	31.8

Table 5.1: Transient temperature measurements, no air flow

is less for T4 to T5. After 20 seconds of immersion, temperatures still increase, a longer time is needed to reach a thermal equilibrium.

5.3.5.3 Air flow $5\,lmin^{-1}$

In figure 5.18 temperature measurements were performed with a flow rate of $5\,lmin^{-1}$ with an input temperature at room temperature. The small plateau recorded by thermocouples T1 located on the ceramic is due to the manipulation of the device during its insertion in the hot oil bath.

By comparing the run with no flow and with an air flow of $5\,lmin^{-1}$, the cooling effect of the gas is clearly shown. For example, the temperature of thermocouple T2 is 58 °C at the end of the run with no flow, and remains below 44 °C with air cooling. For thermocouple T3, the temperature is 48 °C at the end of the run with no cooling and remains below 32 °C with cooling.

For the thermocouples located at the end of the applicator, the increased of temperature is smaller, the increases of temperature for thermocouples T4 and T5 is approximately 4 °C.

The table 5.2 gives the temperature evolution for the different thermocouples before and after the thermal impulse. The increase of temperature for T1 and T2 is respectively 40 °C and 11 °C in 10 s time. The temperature increase of thermocouple T3, T4 and T5 is less than 2 °C.

The temperature of the ceramic given by thermocouple T1 remains around 75 °C with air cooling. The ceramic is in contact with the copper ferrule branch and the copper is cooled by the air flowing inside the coax.

20 seconds after immersion, temperatures become stabilized and the system reaches a thermal equilibrium.

5.3.6 Conclusion

Temperature measurements along the shaft for two different flow rates and two directions show that an air flow significantly cools the shaft.

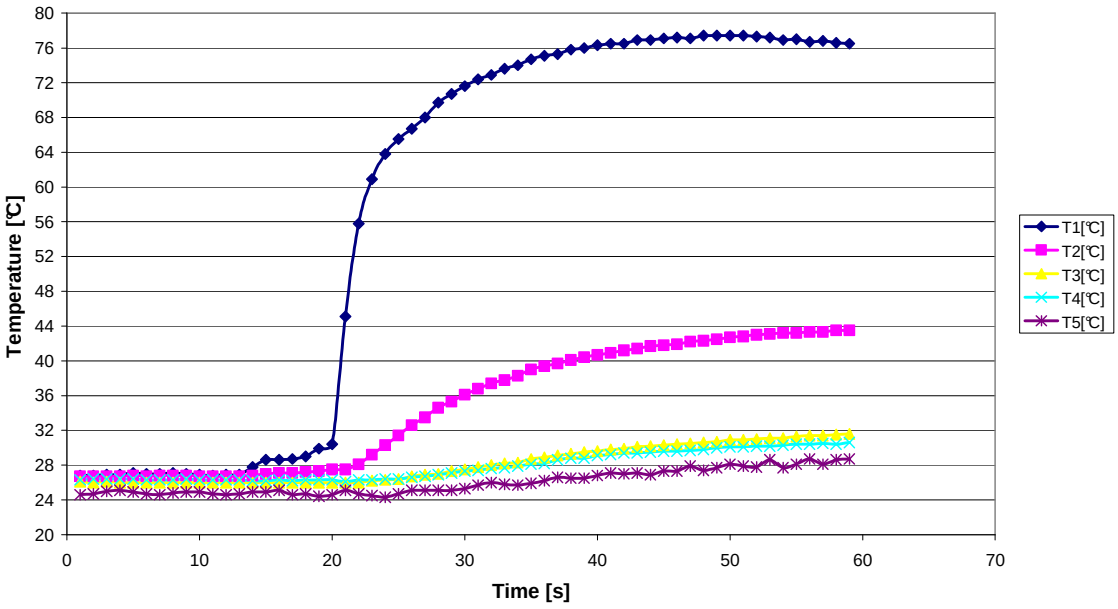

Figure 5.18: Measured temperature for a flow rate of 5 $lmin^{-1}$ in the direction shaft coax

Temperature [°C] — Time [s]	t = 20	t = 25	t = 30
T1 [°C]	30.4	65.5	71.6
T2 [°C]	27.5	31.4	36.1
T3 [°C]	26	26.4	27.5
T4 [°C]	26.3	26.4	27.3
T5 [°C]	24.6	24.7	25.3

Table 5.2: Transient temperature measurements, air flow 5 $lmin^{-1}$

For both steady and transient measurements, an increase of flow rate tends to flatten the temperature profile curve. It means a smaller temperature gradient $\frac{\delta T}{\delta z}$ at higher flow rate for the steady case and a smaller rate of temperature change $\frac{\delta T}{\delta t}$ for the transient case.

The entry gas temperature set the origin of the curves in the temperature distance plot and does not affect the temperature profile.

In the next section, the flow regime characteristic are discussed in order to calculate the temperature by solving the thermal diffusion equation for the fluid and solid domain of the geometry with a finite element model package.

5.4 Characteristic of the flow

The type of flow regime is determined by the geometry of the channel, the physical properties of the fluid and the mean velocity. The Reynolds number is an adimensional

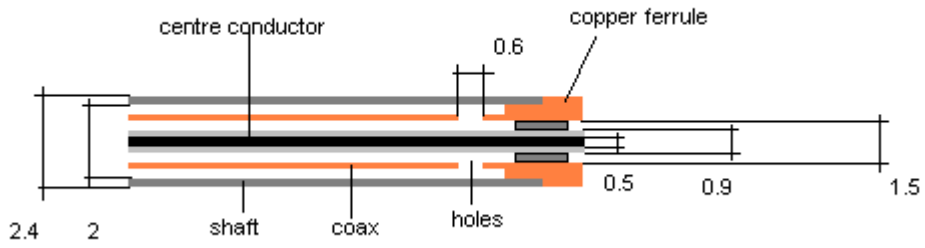

Figure 5.19: Schematic of the cooling circuit of the applicator

number which allows us to know if the fluid is in a laminar or turbulent regime.

When a pressure wave pertubation propagates much faster than the mean velocity of the gas flow, the gas can be consider incompressible. The incompressibility assumption facilitates the calculation for the fluid and thermal solutions.

5.4.1 Geometry

The geometry of the cooling circuit analysed shown in figure 5.19 is comprised of two hollow tubes: a coaxial cable and a hollow stainless steel tube. The cooling circuit is a closed counter flow exchanger with two annular channels. The central line is formed from the center conductor insulated with a PTFE heat shrink tube.

The first channel is defined by the annular space between the centre conductor including the PTFE layer of radius $r_i = 0.45\,mm$ and the coax cable with an inner radius $r_i = 0.75\,mm$.

The second channel consists of the annular space between the coax cable of outer radius $r_0 = 0.9\,mm$ and the steel shaft of inner radius $r_i = 1\,mm$.

The connection between the two channels for the gas is made through two small holes in the outer conductor of the coaxial cable.

5.4.2 Area of the annular channels

The area for the channel inside the coaxial cable is:

$$A_i = \pi(0.75^2 - 0.45^2) = 1.13\,mm^2 \tag{5.7}$$

The area for the channel between the coax and the shaft is:

$$A_o = \pi(1^2 - 0.9^2) = 0.59\,mm^2 \tag{5.8}$$

The mean velocity inside a channel is related to the flow rate $\dot{V}$and the area A by:

$$v_m = \frac{\dot{V}}{A} \tag{5.9}$$

Channel	Hydraulic diameter[mm]	Mean velocity $[m^{-1}]$	Reynolds number
Inside coax	0.6	73.7	2782
Shaft/coax	0.2	140	1761

Table 5.3: Reynolds number for the two channel with an Air flow of $5\,lmin^{-1}$

5.4.3 Reynolds number

To determine the regime of a flow, the Reynolds number which is the ratio between viscous forces and inertial forces is calculated. Depending on its value, the flow is laminar or turbulent.

It is possible to increase the heat transfer between the gas and the shaft by using a turbulent regime instead of laminar regime. Turbulence can be promoted with a metallic mesh at the entrance of the input channel. A second way to increase the heat transfer between the gas and the shaft is to increase the contact area with fins adjunction. For our small geometry it was not possible to increase the surface contact between the fluid and the solid parts.

The transition between the laminar and turbulent flow occurs around $Re = 2300$ but can be much higher depending on the relative roughness of the tube and the flow at the entry channel. Below this value, the regime is laminar and turbulent for higher values. The Reynolds number is defined as:

$$Re = \frac{\rho v_m D}{\mu} \tag{5.10}$$

with the ρ the density of the fluid, v_m a characteristic velocity of the flow , D the characteristic length of the geometry and μ the viscosity of the fluid. The Reynolds numbers calculated for an Air flow of $5\,lmin^{-1}$ are given in table 5.3, the properties are taken at $300\,K$ from Incropera and Dewitt [39].

For a volume flow rate of $5\,lmin^{-1}$ of air, the mean air velocity inside the coax is $73\,ms^{-1}$ and $140\,ms^{-1}$ between the shaft and the coax. The Reynolds numbers are respectively around 2780 and 1760 for the coax channel and the outside channel along the shaft. From this calculation, the flow is laminar in both channels. Transition flow or turbulent flow is most likely to occur inside the coaxial cable first.

5.4.4 Mach number

Because air and CO_2 are used as cooling gases, it is necessary to calculate the Mach number to know if the gas can be considered as incompressible. The ratio between the mean velocity of the gas and the sound velocity give the Mach number. The calculated value is 0.4 and 0.5 for the inside channel and for the shaft channel. As described in section

2.4.1 of chapter 2 the gas can still be considered incompressible with a Mach number below 0.6 for our application.

For our fluid finite element model, the fluid was considered laminar and incompressible because the Mach number was below 0.5. For higher gas velocity, the gas needs to be considered as a compressible flow.

The use of a finite element package allows the calculation of the velocity and pressure field of an annular counter flow geometry.

5.4.5 Fluid solution

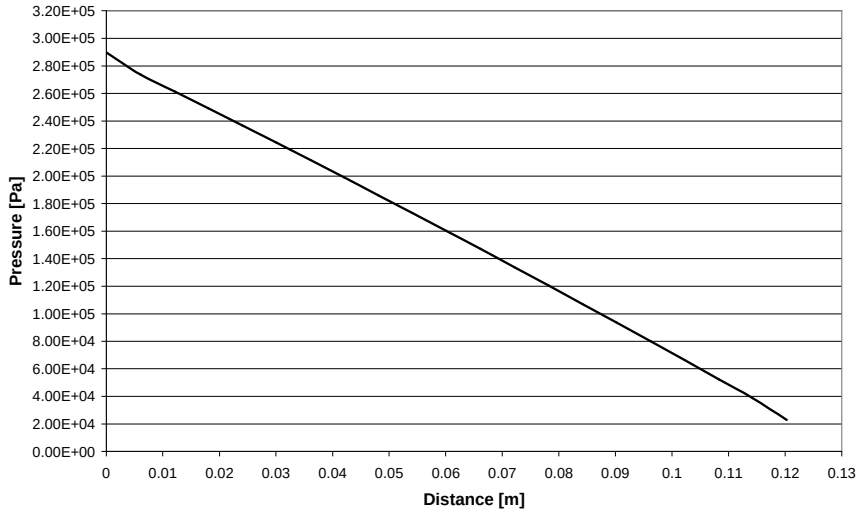

Figure 5.20: Pressure drop along inside the channel shaft/coax

For an input velocity of 118 ms^{-1}, the finite element model was run to obtain the velocity profile and pressure drop inside the tube. In figures 5.20 and 5.21 the pressure drop and velocity profiles of the two annular flows are plotted. For a flow rate of $5 lmin^{-1}$, the pressure difference between the input and output obtained with Ansys is 2.8 bar for 20 cm length. The calculated pressure drop is 2.71 bar (See Appendix A). The maximal velocity is $164 ms^{-1}$ for the input velocity of $118 ms^{-1}$ in the annular channel between the shaft and the coaxial cable. The profile of velocity is parabolic in both annular channels as shown in figure 5.21.

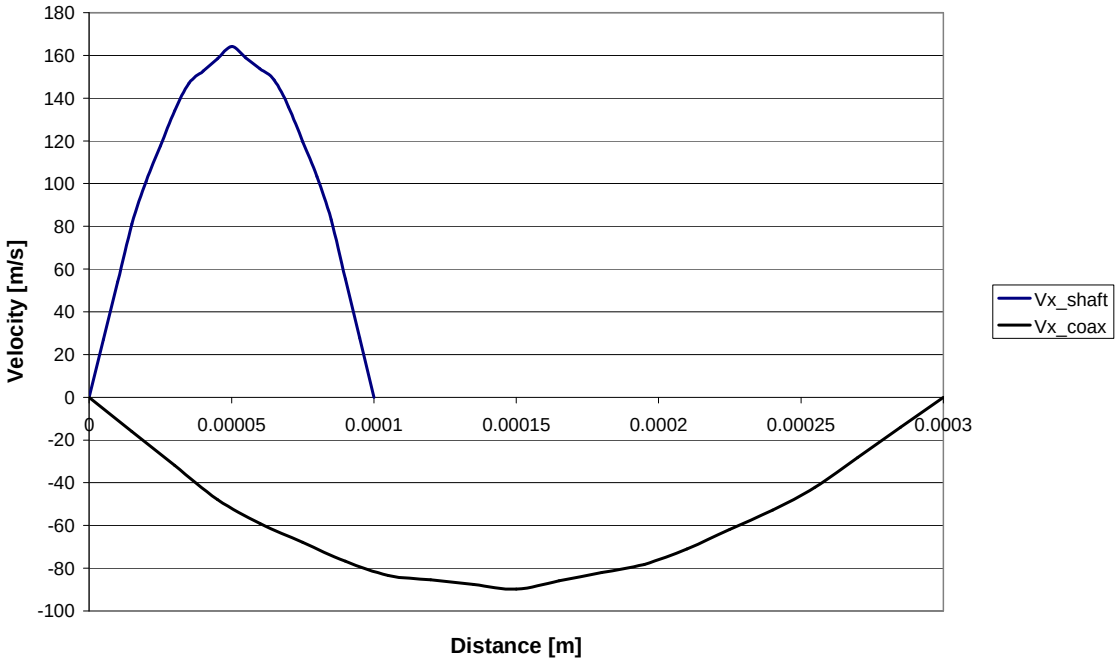

Figure 5.21: Modelled velocity profile for both channels inside the applicator. The blue curve is the velocity profile between the shaft and the coax, the black curve is the velocity profile inside the coaxial cable

5.4.6 Conclusion

From the Reynolds and Mach number calculation, the gas was considered a good approximation to a laminar incompressible flow. This assumption decreases the time required for solving the finite element model and facilitates the calculation of the fluid and thermal solution in both the fluid and solid domain of the model.

5.5 Modelled temperature with a finite element model

With a finite element package, a model was built and the temperature field was obtained in the solid and fluid part of the model by solving the energy equation in both domains.

ANSYS® multiphysics is a software package that solves various equations from different engineering domains such as Maxwell's equation for electromagnetic models; Navier Stokes equation for fluid models and heat conduction equation for thermal problems using the finite element method described in appendix C. The use of a finite element model allows the prediction of variables of interests, such as field temperature in a solid for example, over various regime and conditions. If the model described properly the real system, and also providing that a converged solution is obtained, then predicted results and measurements are usually in very good agreement. Furthermore, a computer model,

by solving an equation everywhere in the domain defined by the mesh, gives some values of interest in zones inaccessible to experimental measurements.

A 2D axisymmetric finite element model was created to evaluate the shaft temperature for different flow rates and input air temperatures.

In the prototype, the connection between the two channels consist of four holes of diameter 0.6 mm. To use the axial symmetry hypothesis, the connection between the two channels was made of a circular ring of 0.24 mm width and of 1.5 mm diameter (which is the diameter of the coax) with an equivalent area to the four holes of the built prototype. The calculation of the equivalent area of both geometries is given in equation 5.11.

$$\begin{aligned} A &= 4 \times \pi \times 0.3^2 = 1.13mm^2 \\ &= \pi \times 1.5 \times 0.24 = 1.13mm^2 \end{aligned} \tag{5.11}$$

In steady state regime the temperature will depend mainly on the flow rate and the entry temperature. For this reason, it is reasonable to assume that the geometry of the junction does not affect significantly the temperature profile along the shaft.

The advantages of using a 2D axisymmetric model are faster time calculation and higher accurate solution.

In the fluid domain, the velocity and pressure field are obtained by solving the incompressible laminar fluid equation. Then, the equation of heat conduction is solved in both the solid and fluid part of the model.

The effect of the aluminium tape used to fix the thermocouples on the shaft for the measurements was not modelled. To take into account of this effect, the modelled thermocouple temperatures were expressed as a linear relationship between the modelled temperature of the shaft and the surrounding temperature of the polystyrene.

$$T_{modelledthermocouple} = \alpha T_{modelled} + (1 - \alpha) T_{room} \tag{5.12}$$

with $T_{modelledthermocouple}$ the modelled temperature at the thermocouple junction and $T_{modelled}$ the modelled temperature of the shaft without any thermocouple and aluminium tape. T_{room} is the temperature at the interface aluminium tape and polystyrene. $\alpha = 0.8$ is determined from the analytical model of a cylindrical geometry described in Appendix F.

The model of the gas cooling circuit of the applicator shown in figure 5.22 and 5.23 consist of a counter flow double annular channel.

In figure 5.22, the green area is the surrounding Polystyrene insulation, the red area is the shaft, the violet area is the coaxial cable, centre conductor and copper ferrule, the pink area is the PTFE surrounding the centre conductor and the PTFE inside the copper ferrule. The blue area is the ceramic tip and ceramic cylinder and the magenta area is the

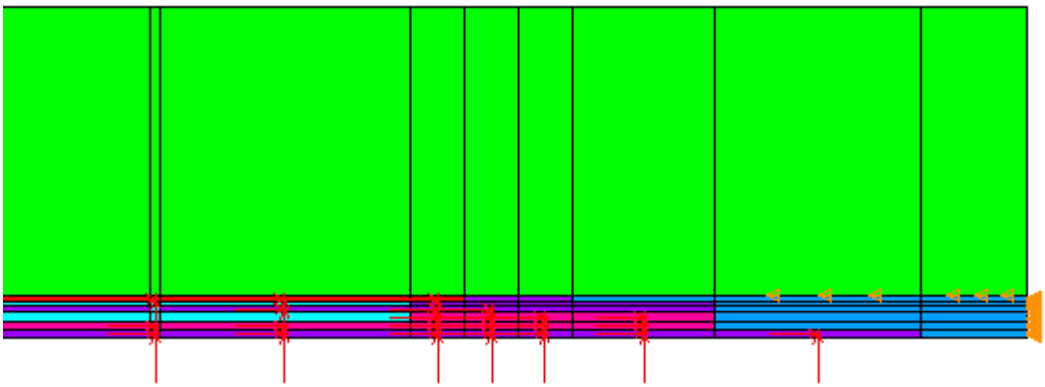

Figure 5.22: 2D axisymmetric model with boundaries conditions

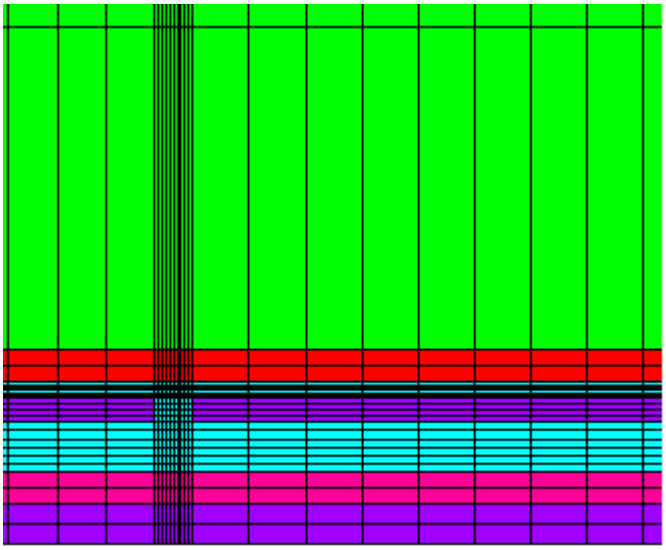

Figure 5.23: Mesh of the 2d axisymmetric model near the hole junction

fluid domain. Figure 5.23 shows the mesh of the fluid and solid domain of the gas circuit model.

5.5.1 Material properties

The properties of solid material used for the model are given in table 5.4 and table 5.5 for air properties at different temperatures.

Copper has a high thermal conductivity, 30 times the thermal conductivity of steel. This implies that the heat flux from the heat source toward the handle will be more important in the coaxial cable compared to the heat flux in the steel shaft.

Properties at 27 °C(77 °C)	Steel	Copper	Ceramic	PTFE	Polystyrene
Conductivity k $[Wm^{-1}K^{-1}]$	13.4 (15.2)	401 (393)	2	0.25	0.04
Density ρ $[kg\,m^{-3}]$	8238	8933	6050	2200	56
Specific heat C $[J\,kg^{-1}K^{-1}]$	468	385	400	1000	1210

Table 5.4: Thermal properties of solid material used for the model [40]

Properties of air[°C]	-23	27	77	127	177	227
Conductivity k $[Wm^{-1}K^{-1}]$	22E-3	26.3E-3	30E-3	33.8E-3	37.3E-3	40.7E-3
Density ρ $[kg\,m^{-3}]$	1.3947	1.1614	0.995	0.8711	0.7740	0.6964
Specific heat C $[J\,kg^{-1}K^{-1}]$	1006	1007	1009	1014	1021	1030
Viscosity $\mu[Ns\,m^{-2}]$	159.6E-7	184.6E-7	208.3E-7	230.1E-7	250.7E-7	270.1E-7

Table 5.5: Thermal properties of air at different temperatures [39]

5.5.2 Boundary conditions

Red arrows shown in figure 5.22 indicate the velocity boundary condition. For all the non fluid parts, velocity was set to 0 on the walls of the solid domain. Yellow arrows indicate the constant temperature set to these lines. At the output circuit of the fluid, a reference pressure of zero bar was assigned. By default Ansys software assigned adiabatic boundary condition on the outside lines of the geometry.

Velocities on the wall of the two channels are zero. The input velocity is $140\,ms^{-1}$ at room temperature, which corresponds to a flow rate of $5\,lmin^{-1}$. The input velocity is $118\,ms^{-1}$ for an input temperature of $-20\,°C$ for a standard flow rate of $5\,lmin^{-1}$. At the output of the channel, a reference pressure is set to 0 bar.

For the steady state regime, a temperature at 100 °C is specified at the end of the ceramic to simulate the ceramic tip immersed in the oil at 100 °C and the input temperature is specified at the entrance of the channel, for example room temperature or −20 °C. By default, the thermal boundary condition on the shaft is a zero heat flux known as the adiabatic condition.

5.5.3 Modelled temperatures in steady state regime with a 2D axisymmetric model

Once the velocity field was obtained, the energy equation was solved for both the fluid and solid part with the 2D axisymmetric model for the steady state regime.

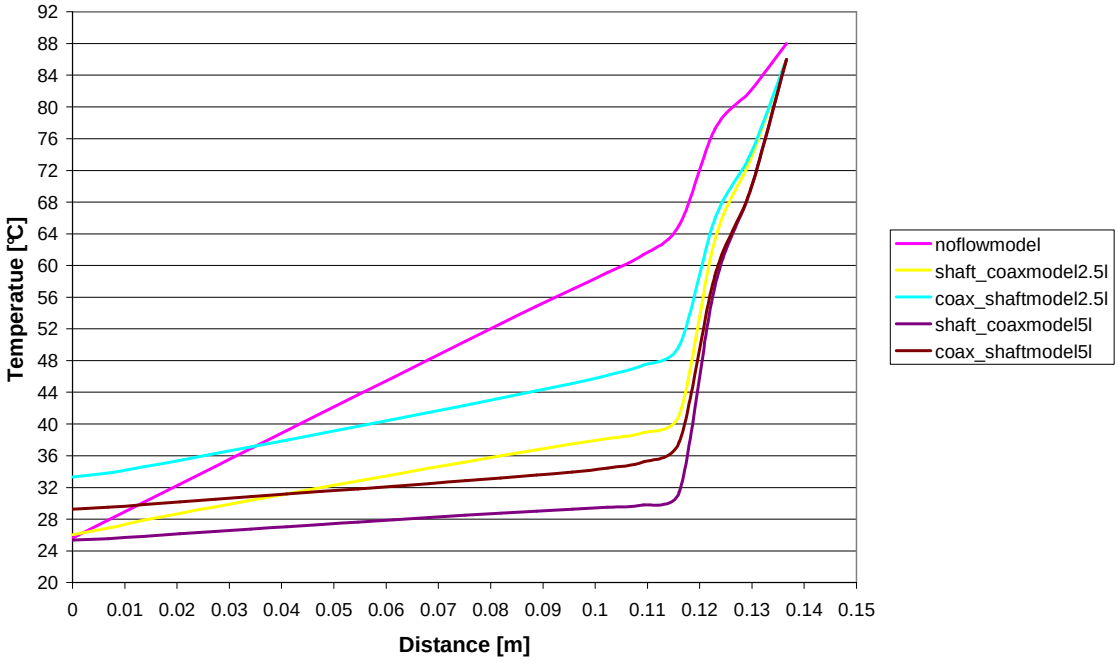

Figure 5.24: Modelled temperature 2.5 $lmin^{-1}$ and 5 $lmin^{-1}$ and two directions, input temperature: 23 °C

5.5.3.1 Initial conditions

The heat source from the oil bath was simulated by assigning a temperature on the line of the ceramic of 100 °C.

Temperatures were plotted against distance along the shaft to compare the cooling effect of the air flow for two sets of simulations. The first set of simulations was performed at an initial gas temperature of 23 °C for two different flow rate and flow directions.

The second set of simulations is composed of two different flow direction with a flow rate of 5 $lmin^{-1}$ and an initial gas temperature of −20 °C.

The boundary condition applied on the polystyrene line of the model was a zero heat flux known as adiabatic condition.

5.5.3.2 Results for air entry at 23 °C

In figure 5.24 modelled temperature along the shaft obtained with the model for an input air at room temperature is plotted.

Temperature profile along the shaft is indicated by the pink curve in figure 5.24 for the first simulation with no air flow flowing inside the circuit. The entry temperature was set at 22 °C. The temperature of the shaft is proportional with the distance from the heat source, as expected, the temperature gradient is constant in the shaft.

The reason is that heat transfer occurs mainly along the direction of the steel shaft.

Regime	steady	steady	steady	steady	steady
Flow rate [$lmin^{-1}$]	0	2.5	2.5	5	5
Initial temperature [∘C]	-	24	24	22	23
Direction of flow	-	shaft/coax	coax/shaft	shaft/coax	coax/shaft
Length below 40 °C [cm]	4.4	10	4.5	12	11.6

Table 5.6: Effect of two different flow rate and two direction of flow on the shaft temperature

Two runs were performed with air temperature entry at 24 °C with a flow rate of 2.5 $lmin^{-1}$ in the shaft/coax and coax/shaft directions as shown by the yellow and blue curve of figure 5.24. For the direction of flow shaft/coax, temperature of the shaft remains below 40 °C over a distance of 10 cm (yellow curve). The length of the shaft below 40 °C is only 5 cm for the same flow rate with the direction coax/shaft (blue curve). With this configuration the heat is transported nearer the entry of the shaft.

With air entry temperature at room temperature, the configuration shaft/coax is more effective than the configuration coax/shaft to maintain a shaft temperature below 40 °C over a long distance. The reason is that with the coax/shaft configuration heat is transported from the heat source to the lower temperature area near the exit (Compared brown with violet curve, and blue with yellow curve of figure 5.24).

For higher flow rate 5 $lmin^{-1}$ the two runs performed with air temperature entry at 22 °C an 23 °C in both directions show that the cooling effect is more important than the previous case, the temperature of the shaft remains below 40 °C over a distance of 11.6 cm. (See light violet and brown curve in figure 5.24).

A flow rate of 5 $lmin^{-1}$ gives a lower temperature along the shaft than a flow rate of 2.5 $lmin^{-1}$ for both directions shaft/coax and coax/shaft. The slope of curves with a 5 $lmin^{-1}$ flow rate are smaller than curves with a flow rate of 2.5 $lmin^{-1}$. (Comparing the violet with the yellow curve and the brown with the blue of figure 5.24).

After 11 cm for locations closer to the heat source, there is a quick increase of temperature. The slope of the temperature curves greatly increased near the heat source. This is due to the fact that the region is purely solid material and has no air flow to cool this solid region directly. The results of the different simulations are summarized in table 5.6.

5.5.3.3 Results for air at −20 °C

In figure 5.25, modelled temperatures are plotted for an air input temperature of −20 °C.

Runs at a flow rate of 5 $lmin^{-1}$ with an input initial temperature of −20 °C were performed for both directions as shown in figure 5.25.

As in the case at room temperature, until 11 cm, temperatures are nearly proportional

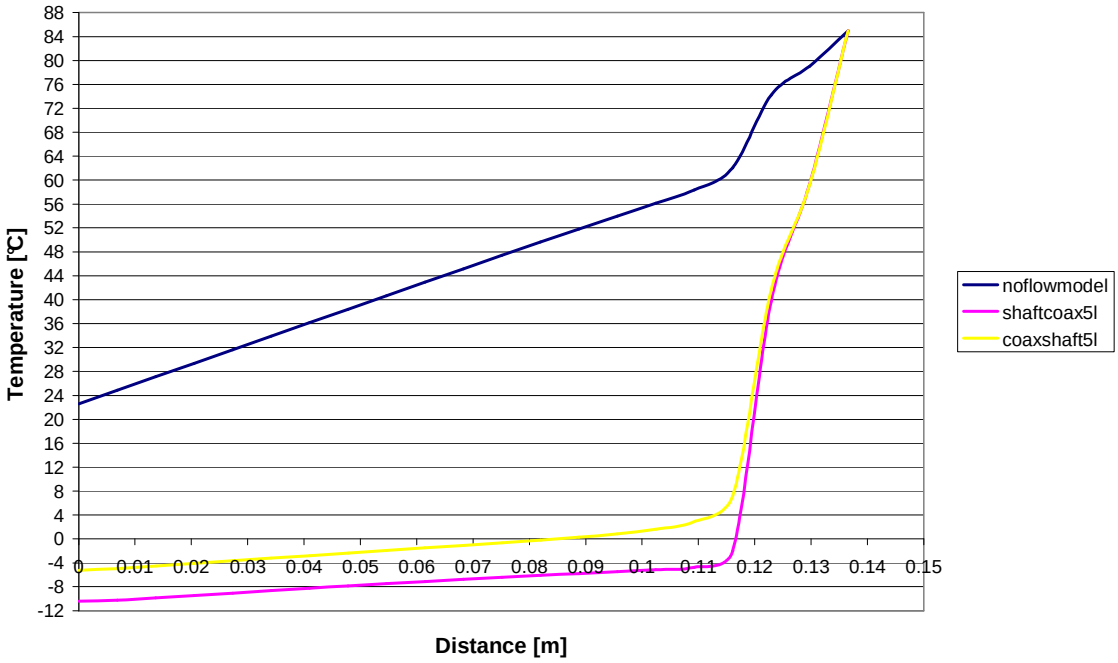

Figure 5.25: Modelled temperature with an air flow of 5 $lmin^{-1}$ and two directions, input temperature: $-20\,°C$

to the distance and the large increase of temperature occurs in the solid part of the device near the heat source.

The shaft temperature is below $-4\,°C$ over a length of 11.5 cm for the shaft/coax configuration and below $0\,°C$ over a length of 8 cm for the coax/shaft configuration.

At low input temperature as shown in figure 5.25, the configuration with the flow flowing in the direction coax/shaft is more interesting because it offers a lower temperature gradient along the shaft and the temperature of the shaft at the entrance of the fluid $z = 0$ is higher than the configuration shaft/coax. This configuration avoids potential cold burns for the tissue surrounding the shaft during a microwave ablation.

5.5.4 Modelled temperatures in transient regime with a 3D model

The prototype has four holes located at the end of the copper coaxial cable. When the end is plunged in hot oil, heat conduction occurs through the coax and shaft. The effect of the copper junction around the holes cannot be reduced to a annular air space for the transient regime. For this reason, a 3D model was built with the thermal properties and boundaries conditions identical to the 2D model.

The two annular gas channels of the model are shown in figure 5.26. Evolution of temperature along the shaft was investigated by performing a transient thermal analysis. A transient model is less sensitive to boundary conditions at the beginning of the run, because

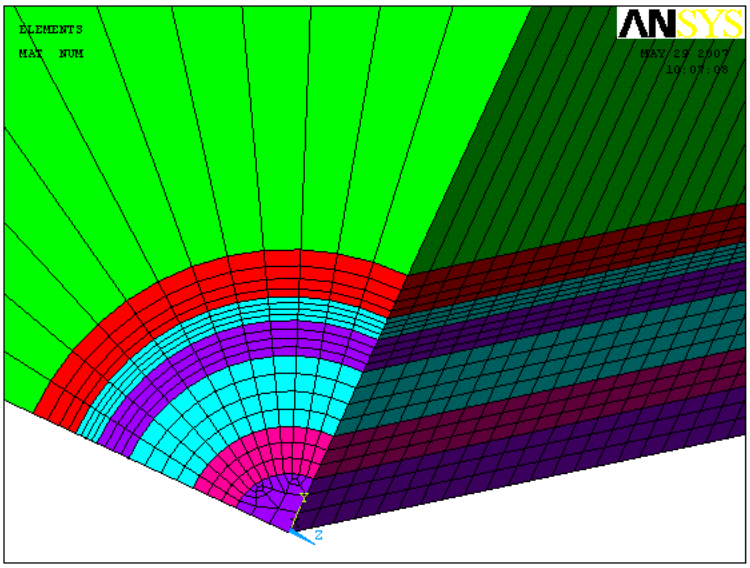

Figure 5.26: 3D model of the gas circuit with the mesh

the thermal equilibrium is not reached and the cause of the variation of temperature depends more of the heat source term than the boundaries conditions located further to the heat source.

The transient analysis concerns only the thermal part, because the fluid was set at a constant flow rate, so the fluid solution was a steady state solution.

To model the effect of plunging the ceramic tip of the applicator in the oil bath in a short time, the temperature recorded during measurement tests by the first thermocouple T1 located on the ceramic was applied on the ceramic line of the model.

Then, temperature as a function of time was obtained for the five thermocouples for the transient case with no flow and for an air flow of $5\,lmin^{-1}$ at room temperature.

5.5.4.1 Results no air flow

In figure 5.27 the blue curve is the temperature recorded by thermocouple T1 during an experimental measurement and is assigned to the ceramic area of the model. It is the temperature evolution of the ceramic tip when the applicator tip is immerged in the oil bath. The next four curves show the modelled temperature evolution at four location along the shaft specified in figure 5.8 of section 5.3. The initial temperature of the solid and air domain was set to 32 °C.

The introduction of the applicator tip in the oil bath takes less than a second. In figure 5.27, large increase of temperature occurs near the ceramic tip, the increase of temperature is less as the distance along the shaft increases. Table 5.7 shows that the amplitude of increased temperature decreased with the distance from the tip. There is a time delay

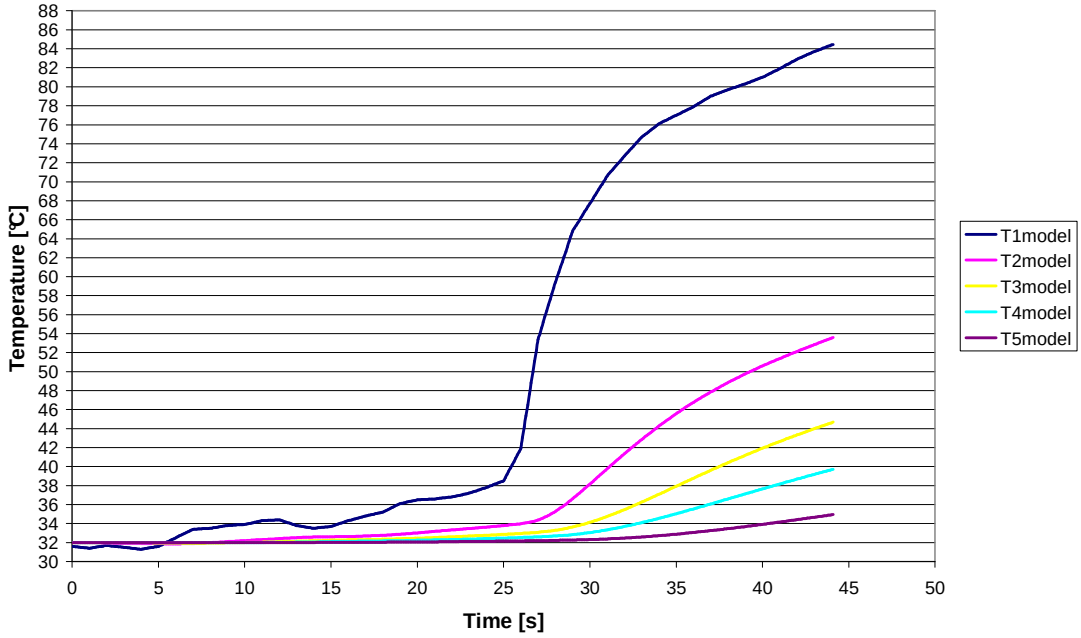

Figure 5.27: Modelled temperature for the transient run, no flow

Time [s]	t = 25	t = 30	t = 35
T1 (measured)[∘C]	38.5	67.7	77
T2 [°C]	33.8	38.2	45.6
T3 [°C]	32.9	34.1	37.9
T4 [°C]	32.5	33.1	35
T5 [°C]	32.1	32.3	32.8

Table 5.7: Evolution of modelled temperature for different locations, no air flow

during the heat conduction along the shaft. For example temperature of T4 and T5 change only after 5 seconds whereas temperature of T2 and T3 change significantly in the first 5 seconds.

5.5.4.2 Results air flow $5\,lmin^{-1}$

In order to assess the effect of air cooling, fluid and thermal equations were solved with an air flow of $5\,lmin^{-1}$, with the same temperature loads and boundaries as for the model with no flow. The initial temperature of the solid domain was set to 25.7 °C, the air temperature entry was set to 24 °C to match the inital temperature of the experimental conditions.

In figures 5.28 the temperature against time is plotted for the first five thermocouples. For the run with a flow rate of $5\,lmin^{-1}$ in the direction shaft/coax temperatures of

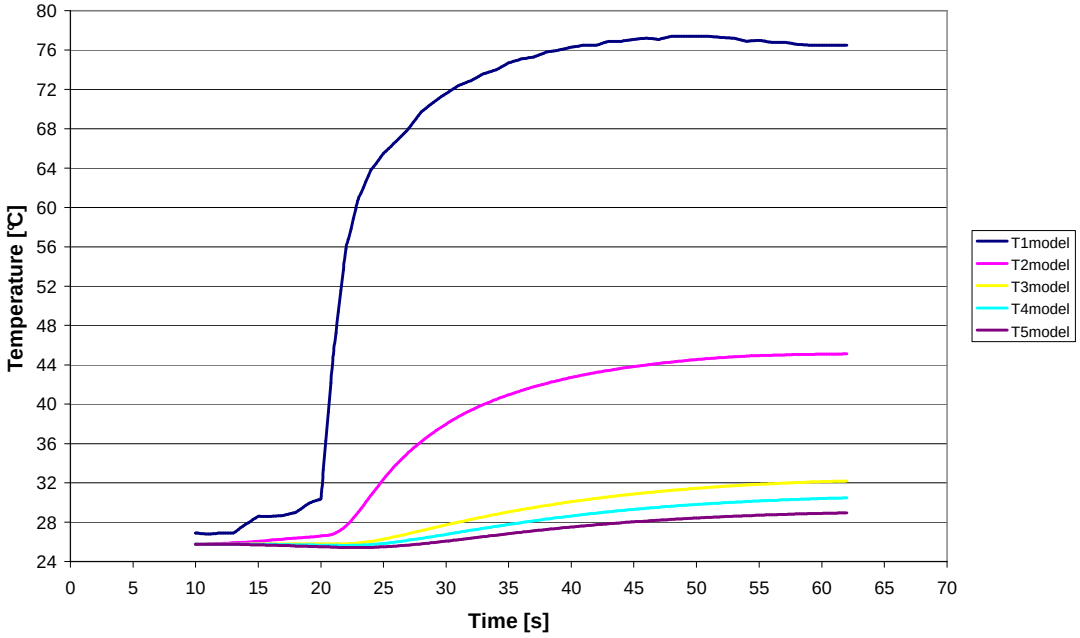

Figure 5.28: Modelled temperature for the transient run, flow rate $5\,lmin^{-1}$, direction shaft/coax

Time [s]	t = 20	t = 25	t = 30
T1 (measured)[∘C]	30.4	65.5	71.6
T2 [°C]	26.6	32.4	37.9
T3 [°C]	25.8	26.3	27.7
T4 [°C]	25.6	25.8	26.7
T5 [°C]	25.5	25.5	26

Table 5.8: Evolution of modelled temperature with air flow $5\,lmin^{-1}$

thermocouple T3 to T5 are maintained below 34 °C. Heat energy is taken by air flowing inside the applicator, the amplitude of the slope of the curves of temperature are smaller than the case with no air flow.

Shaft temperatures T1, T2 and T3 increase less than the previous case because of the cooling action of the air flow. Temperature T4 and T5 remains quasi unchanged in the first 10 seconds as shown in table 5.8.

5.5.5 Conclusion

Fluid and heat conduction were solved in transient regime with a 3D finite element model. With an air flow of $5\,lmin^{-1}$ at room temperature, the shaft is significantly cooled. By comparing the model with an air flow and no flow 10 seconds after the thermal impulse, temperature of thermocouple T2 decrease by 8 °C (from 45.6 °C to 37.9 °C) and by 10 °C

for T3. (from 37.9 °C to 27.7 °C for T3) .

5.6 Comparison of measured and predicted temperature

In this section, the measured and modelled temperature of the applicator shaft described in sections 5.3 and 5.5 are compared in order to check the validity of the model. The temperature measurement accuracy was estimated as $\pm 1.5\,°C$, the spatial accuracy was estimated as $\pm 2mm$ for the location of thermocouples, the temporal accuracy was $\pm 1s$ for the transient measurements.

Modelled temperatures appeared as a black line with no markers whereas the measured results are shown with markers with an error measurement bar in the x and y direction for each thermocouple.

5.6.1 Steady regime

5.6.1.1 Results

Three comparisons were performed in steady state regime. The measured and modelled are plotted together in a temperature - distance graph for the case with no air flow and with a $2.5\,lmin^{-1}$ air flow at room temperature in both direction shaft/coax and coax/shaft.

As shown if figure 5.29, the modelled temperature predict the measurement for the first three thermocouples T7, T6 and T5. The temperature gradient is also well predicted by the model, the slope of the black curve is parallel to a line passing through thermocouple T7, T6 and T5 of figure 5.29.

The difference between modelled and measured temperature increased for thermocouple T4, T3 and T2 near the heat source with a difference of approximatly 6 °C for T4, 8 °C for T3 and 4 °C for T2.

The second comparison shown in figure 5.30 is for the case with a $2.5\,lmin^{-1}$ air flow at 22 °C in the shaft/coax direction. For this case, the temperature prediction of the shaft is closed to the measured temperature. The temperature gradient given by the slope of the line is well predicted for first five thermocouples. Except for thermocouple T2, the modelled temperature is very closed to the measured temperature.

The third comparison shown in figure 5.31 is for the case with a $2.5\,lmin^{-1}$ air flow in the coax/shaft direction. The predicted temperature is still in good agreement with the measured temperature.

5.6.1.2 Comments

In steady state regime, modelled and measured temperature along the shaft are in good agreement. The difference between the predicted and measured temperature is more

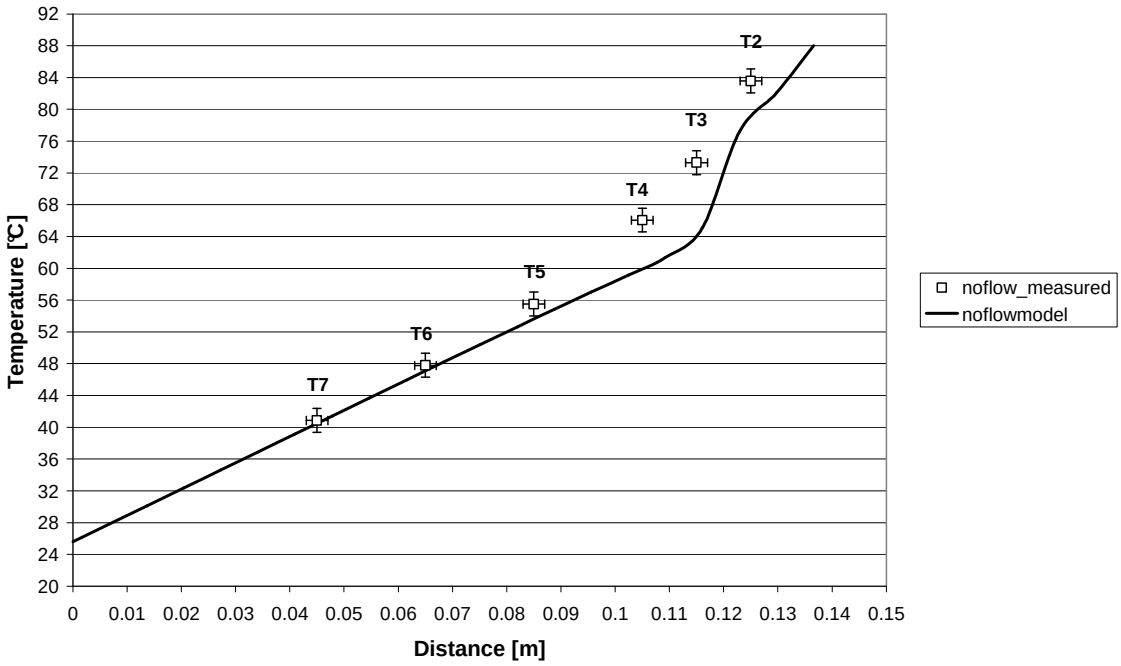

Figure 5.29: Measured and modelled temperature with no air flow

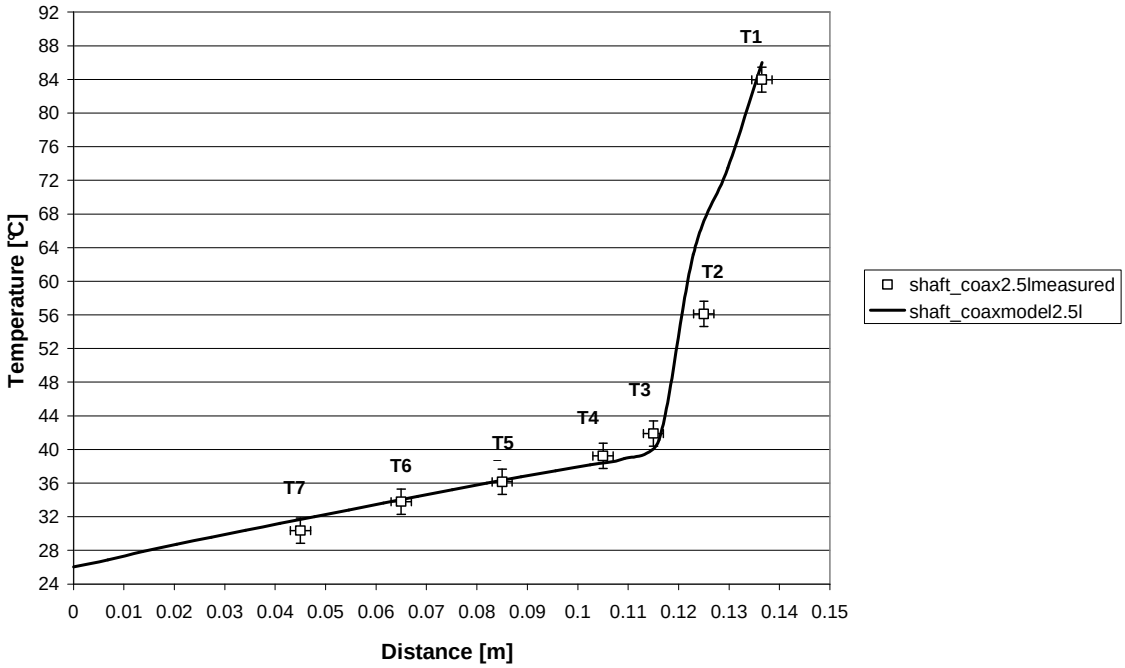

Figure 5.30: Measured and modelled temperature with $2.5\,lmin^{-1}$ air flow in the shaft/coax direction

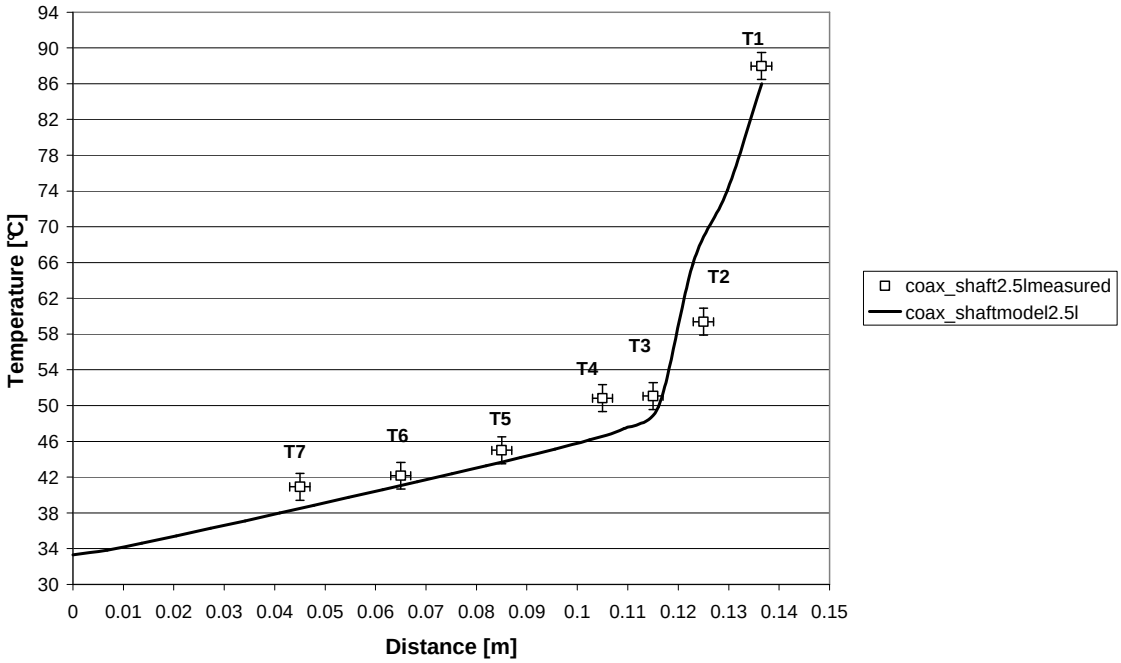

Figure 5.31: Measured and modelled temperature with $2.5\,lmin^{-1}$ air flow in the coax/shaft direction

important for the thermocouple near the heat source than for those located at the channel entrance.

The difference between the predicted and measured temperature can be explained by the boundary condition used for the model. In the model, the temperature of 100 °C was applied on the edge of the area representing the ceramic immersed in oil at 100 °C. In reality, there exists a temperature gradient from the heat source to the shaft.

The effect of the junction thermocouple on the shaft with aluminium tape was taken into account with the relation 5.12 of section 5.5.

Factors that can be the cause of differences between the modelled and measured temperature are:
- the effect of the junction thermocouple on the shaft with aluminium tape was taken into account with a linear relationship between the modelled temperature without any thermocouple on the shaft and the room temperature (see equation 5.12 of section 5.5)
- difference between the effect of the environment and the modelled applied boundary condition
- difference between the model geometry and the prototype geometry of the applicator
- location of the thermocouple along the shaft
- initial temperatures

In the next section, transient temperature measurements are compared with the 3D

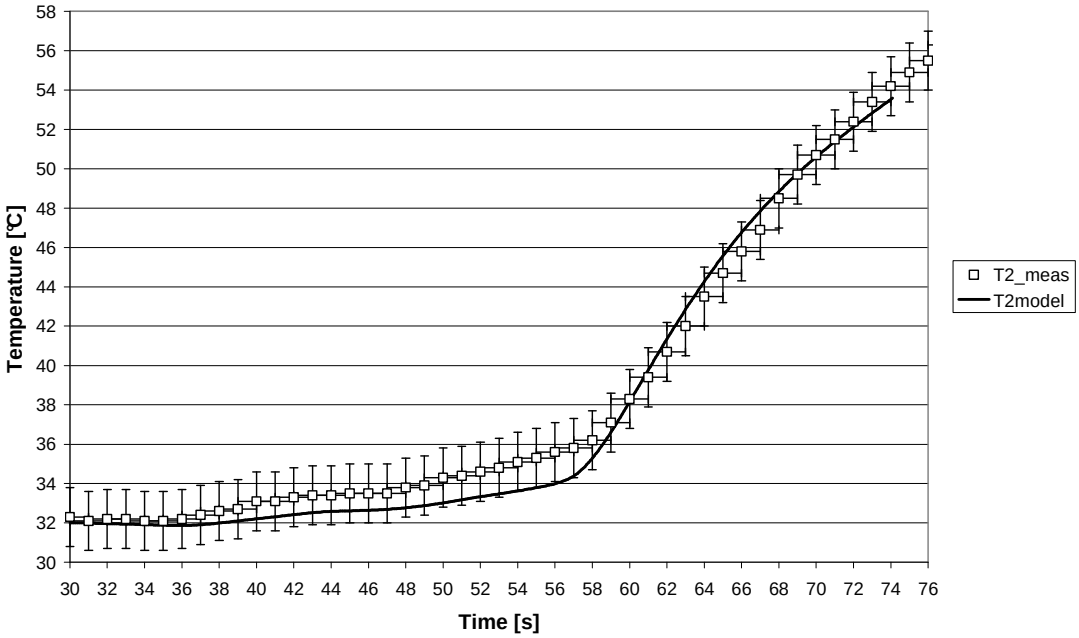

Figure 5.32: Measured and modelled temperature in transient regime for T2 with no air flow

model.

5.6.2 Transient regime

A comparison of transient measured temperature and transient modelled temperature described respectively in the previous section 5.3 and 5.5 is performed in order to check the validity of the model. The entrance for the gas was in the annular channel shaft/coax.

5.6.2.1 Results with no air flow

In figure 5.32, the measured and modelled temperature at the thermocouple T2 location is plotted. The modelled temperature follows the temperature evolution at this location and at the time $t = 58\,s$ both modelled and measured temperature start to increase.

In figure 5.33, modelled and measured temperature at the thermocouple T3 location are plotted. The modelled temperature predicted the temperature evolution of the shaft. At the time $t = 59\,s$ both temperatures start to increase quickly.

In figure 5.34, modelled and measured temperature at the thermocouple T4 location are plotted. As for the two previous cases, the model predicts the shaft temperature evolution at this location with a quick increase of temperature amplitude at $t = 60\,s$.

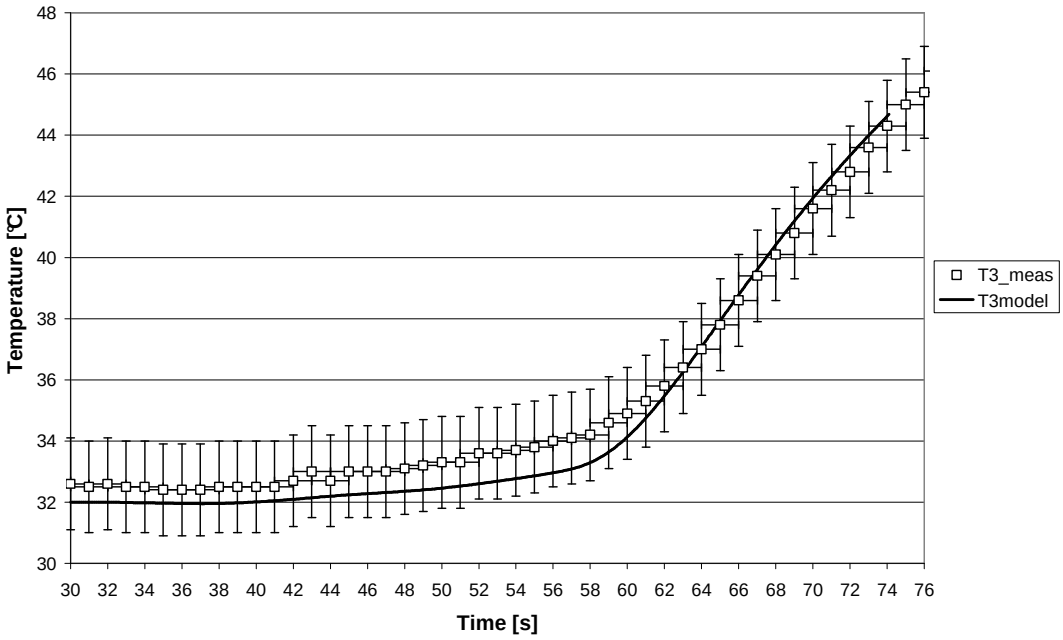

Figure 5.33: Measured and modelled temperature in transient regime for T3 with no air flow

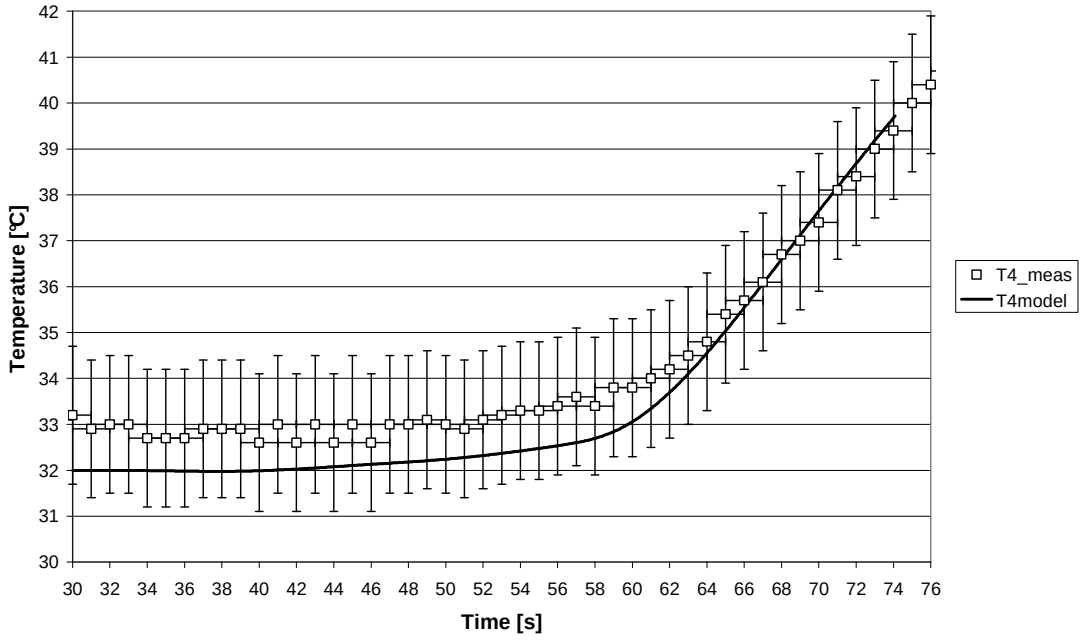

Figure 5.34: Measured and modelled temperature in transient regime for T4 with no air flow

5.6.2.2 Results with $5\,lmin^{-1}$ air flow

In figure 5.35 modelled temperature at the location of thermocouple T2 follows the measured temperature evolution. The model slightly over predicted the measured temperature. 20 seconds after the thermal impulse, the modelled and measured temperature are respectively 45 °C and 43 °C.

In figure 5.36 modelled temperature at the location of thermocouple T3 follow closely the measured temperature evolution. Change of temperature magnitude before and after the thermal impulse is smaller at this location because distance from the heat source is greater than for the thermocouple T2. (T2 and T3 are located respectively at 1.15 cm and 2.15 cm from the heat source)

In figure 5.37 modelled temperature at the location of thermocouple T4 follows closely the measured temperature. Thermocouple T4 is located at 3.15 cm from the heat source and the magnitude of temperature increase after the thermal impulse is 4 °C.

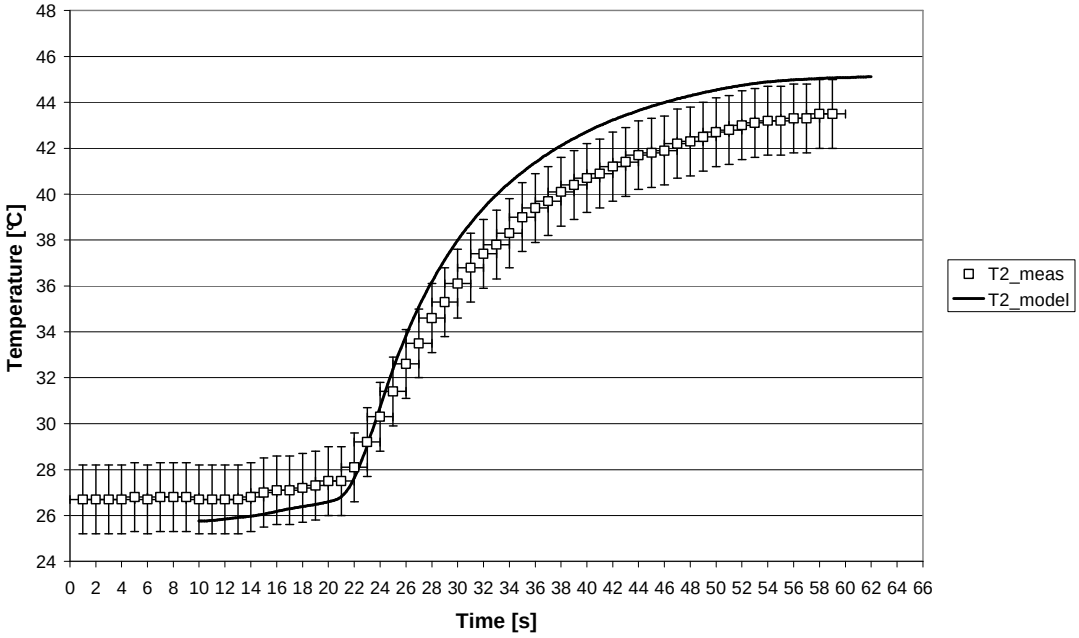

Figure 5.35: Measured and modelled temperature for T2, air flow $5\,lmin^{-1}$

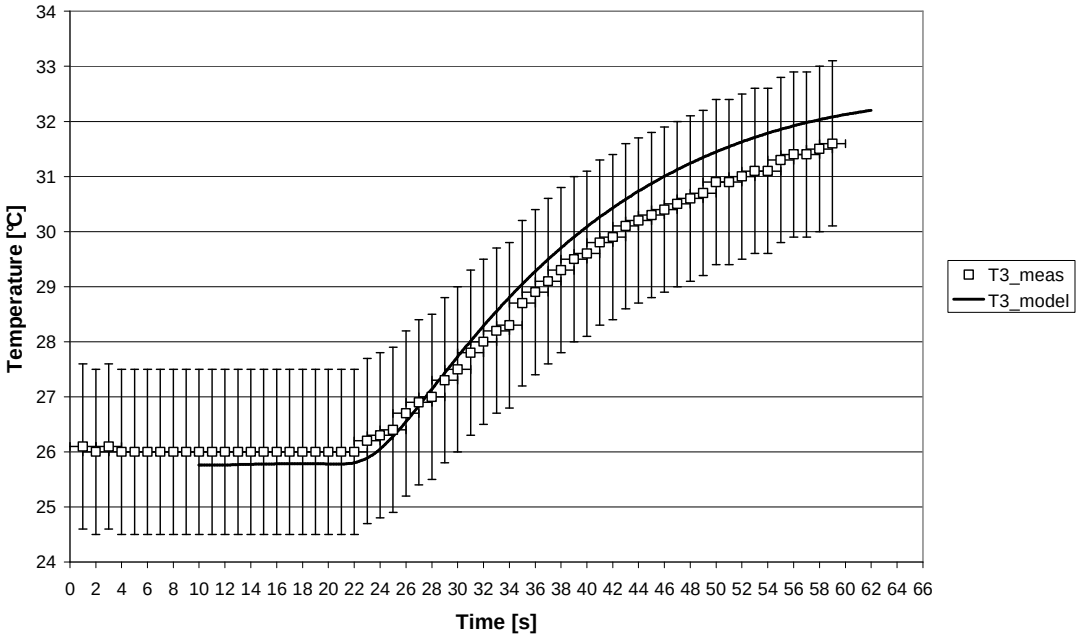

Figure 5.36: Measured and modelled temperature for T3, air flow $5\,lmin^{-1}$

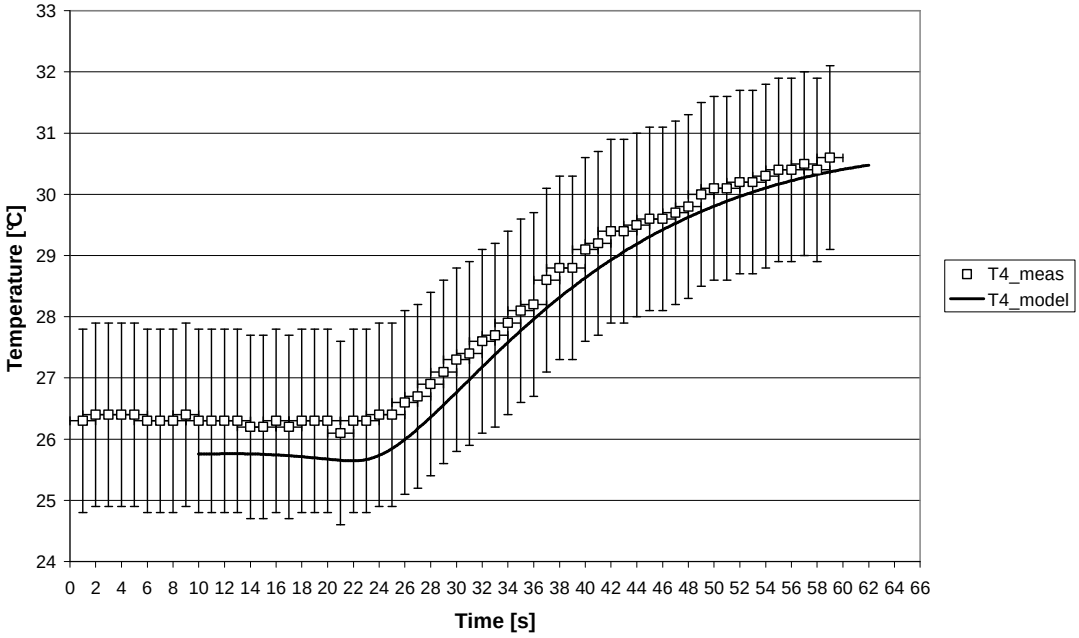

Figure 5.37: Measured and modelled temperature for T4, air flow $5\,lmin^{-1}$

5.6.2.3 Comments

Overall, the modelled temperature for the case without air flow and the case with an air flow of $5\,lmin^{-1}$ is in good agreement with the measured temperature.

5.6.3 Conclusion

The gas thermal model of the cooling circuit of the double annular channel predicts the temperature measurements. The difference between the test prototype geometry and the model geometry can explain the small discrepancy between modelled and measured temperatures.

For the thermal steady state case, temperature differences can be explained by the difference between the real and the modelled boundary condition applied to the model. (adiabatic along the shaft and imposed temperature on the ceramic). The difference between modelled and measured temperature increase as the distance from the heat source decrease.

For the transient case, temperature evolution is less sensitive to the boundary condition and the modelled temperature predict very well the measured temperature.

5.7 Summary

The temperature measurements and the finite element model have demonstrated that the air flow significantly cools the shaft of the applicator. Despite some small difference for temperature near the heat source for the steady thermal case, the 2D model predict well the temperature behaviour along the shaft of the applicator.

For the transient regime the 3D model predicts well the temperature behaviour along the shaft of the applicator.

The electromagnetic and thermal studies have shown that it is possible to use an air filled coaxial cable for a microwave applicator. The main interest of using gas as a cooling fluid is that it cools the applicator internally. It allows a simpler and compact design for the gas cooling circuit by using the space between the inner and outer conductor of the coaxial line.

The gas cooling circuit has been implemented on the 2.4 mm and 5 mm applicators, they are presented in the next two chapters.

Chapter 6

5 mm gas cooled applicator

6.1 Introduction

Following the development of the open loop 5 mm applicator for laparoscopic applications described in chapter 3, a closed cooling system was seen as the solution to avoid any liquid water being deposited in the heating zone. This would decrease the potential risk of steam formation leading to unexpected ablation owing to fluid movements inside the complex structure of the liver tissue.

When the concept of using gas inside the applicator in the design of a closed loop circuit was considered, it was felt that the best method was to implement an air coaxial cable within the current open loop 5 mm applicator.

In operation, the closed loop 5 mm applicator will be used with the laparoscopic procedure in an identical way to the 5 mm applicator open loop because the only difference between these two applicators is the presence, or not, of the released water in the tissue. In this section, the construction and working of the 5 mm gas cooled applicator is presented in order to show that a gas cooling circuit can be used for different microwave applicators.

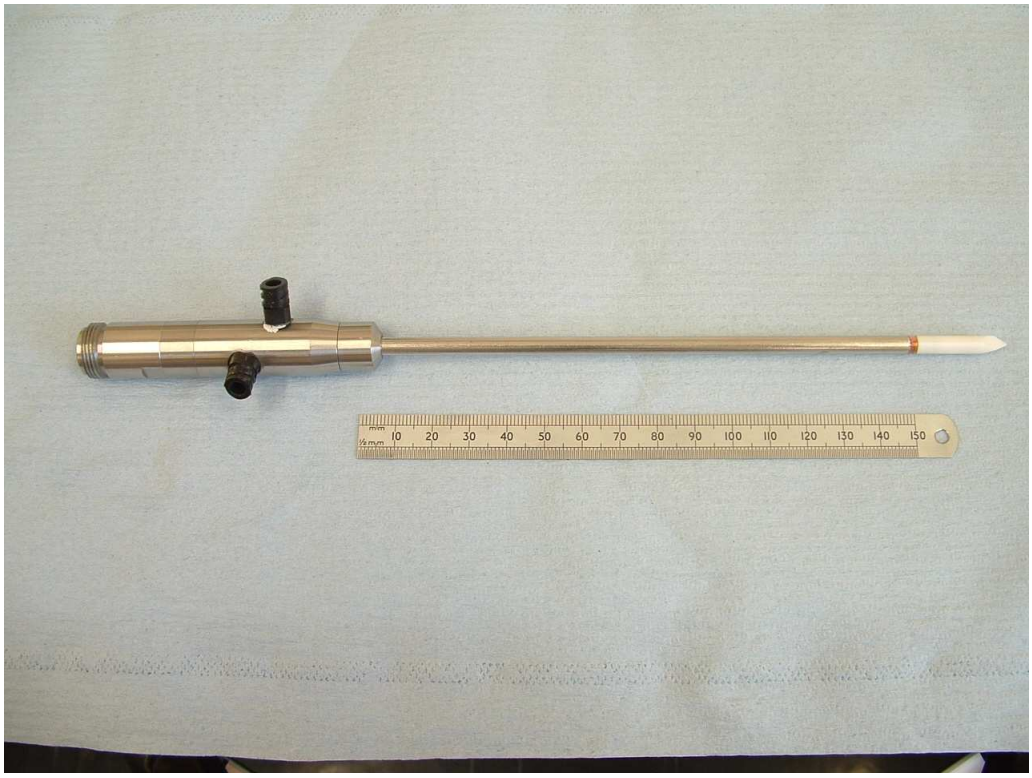

Figure 6.1: 5mm percutaneous gas cooled applicator

6.2 Specifications

The operational specifications of this microwave closed loop applicator are the same as the 5 mm open loop of chapter 3. The applicator has to perform large ablations in a short time with delivering a power up to 200 watts. The mechanical requirements, in order to penetrate the tissue easily, are a sharp radiating tip, a robust and rigid stainless

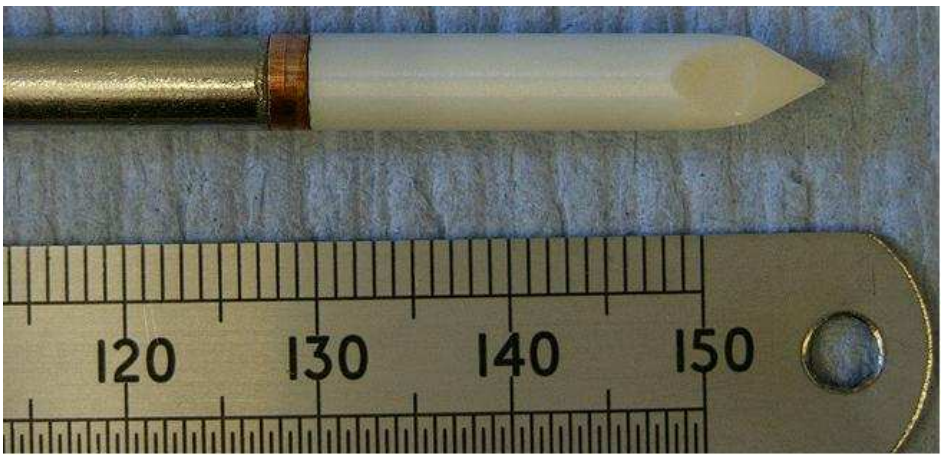

Figure 6.2: Ceramic trocar tip of the 5 mm applicator

steel shaft coated with a polymer. The gas cooled applicator is shown in figure 6.1. The trocar ceramic tip geometry shown in figure 6.2 facilitates the insertion by cutting the tissue during the insertion.

6.3 Applicator design

The difference between the open loop and the closed loop applicator is the use of an air filled coaxial. It is shown in chapter 5 that the small difference of characteristic impedance between a PTFE filled coaxial cable and air filled coaxial cable has little effect on the reflected power. For this reason and for machining reasons, the radiating section of the 5 mm closed loop applicator is identical to the 5 mm open loop applicator presented in chapter 3.

6.3.1 Principle of operation

The antenna geometry is shown in the figure 6.3. PTFE seals are used at the end of the coaxial cable to close the gas circuit. Microwaves travel along the coaxial cable and then are radiated from the radiating tip into the tissue.

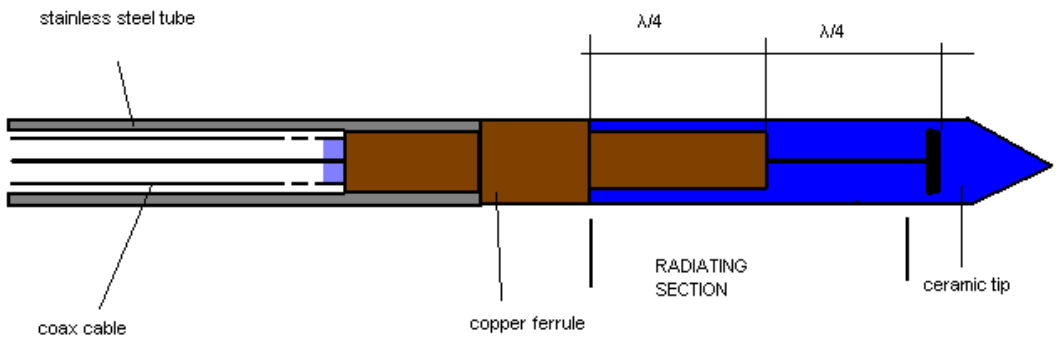

Figure 6.3: Radiating section of the 5 mm closed loop applicator with the air filled coaxial cable

6.3.2 3.6 mm air filled coaxial cable

Figure 6.4: Conductor with PTFE spacers

Figure 6.5: Coaxial tube with holes

The copper coaxial cable is 3.58 mm outside diameter and 2.98 mm inside diameter with four holes of 1 mm diameter at both ends. The space between the centre conductor and outer conductor was sufficient to allow the use of small PTFE spacers (see figure 6.4) placed at four centimetre intervals to maintain the centre conductor in the centre and to create an annular space for the gas flow as shown in figure 6.5 and 6.7.

A cross section of the coaxial cable is shown in the figure 6.7 showing a rectangular PTFE spacer and the two air channels.

6.3.3 Gas circuit

The goal of the cooling system is to maintain a shaft temperature below 42 °C as prescribed by the safety regulatory authority in order to prevent local burns of normal tissue along the track of the applicator. At the same time, the gas cools the applicator components allowing its safe working at higher power.

In figure 6.6, the internal gas circuit of the applicator is shown with the red line indicating the path of the gas flow. The cold air flows from the high pressure chamber, then through the coaxial cable, exits through the coax holes, flows through the annular space between the shaft and the coax and finally exits to the low pressure chamber. The path of a gas particle is indicated by the red line and the number from 1 to 5 in figure 6.6. The inner channel inside the coaxial cable and the outer annular channel are shown in figure 6.7.

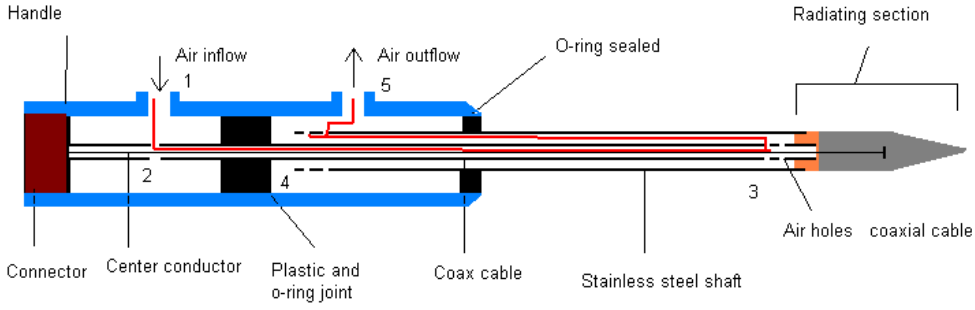

Figure 6.6: Schematic of the internal gas circuit of the applicator, the red line and the numbers 1 to 5 indicate the gas path

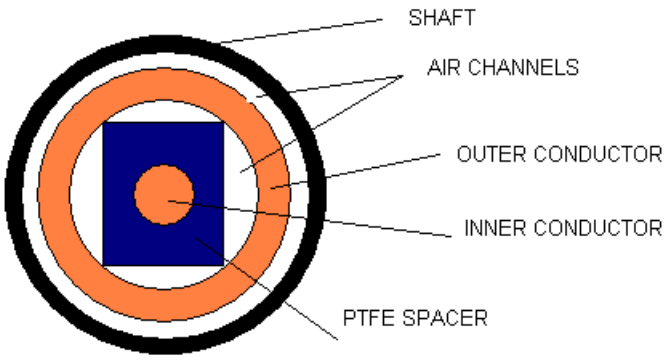

Figure 6.7: Cross section of the air filled coaxial cable at a spacer location

Figure 6.8: Handle of the 5 mm gas applicator

During the liver ablation tests, an air flow from 6 to 10 $lmin^{-1}$ was used giving a pressure up to 2.5 bars in the high pressure chamber.

6.3.4 5 mm applicator handle

The handle is basically a stainless tube, which is the part of the applicator manipulated by the surgeon. Inside the handle a plastic hollow cylinder joint separated the low and high pressure chambers. The handle with the input and output gas ports is shown in figure 6.8.

6.3.5 Cooling effect of Air and CO_2

For cooling the applicator, Air and CO_2 have been used. Air has the advantage that it can be released safely in the operating environment. CO_2 has the advantage that it is non flammable and can be removed by the respiratory system in the case of absorption of CO_2 through the tissue. The maximum running pressure for the cooling circuit applicator was 3 bars.

It can be shown that in steady convection flow and laminar regime, the velocity distribution is a function of the geometry and the Reynolds number. The temperature distribution is a function of the geometry, the Reynolds number and the Prandtl number [46]. The Prandlt number is defined as the ratio between the momentum diffusivity and

Properties at 300 K	Density $[kgm^{-3}]$	viscosity $[Nsm^{-2}]$	Prandtl number
Air	1.1614	184.6E-7	0.707
CO_2	1.773	149E-7	0.766

Table 6.1: Properties of Air and CO_2 at 300 K [39]

thermal diffusivity:

$$Pr = \frac{\nu}{\alpha} = \frac{C_p \mu}{k} \tag{6.1}$$

with $\nu[m^2 s^{-1}]$ the kinematic viscosity, $\alpha[m^2 s^{-1}]$ the thermal diffusivity and $k[Wm^{-1}K^{-1}]$ the thermal conductivity. For most of gas, the Prandlt number is around 0.75 which means that heat conduction and heat convection are comparable. To compare the cooling effect between the CO_2 and the air, both Reynolds and Prandlt number were compared.

The Reynolds numbers and Prandlt numbers are calculated by using the physical properties of Air and CO_2 from the table 6.1.

During the measurement, for the same pressure drop of 3 bars, the volume flow rate of air was $5\,lmin^{-1}$ and the volume flow rate of CO_2 was $3.25\,lmin^{-1}$. The corresponding mean velocity of Air and CO_2 are respectively $140\,ms^{-1}$ and $91\,ms^{-1}$. The Reynolds numbers calculated for the caracteristic length of 0.2 mm which is the interstitial space between the coaxial cable and the shaft give respectively $Re_{Air} = 1760$ and $Re_{CO_2} = 2170$. The ratio between both reynolds number is:

$$\frac{Re_{CO_2}}{Re_{Air}} = 1.23 \tag{6.2}$$

Two convective flows are similar if their Reynolds and Prandlt numbers are the same. Because these two numbers for the Air and CO_2 gas are close for the same geometry channel, initial temperature and input pressure, Air and CO_2 gas have a similar cooling effect.

During the measurement, for the same input pressure, there were no significant difference between both gases regarding their effectiveness to cool the shaft

6.4 Applicator testing

6.4.1 $|S_{11}|$ measurements

To evaluate the applicator capability to transmit microwave energy into the tissue, the magnitude of the S_{11} parameter was measured in water with the Network Analyser. The reflected power is minimum at 2.8 GHz and $|S_{11}|$ is below -10 dB between 2.4 GHz and 3.4 GHz as shown in figure 6.9.

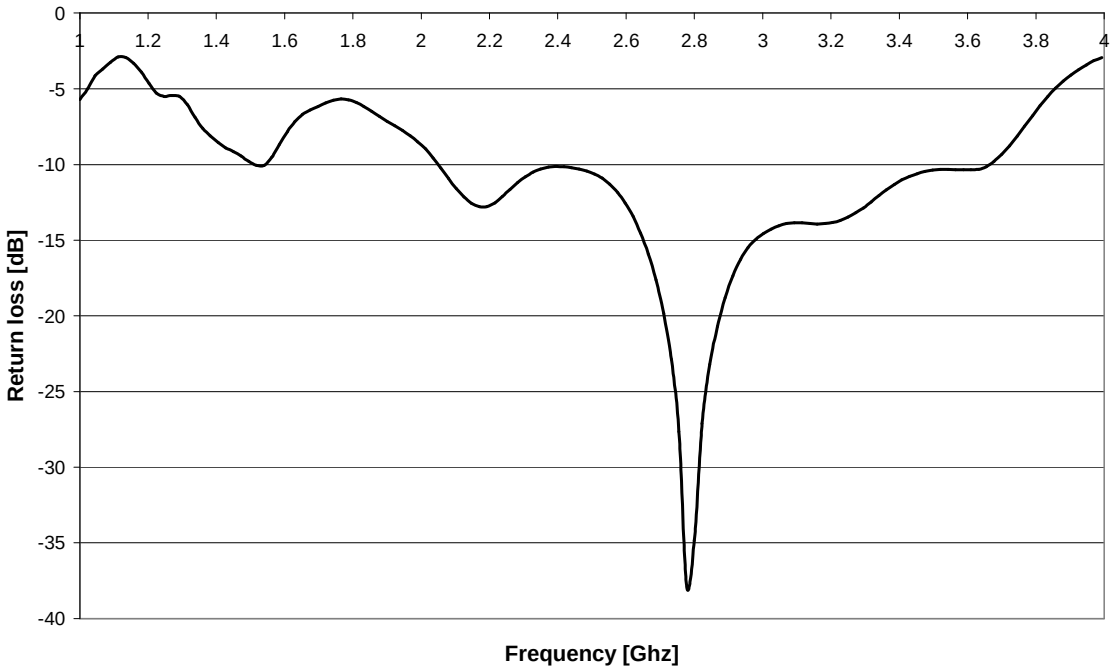

Figure 6.9: Measurement of the $|S_{11}|$ parameter in water for the 5 mm gas cooled applicator

6.4.2 Ex vivo bovine liver ablation

Tests were performed at 100, 150 and 200 watts in bovine liver to record the temperature along the shaft of the 5 mm applicator. Four thermocouples T2, T3, T4, T5 were placed at intervals of three centimetres and thermocouple T5 was located at a distance of 2.5 cm from the copper ferrule as shown in figure 6.10.

Two runs at 100 watts were performed in bovine liver tissue at an initial temperature of 27 °C for a time duration of typically five minutes. The air flow rate was $10\,lmin^{-1}$ with an input initial temperature of 10 °C. Temperature profiles of the four thermocouples are

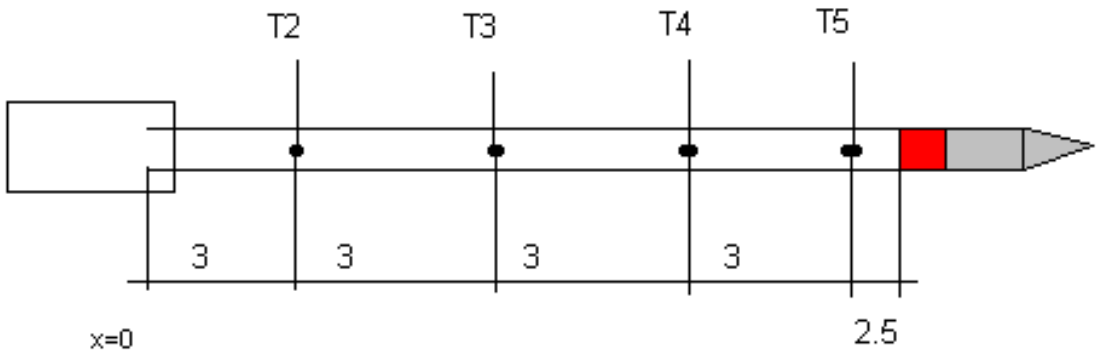

Figure 6.10: Location of the thermocouple on the shaft of the 5 mm gas applicator, distance in cm

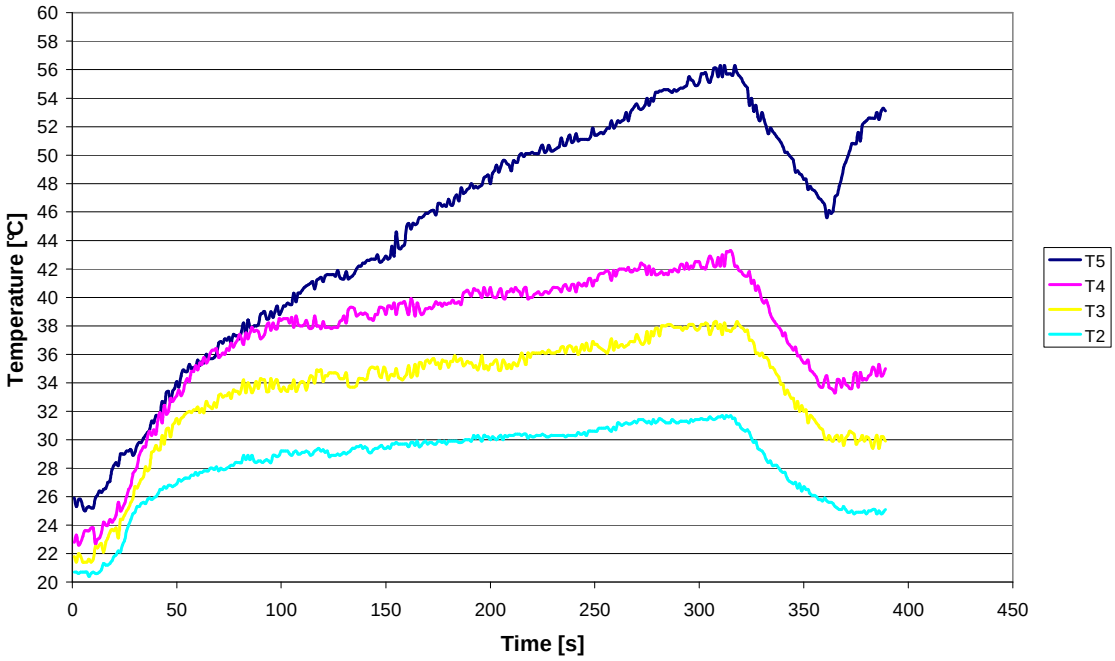

Figure 6.11: Temperature measurements along the shaft during an ex vivo liver ablation at 100 Watts. The air flow was $10\,lmin^{-1}$ with air entry temperature of 10 °C

shown in figures 6.11 and 6.12.

For the first run, the temperature of the thermocouple T4 is below 44 °C and below 46 °C for the second run. For both runs shown in figures 6.12 and 6.11 thermocouples T3 and T2 remains respectively below 38 °C and 32 °C. Thermocouple T5 is in the thermal ablation zone, so the temperature of T5 increased as the ablation volume increased and the effect of gas cooling is less visible.

The sudden drop of temperature of all four thermocouples occurred when the microwave power was switched off at time $t = 320\,s$ while the air flow is maintained. Then, the temperature of these thermocouples increased temporarily again when the air flow is switched off. This is due to the heat flux coming from the ablated volume at high temperature and propagating along the shaft. For the first run shown figure 6.11, a thermal equilibrium is nearly reached during the microwave energy deposition process. Between time $t = 100\,s$ and $t = 320\,s$ temperature of thermocouples T2, T3 and T4 increased slightly. The increase is approximately 4 °C for T3 and T4, and 2 °C for T2.

For the second run shown in figure 6.12, quasi thermal steady regime is achieved between time $t = 100\,s$ and $t = 320\,s$. Temperature of T4 increased of 6 °C, 4 °C for T3, and 2 °C for T2.

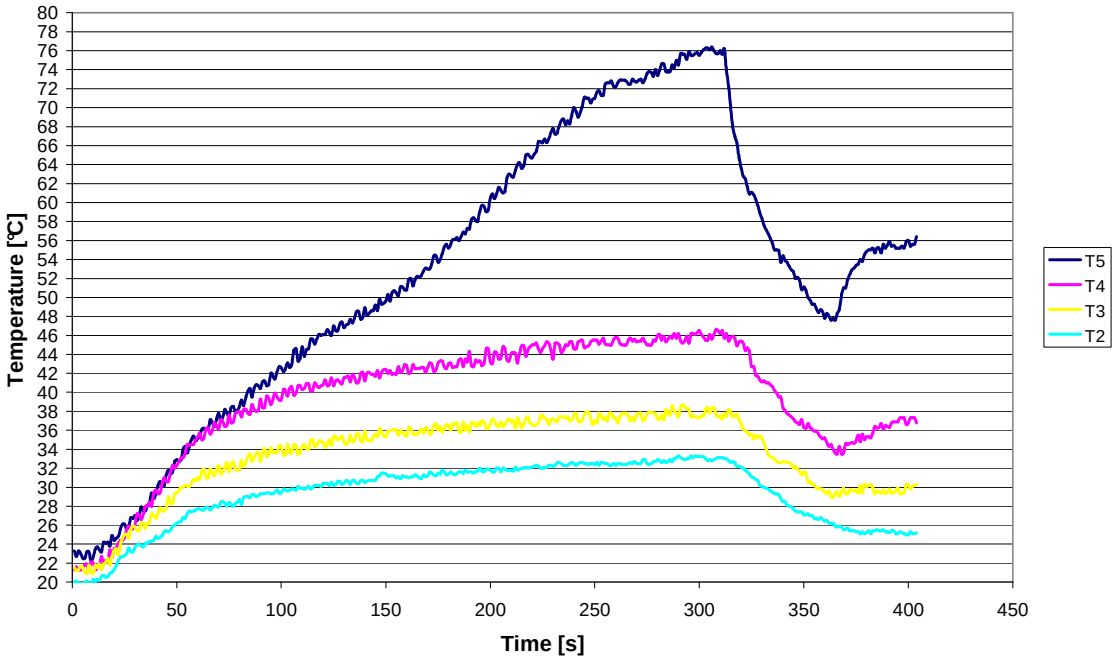

Figure 6.12: Temperature measurements along the shaft during an ex vivo liver ablation at 100 Watts. The air flow was 10 $lmin^{-1}$ with air entry temperature of 10 °C

6.4.2.1 Conclusion

These results showed that cooled air is effective in cooling the shaft of this microwave applicator. The temperature of thermocouple T4 is slightly higher than 42 °C with an air input temperature of 10 °C. By using colder air at 0 °C, the temperature of T4 would be below 42 °C. Figure 6.13 showed a thermal ablation performed at 100 watts in bovine liver with the microwave cable and the air tube supplied connected to the applicator. During these ex vivo ablation bovine liver no trace of burnt tissue along the shaft was found, this means that the air flow was cooling the stainless steel shaft efficiently.

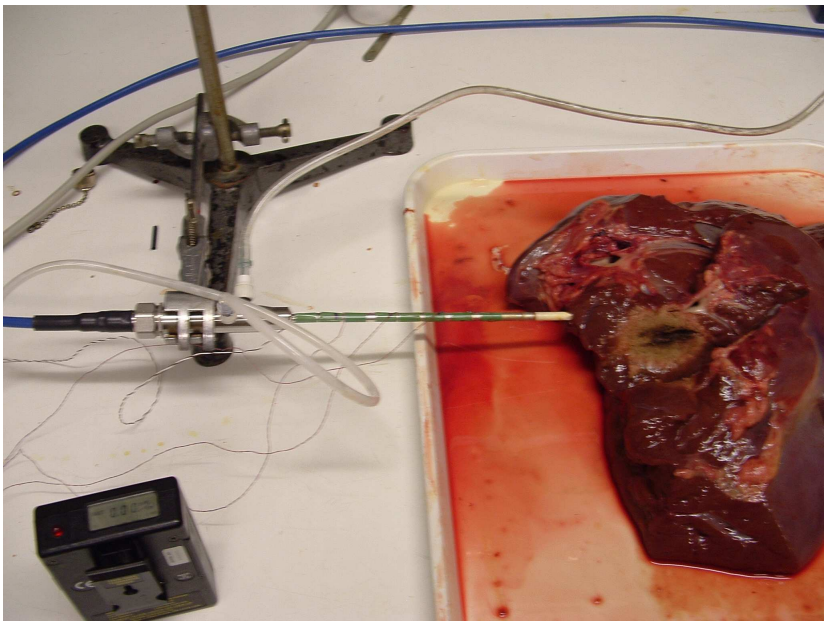

Figure 6.13: Liver ablation performed with the 5 mm gas cooled applicator, power 100 watts, lesion 5-6 cm diameter, $T_{air} = 10\,^{\circ}\mathrm{C}$, flow rate = $10\,lmin^{-1}$

6.5 Summary

The construction of this applicator is based on that of the 5 mm open water cooled applicator. With the use of an air filled coaxial cable, a cooling circuit was designed and implemented on the applicator. Temperature measurements along the shaft of the 5 mm applicator have demonstrated that an air or CO_2 gas cooled applicator is a feasible solution for liver thermal ablation for the 5 mm applicator. Gas cooling has special interest for small diameter applicators because of the impracticality of liquid cooled solutions. A smaller diameter applicator (2.4 mm) is described in the following chapter.

Chapter 7

2.4 mm gas cooled applicator

7.1 Introduction

Using the design of the air filled coaxial cable and the 5 mm applicator described in chapter 6, a gas cooled 2.4 mm diameter applicator for percutaneous use has been designed and built. The main application of the 2.4 mm gas cooled applicator is the thermal ablation of liver tumours. This applicator could also be potentially used for kidney, brain and bone tumours.

For patients with renal tumours who are not candidates for surgery, minimal invasive procedures such as radiofrequency ablation are technically feasible and give some encouraging results [49]. Anzai *et al* [4] have performed radiofrequency ablation of primary and metastatic brain tumours in 15 patients. Takahashi *et al* [71] have performed radiofrequency ablation involving 30 patients with malignant brain tumours. Percutaneous techniques such as cryoablation, radiofrequency ablation and microwave ablation have also been tested on bone tumours [10]. Overall, with little adjustments to the applicator according to the particular organ, the small gas cooled percutaneous applicator has a large range of potential applications.

7.2 Specifications

As for the open loop applicator, the gas cooled applicator has a sharp ceramic trocar tip to penetrate the tissue easily and a robust and rigid stainless steel shaft. The surgeon manipulates the applicator by the handle which has an ergonomic design and is the connection between the shaft and the coaxial cable. In addition, the use of a coating polymer deposited on the stainless steel shaft minimizes the friction between the shaft and the tissue and facilitate the insertion and removal of the applicator.

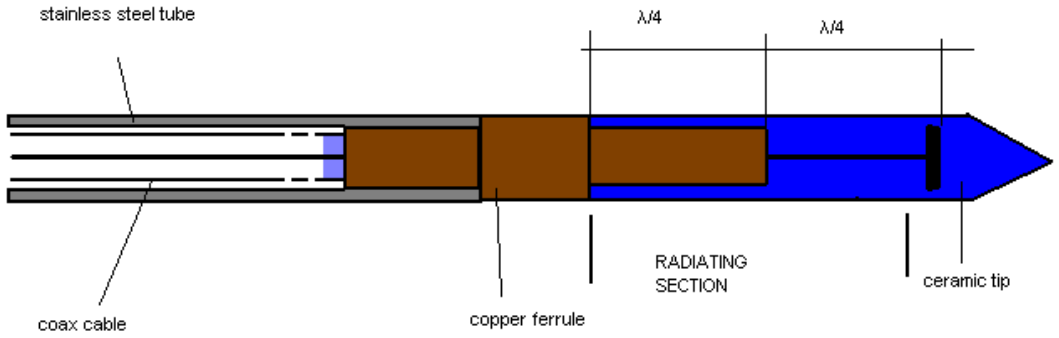

Figure 7.1: Air filled coaxial cable and radiating antenna of the 2.4 mm gas cooled applicator

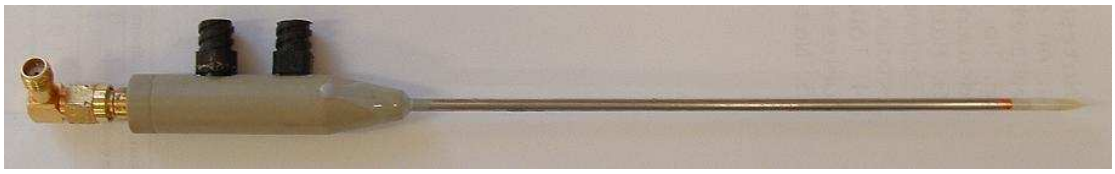

Figure 7.2: 2.4 mm gas cooled applicator

7.3 Applicator design

7.3.1 Principle of operation

The radiating tip shown in figure 7.1 is the same as the 2.4 mm applicator open loop described in chapter two. The major difference is that the applicator is constructed using an air filled coaxial cable shown in figure 7.3 and that there is no fluid exiting into the ablation volume. The 2.4 mm gas cooled applicator is shown in figure 7.2.

7.3.2 1.8 mm air filled coaxial cable

Dimensions of the air filled coaxial cable of the applicator are shown in figure 7.3.

The center conductor was insulated with a thin heat shrink PTFE tube. No spacers were used to centre the center conductor in the center of the coaxial cable, it has been shown in chapter 5, that the characteristic impedance varies slightly with the eccentricity.

The coaxial cable of 1.8 mm in diameter shown in figure 7.4 has small holes of 0.6 mm diameter on both ends to allow the gas to flow inside the coaxial cable.

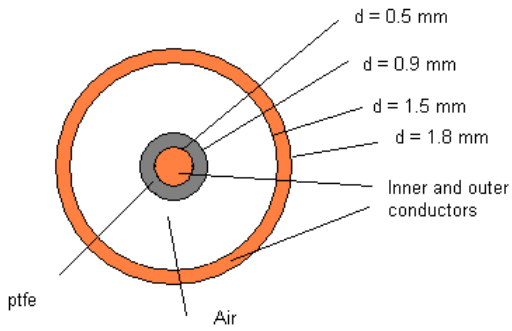

Figure 7.3: Cross section of an air coaxial cable

Figure 7.4: Air coax cable with two holes of 0.6 mm diameter

7.3.3 2.4 mm applicator handle

The handle is a plastic (Acetal) tube which connects the shaft and the coaxial cable as shown in figure 7.5. High and low pressure chambers located inside the handle are connected to two channels of the applicator. The seal between the high pressure chamber and the low pressure chamber is made of plastic acetal cylinder incorporating an elastic o-ring as shown in figure 7.6.

Figure 7.5: Handle with the acetal plastic joint visible

Figure 7.6: Acetal plastic attached to the coaxial cable

7.3.4 Closed loop circuit

On the proximal end of the applicator, the handle is the part of the device that the surgeon can hold and where the connector is attached. The gas closed loop circuit is similar to the one used with the 5 mm applicator presented in chapter 6. The cold air flows in the annular space between the annular space between the inner coaxial cable and the center conductor and returns between the inner shaft and the coaxial cable. During the thermal ablation tests in bovine liver, an air flow rate of $5\,lmin^{-1}$ was used in order to cool the shaft sufficiently.

To measure the volumetric flow rate, a thermal mass flow meter was connected between the compressed air bottle source and the input gas located on the left chamber of the handle.

7.4 Applicator testing

The applicator was tested in bovine liver and the shaft temperature was recorded by four thermocouples. The CO_2 gas was cooled with a heat exchanger .

7.4.1 Heat exchanger

A gas temperature of $-20\,^{\circ}$C, was achieved with an experimental heat exchanger shown in 7.7. It was made of seven meters of copper tube with an inside diameter of 3 mm and 5 mm outside diameter. The tube was coiled to fit in a plastic bottle. The copper tube was surrounded by ice at a temperature of $-30\,^{\circ}$C and the plastic bottle was surrounded by solid dry ice CO_2 of temperature around $-80\,^{\circ}$C. The plastic bottle with ice containing the copper tube and the dry ice CO_2 were put in an expanded polystyrene bucket for insulation.

Figure 7.7: Experimental heat exchanger

7.4.2 Experimental set up

The 2.4 mm gas closed loop applicator was tested in bovine liver with the microwave power on. A few runs at 60 watts and 80 watts at 2.45 GHz were performed for 4 to 5 minutes. Locations of thermocouples on the shaft of the applicator with the distance are given in figure 7.8.

In figure 7.9 the experimental set up used to perform ex vivo bovine liver with the 2.4 mm gas cooled applicator is shown. On the left of the picture, thermocouples lead to a computer out of picture and the microwave cable connects a microwave source. In the middle of the picture, the applicator inserted in the bovine liver and the heat exchanger used to cool the gas can be seen. The thermal mass flow meter and the pressure sensor appear on the right of the picture. The microwave source with the power meter is in foreground of the picture with the compressed gas bottle behind.

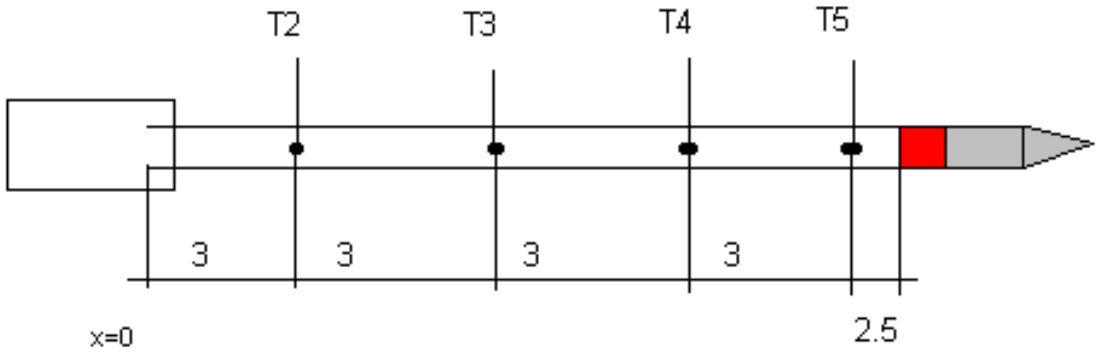

Figure 7.8: Location of thermocouples along the shaft, distance in cm

Figure 7.9: Installation for liver ablation with the 2.4 mm gas cooled applicator. From left tor right: flexible cable, heat exchanger, applicator, bovine liver, mass flow meter, pressure sensor, compressed Air bottle, microwave source.

7.4.3 Ex vivo bovine liver ablation

Ablations at 60 and 80 watts have been performed for 5 minutes in bovine liver. Temperatures recorded by each thermocouple were plotted versus time as shown in figures 7.10 and 7.11. The flow rate was $3.5\,lmin^{-1}$ and the gas used was CO_2 cooled with the heat exchanger. A temperature of $-16\,°C$ for gas entry was achieved with the experimental heat exchanger. The input and output temperature of the gas were recorded with thermocouples T6 and T5, respectively.

7.4.3.1 Liver ablation at 60 watts

For the run at 60 watts from figure 7.10, the applicator was pre cooled for 50 s with the gas flowing inside the device and then the microwave power was switched on at time $t = 60\,s$. Temperatures of the shaft increased until $t = 150\,s$ and then they start to stabilize around a given value. In this quasi steady state region, the temperature of thermocouple T2 located at 2.5 cm from the copper ferrule remained below $40\,°C$. Temperature of thermocouples T3 and T4 remained respectively below $24\,°C$ and $16\,°C$. The input gas

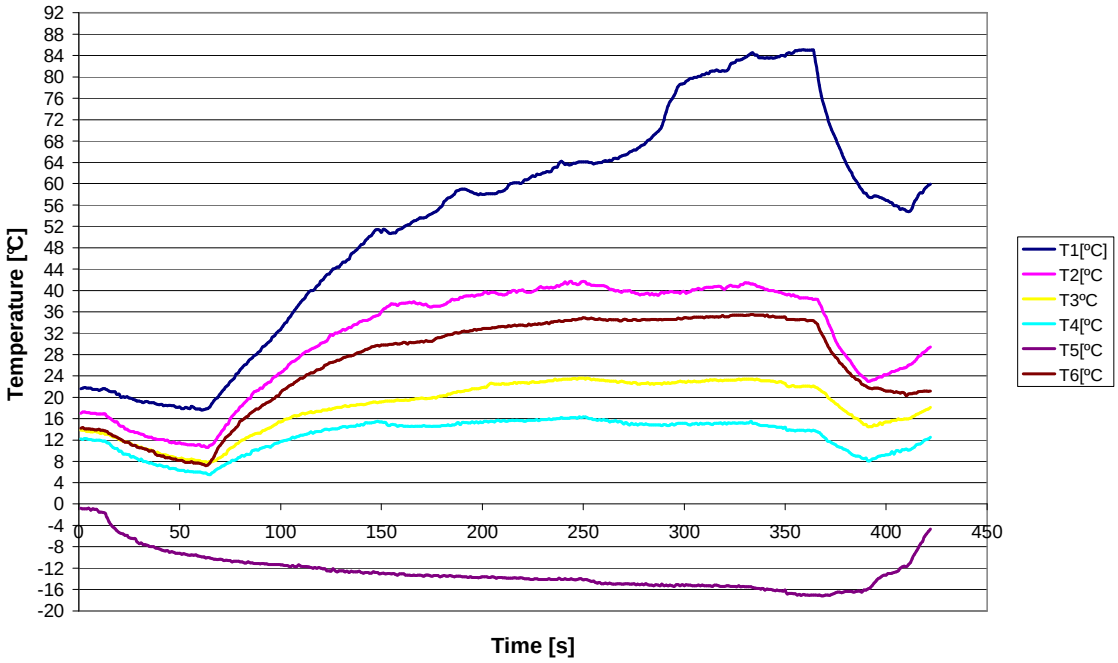

Figure 7.10: Run at 60 watts, flow rate of CO_2 at $3.25\,lmin^{-1}$

temperature was between $-12\,°C$ and $-16\,°C$. At the end of the run, at time $t = 380\,s$, the microwave power was switched off while CO_2 gas was still cooling the applicator. As a result, all temperatures decreased. At time $t = 390\,s$, temperature started to increase again when the gas flow was switched off.

The average gas input and output temperature in the steady region are respectively around $-15\,°C$ and $34\,°C$. At $-15\,°C$, the specific heat of the CO_2 gas is $C_p = 807 Jkg^{-1}K^{-1}$ and the density $\rho = 2.045\,kgm^{-3}$. The heat transfer to the fluid can be calculated with equation 7.1 showing that the power transmitted to the fluid is 4.7 watts.

7.4.3.2 Liver ablation at 80 watts

The temperature curves for the run at 80 watts shown in figure 7.11 are similar to the run at 60 watts of figure 7.10. Temperature of thermocouple T2 remained below $42\,°C$. Temperature of thermocouples T3 and T4 remained respectively below $22\,°C$ and $16\,°C$. The input gas temperature was between $-14\,°C$ and $-20\,°C$.

For this run, the average input and output gas temperature are respectively $-16\,°C$ and $38\,°C$. With the same flow rate and thermal properties as in the run at 60 watts, the power transmitted to the fluid is 5.2 watts.

From these shaft temperature measurements, it was concluded that a flow rate of $3.5\,lmin^{-1}$ of CO_2 or $5\,lmin^{-1}$ of air with an input temperature of $-20\,°C$ was sufficient to cool the shaft during a 5 minute microwave ablation performed at 80 watts.

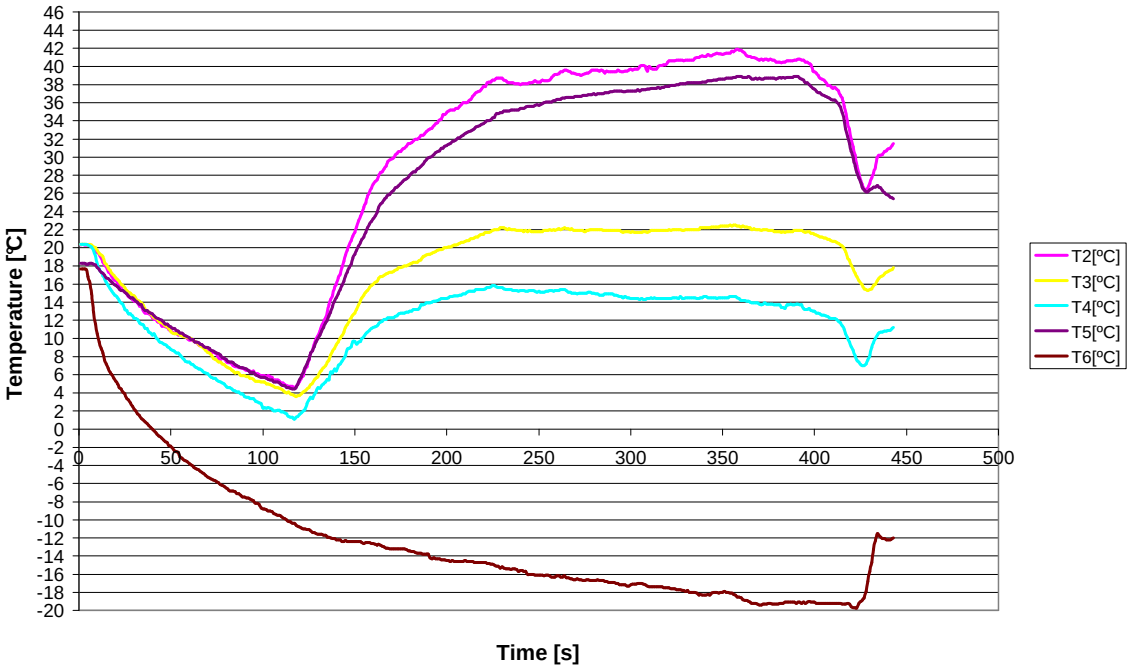

Figure 7.11: Run at 80 watts, flow rate of CO_2 at $3.5\,lmin^{-1}$

In figure 7.12, a liver ablation of 4 cm diameter is shown. As expected, diameters of liver burns were the same size as the burns performed with the open loop 2.4 mm open loop water cooled applicator. It can be seen that the tissue is nearly carbonized near the ceramic tip due to a high microwave field in the vicinity of the ceramic trocar tip. Estimated temperatures achieved in liver tissue near the ceramic tip were between 150 °C to 250 °C from experimental measurement and computer modelling.

Figure 7.12: Liver ablation with the 2.4 mm gas cooled applicator, 5 min 80 watts

7.5 Energy balance for the gas cooled applicator

In figure 7.13 is plotted the power transfer to the gas for different runs performed in liver at a flow rate of 3.5 $lmin^{-1}$ of CO_2 at 60 watts and 80 watts. The heat flux q was calculated as the product of the mass flow $\dot{m}$ with the specific heat capacity C_p of the gas and the temperature difference between input and output gas port:

$$q = \dot{m} C_p \left(T_{out} - T_{in}\right) \tag{7.1}$$

With $\dot{m}$ the mass flow rate, C_p the thermal specific heat of the CO_2, T_{out} the temperature of the exhaust gas and T_{in} the temperature of the gas at the entrance of the applicator. Power transmitted to the gas constantly increased during the thermal ablation. One minute after the run, heat flux increased slightly at a rate between 0.2 and 0.3 $Wmin^{-1}$. Once the microwave power is switched off, the heat flux quickly decreases because less and less heat is transfered to the gas. For the run with a microwave power of 80 watts, the heat transfer to the gas is between 4 and 5 watts.

The figure 7.14 gives the overall energy balance of the gas cooled applicator during a thermal ablation. The different powers are calculated or estimated such as the reflected power, the power loss due to electrical dissipation and the power radiated from the tip. For example a match for the applicator of -10 dB is usually considered as the limit for a reasonably good applicator. Above -10 dB, more than 10 % is reflected back, which lowers the performance of the device. Therefore a good design radiating section of the applicator is essential to minimize the reflected power and heat losses along the device.

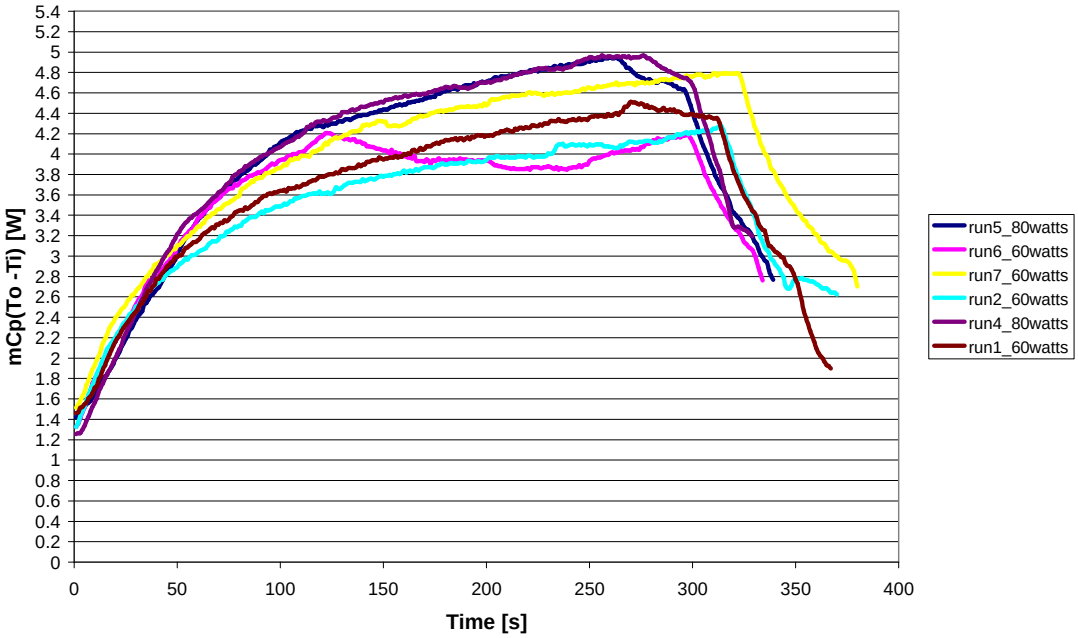

Figure 7.13: Heat flux taken by the CO2 gas

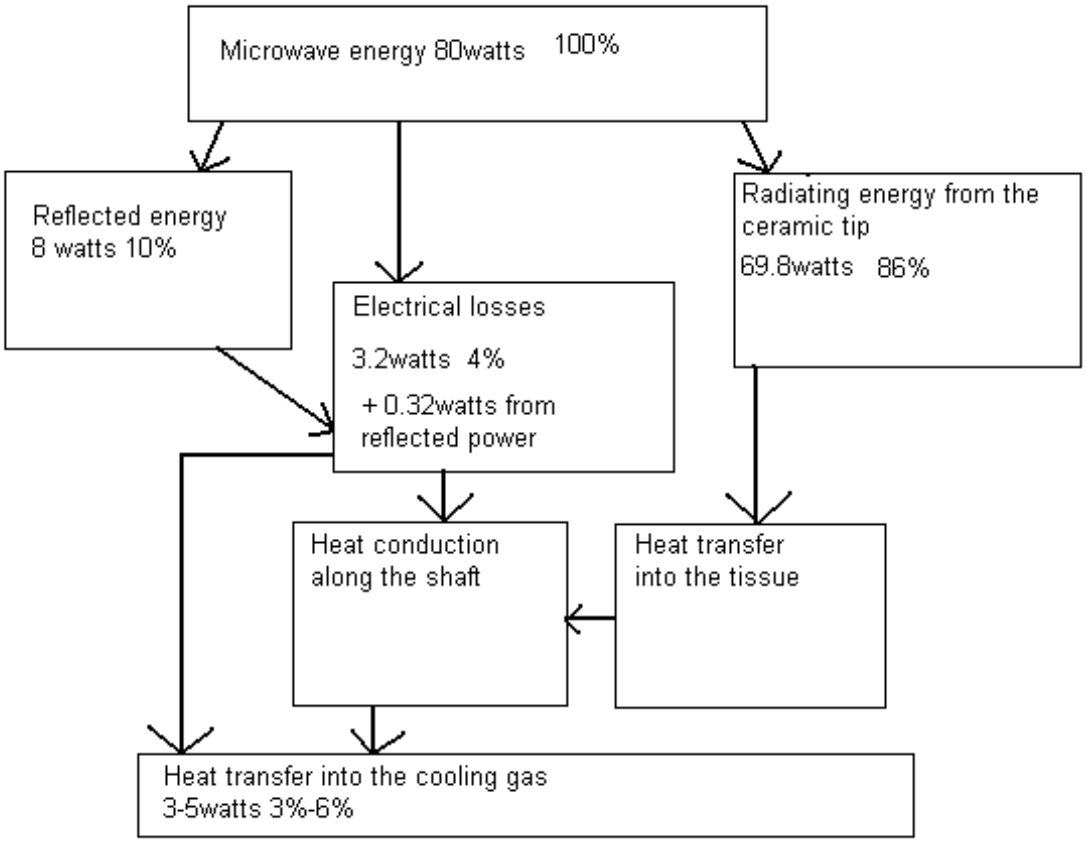

Figure 7.14: Energy balance for the gas cooled applicator

Electrical loss occurs during propagation of microwaves in the coaxial cable made of PTFE. For a standard 20 cm length for the applicator, it was found that these losses count for 4 % of the total input energy.

The remaining energy evaluated at 86 % is emitted from the radiating section. It has to be noted that the radiating section made of the ceramic and the copper ferrule is soldered on the copper coaxial cable and the stainless steel shaft is connected to the copper ferrule. Thus, heat transfer also occurred along the coax cable and the shaft toward the handle.

The power transferred to the fluid calculated was in the range of 3 to 5 watts as shown in figure 7.13, the power taken by the gas represents 3.75 % to 6.25 % of the overall power.

7.6 Summary

A 2.4 mm gas cooled applicator has been built which exhibits a shaft temperature below 42 °C for ablation powers up to 80 watts. The range of potential applications of thermal ablation on different organs is wider because no water is flowing in the tissue. The second advantage is that the air filled coaxial line is internally cooled and the applicator can be safely used at higher power. The main drawback is the need of a cold air supply unit to provide cold air to the input of the applicator.

Chapter 8

Concluding notes

8.1 Thesis summary

8.1.1 Introduction

This thesis describes an approach to the development of efficient microwave applicators by using both computer modelling, construction of prototypes and testing. A gas cooled solution to the problem of shaft heating was implemented successfully on a 5 mm laparoscopic applicator and 2.4 mm percutaneous applicator.

8.1.2 Water cooled open loop applicators

A 5 mm microwave laparoscopic open loop applicator has been designed and tested using a design similar to an earlier 2.4 mm open loop applicator. The 5 mm applicator open loop allows the ablation of large tumours of 5-7cm diameter in 4 minutes with power up to 200 watts. Finite element electromagnetic models have been used for the prediction of the loss return and the energy field distribution.

A 2.4 mm percutaneous applicator designed in the Medical Device Technology Group and used in a clinical trial has been presented. Its design formed the basis of the development of a 2.4 mm percutaneous gas cooled applicator.

8.1.3 Fluid movements

Fluid movements in the ablation zone have been discussed and demonstrated with a sponge experiment showing some interstitial fluid movements in a porous medium during microwave heating. An experiment with a gamma camera has shown some fluid movements in bovine liver during a thermal ablation.

Water cooled open loop applicators have the drawback of adding some fluid to the tissue and potentially the ablation area. This can enhance the effect of fluid movements during ablation and may cause undesirable burns along vessels outside the targetted tumour.

In spite of this, water deposition inside the ablated area may be advantageous for the following reasons :
- An open water circuit is easy to integrate in a percutaneous applicator.
- Deposition of water inside the ablated volume also attenuates the tissue dessication process and gives a better overall thermal efficiency than a closed loop solution.
- Due to the high latent energy of vaporization of water, the water acts as a temperature limiter and absorbs a lot of energy during the transformation phase liquid to steam.
However, for some organs such as lungs or bones, water deposition is not at all desirable and must be avoided.

On balance, the problem associated with the input of fluids to the ablation outweigh the advantages of the open loop solution and therefore a non perfused solution to the cooling problem is essential.

8.1.4 Air filled coaxial cable

As an alternative to an open loop cooling circuit, a gas closed loop cooling circuit has been designed.

This design utilizes an air cooled coaxial cable which has been built and used for the design of the two closed loop circuit applicators. It allows efficient microwave transmission to the radiating section of the applicator and a compact gas cooling circuit. Temperature measurements for different flow rates, input temperature and direction of flow have been compared with a finite element fluid thermal model and a good agreement was obtained between measured and predicted temperatures along the shaft.

8.1.5 Gas cooled applicators

The gas cooling circuit using the air filled coaxial cable solution has been implemented in 5 mm and 2.4 mm diameter applicators and has been successfully built and tested in ex vivo bovine liver. For the 2.4 mm applicator, the temperature of the shaft remained below 42 °C during a microwave ablation at 80 watts for 5 minutes.

The advantages of these applicators are a greater range of potential treatments on different organs such as liver, kidney, lungs and bone cancer. A summary of these applicators with their characteristics and target organs is given in table 8.1.

Diameter of the shaft [mm]	5	2.4	5	2.4
Cooling circuit	open, water	open, water	closed, Air, CO_2	closed, Air, CO_2
Procedure	Laparoscopic	Percutaneous	Laparoscopic	Percutaneous
Organ	Liver	Liver	Liver	Liver, kidney, lungs, bones, brain
Power [W]	100-200	40-80	100-200	40-80
Lesion size [cm]	4-7	2-5	4-7	2-5

Table 8.1: Summary for the laparoscopic and percutaneous applicators characteristics

8.2 Discussion

The process of developing a microwave thermal ablation applicator involves the following engineering disciplines:
- electromagnetic modelling of the radiating section of the applicator.
- mechanical construction of the applicator prototype.
- thermal heat transfer analysis of the cooling circuit of the applicator.
- biology and heat transfer through the tissue.
- mathematical analytical model to obtain some quantitative information related to the applicator.

8.2.1 Electromagnetism

The fundamental working part of a microwave applicator is the radiating section. An effective radiating antenna is obtained after a electromagnetic analysis using usually a finite element package which allows us to perform a parametric analysis in order to design an optimal radiating section. During this development phase, four main characteristics are needed for a efficient applicator:
- the reflected power has to be minimized. A criterion usually used is to require $|S_{11}|$ to remain below minus 10 dB.
- the reflected power must to remain low during the ablation including tissue dessication. This implies designing a radiating section with a low return loss below minus 10 dB over 1 GHz band, from 2.45 GHz to 3.5 GHz for example.
- the radiating section has to be not too sensitive to small length variations coming from the machining tolerance.
- the field shape should be as near to spherical since soft tissue tumours tend to be

approximatly spherical.
Once the critical lengths of the radiating section have been determined, the construction of the applicator must be practically viable.

8.2.2 Mechanical construction

Percutaneous ablation required a rigid, sharp and robust device. These specifications determined the mechanical design and the method of assembly.

To achieve robustness careful attention must be paid to the materials used and the method of construction. In addition to the ceramic and metal components, all items such as glues, solders, coating materials, must be selected to withstand temperatures which can exceed 250 °C. Finally, attention must be paid to relative thermal expansion and other mechanical considerations if the device is not to fail during a treatment.

8.2.3 Fluid and thermal heat transfer

During the development of these applicators, a cooling circuit has to be integrated in the device, this is important for two main reasons:
- a cooling system has to be integrated to the device in order to maintain a shaft temperature below 41 °C to avoid burns of the normal tissue surrounding the applicator.
- a cooling fluid is also required to keep the applicator parts below any excessive temperature which could damage or destroy the applicator itself at high power levels.
A finite element model can be used to make a coupled thermal fluid analysis which will predict the temperature field along the shaft applicator for a given flow rate.

8.2.4 Biological consideration

Biological tissues have complex structures with high fluid content. During a microwave ablation, a pressure gradient occurs in the volume around the ceramic tip leading to fluid movements. These fluid movements were one of the reason why a closed loop cooled applicator was desirable, because no water is deposited in the tissue.

During ablation, a dessication process occurs in which the water content of the ablated volume decreases and the electrical, thermal and mechanical properties of the tissue change.

In order to have a good microwave transmission during all the ablation procedure, it is important to design an applicator with a low $|S_{11}|$ over a large band of frequencies since this translates into a relatively high tolerance to changes in tissue properties.

8.2.5 Analytical models

Analytical calculations were useful to assess important variables concerning the applicator. For example in the cooling circuit of the gas applicator the pressure drop as a function of the volume flow rate for an annular geometry was calculated in appendix A.

During the study of the coaxial cable, some values needed to be calculated especially:
- the loss of the cable calculated in appendix E.
- the variation of the characteristic impedance relative to the eccentricity of the inner conductor calculated in appendix D.

During a microwave thermal ablation, high temperatures occur in the vicinity of the radiating section. Thermal stress exists in the different part of the radiating section, especially in the copper ferrule and the ceramic tip. In appendix B the thermal stress in the copper ferrule and the ceramic was calculated to quantify the magnitude to the internal stress.

Overall, it was found that these various calculations were quite useful in order to check the viability of a proposed design. Futhermore, these models are used to check the validity of some finite element models.

8.3 Current research in Bath

The current research in the Medical Device Technology Group is composed of different areas:
- antenna design for new microwave applicators.
- construction of prototypes.
- clinical collaboration with various surgerons interested in minimally invasive microwave ablation.
- computer modelling in electromagnetism, heat transfer and fluid mechanics.

8.3.1 1.8 mm water cooled applicator

A 1.8 mm percutaneous using a similar design to the 2.4 mm applicator has been designed and developed by I.Wieland in the Bath Medical Technology Group. This applicator incorporates a closed water cooled cooling system and performs ablation up to 5 cm in diameter at 100 watts for 4 minutes.

The compact cooling circuit was developed without using the space inside the coaxial cable but only the annular space between the coaxial cable and the shaft. The creation of two channels in the annular space allows the use of water as a cooling fluid because the cooling circuit is distinct from the microwave circuit contrary to the gas applicator.

8.3.2 Construction of prototype

The company Microsulis has the intention to market the 1.8 mm water cooled closed loop applicator. This applicator has very good performance and would be quite effective for treating liver tumours using non invasive surgery and percutaneous route.

8.3.3 Clinical trial

A clinical trial was started in 2005 with an interventional radiologist Professor W. Lees from University College Hospital of London and Dr P. Clegg from the Medical Device Technology Group at Bath University.

This clinical trial is still running and will give important information from the surgeon concerning the manipulation and the possible design improvement of the applicator.

8.4 Suggestions for further research

8.4.1 Gas cooled applicators

The use of the inner space of the coaxial cable gives a very compact applicator because the gas is used as a dielectric for the coaxial cable.

For a very small percutaneous applicator with diameter around 1 mm, the gas circuit could be the only solution for the cooling circuit by using the annular space inside the coaxial cable because space would be not sufficient for a water cooling solution.

The implementation of the gas circuit gives the first closed loop gas cooled microwave applicator developed in the Medical Technology Group. In order to make a convenient product, a gas cooled applicator will have to incorporate a compact cooling unit to lower the Air or CO_2 temperature around $-20\,^{\circ}\mathrm{C}$.

8.4.2 Computer modelling

Finite element models which iteratively solve the electromagnetic and thermal problem have been developed [30]. It allows us to predict the temperature in the tissue around the applicator tip for a given microwave power and time. It is possible to take into account the change of the tissue properties during the dessication process by defining some electrical and thermal properties of the tissue as functions of the temperature. These models do not incorporate the effect of the cooling fluid. Instead an adiabiatic boundary is imposed on the appropriate boundary of the model.

During the development of cooling circuits described in this thesis a fluid thermal model has been created and compared with measurements as decribed in chapter 5. This model does not incorporate the temperature field obtained from an electromagnetic analysis, instead an imposed temperature is applied on the appropriate boundary.

The next step in the development of accurate models is to predict the shaft temperature of the applicator during a thermal ablation by taking into account the effect of the cooling circuit. This would allow us to take into account the effect of the cooling fluid, and to predict the temperature field of the applicator with its surrounding tissue.

Acknowledgements

Above all, I wish to thank Professor Nigel Cronin for his support and guidance throughout this work.

I would also express my gratitude to Dr Peter Clegg and Dr Adam Guy for their availability and assistance during my work. My thanks also go to all the technical staff from the physics departement, especially Bob Draper and Cathy Dyer for their support and help during the building and testing of the prototypes.

I am grateful for the funding provided by Microsulis Medical Ltd.

Finally, I would like to thank my family.

References

[1] R. Adam, E. J. Hagopian, M. Linhares, J. Krissat, E. Savier, D. Azoulay, F. Kunstlinger, D. Castaing, and H. Bismuth. A comparison of percutaneous cryosurgery and percutaneous radiofrequency for unresectable hepatic malignancies. *Archives of Surgery*, 137(12):1332–1339, December 2002.

[2] Z. Amin, S. G. Bown, and W. R. Lees. Local treatment of colorectal liver metastases - a comparison of intertitial laser photocoagulation and percutaneous alcohol injection. *clinical radiology*, 48(3):161–171, September 1993.

[3] D. Andreuccetti, M. Bini, A. Ignesti, R. Olmi, N. Rubino, and R. Vanni. Use of polyacrylamide as a tissue-equivalent material in the microwave range. *IEEE Transactions on Biomedical Engineering*, 35(4):275–277, 1988.

[4] Y. Anzai, R. Lufkin, A. Desalles, F. Farahani, A. Huang, S. Sinha, E. Behnke, and K. L. Black. Radiofrequency ablation of brain tumours using mr guidance. *Minimally invasive therapy and allied technologies*, 5(3):232–242, June 1996.

[5] J. Argyris and S. Kelsey. Energy theorems and structural analysis, part two, applications to thermal stress problems and st venant torsion. *Aircraft Engineering*, 26(310):410–422, November 1954.

[6] A. J. Bilchik, T. F. Wood, D. Allegra, G. J. Tsioulias, M. Chung, D. M. Rose, K. P. Ramming, and D. L. Morton. Cryosurgical ablation and radiofrequency ablation for unresectable hepatic malignant neoplasms - a proposed algorithm. *Archives of surgery*, 135(6):657–662, June 2000.

[7] M. G. Bini, A. Ignesti, L. Millanta, R. Olmi, N. Rubino, and R. Vanni. The polyacrylamide as a phamtom material for electromagnetic hyperthermia studies. *IEEE Transactions on biomedical engineering*, 31(3):317–322, 1984.

[8] L. Boni, A. Benevento, F. Cantore, G. Dionigi, F. Rovera, and R. Dionigi. Technological advances in minimally invasive surgery. *Expert review of medical devices*, 3(2):147–153, March 2006.

[9] A. Carbonell, C. Joels, K. Kercher, B. Matthews, R. Sing, and B. Heniford. A comparison of laparoscopic bipolar vessel sealing devices in the hemostasis of small, medium, and large-sized arteries. *Journal of laparoendoscopic and advanced surgical techniques*, 13(6):377–380, December 2003.

[10] R. Cioni, N. Armillotta, I. Bargellini, V. Zampa, C. Cappelli, P. Vagli, G. Boni, S. Marchetti, V. Consoli, and C. Bartolozzi. Ct-guided radiofrequency ablation of osteoid osteoma: long-term results. *European radiology*, 14(7):1202–1208, July 2004.

[11] P. Clegg. *Microwave ablation therapy for liver cancers.* PhD thesis, University of Bath, 2002.

[12] R. Clough. The finite element method in plane stress analysis. *Proceedings of the second ASCE conference on electronic computation, Pittsburg*, pages 345–378, September 1960.

[13] Cookson electronics company, 7645 Woodland Drive, Indianapolis, IN 46278-2707. *PDS 2010 LABCOTER 2, Parylene Deposition System, Operator's manual.*

[14] N. Cronin. *Microwave and optical waveguides*, chapter 2, pages 36–39. 1995.

[15] A. Curnier. *Méthodes numériques en mécanique des solides*, chapter 1–2. Presses polytechniques et universitaires romandes, 2000.

[16] B. N. Das, S. B. Chakrabarty, and K. S. R. Rao. Effect of dielectric support on the inner conductor of eccentric coaxial line. *IEEE Transactions on Electromagnetic Compatibility*, 37(1):71–74, 1995.

[17] E. J. Davies. Exact solutions for a class of heat and mass transfer problems. *Canadian Journal of Chemical Engineering*, 51:562–572, October 1973.

[18] D. L. Deardorff, J. D. Diederich, and W. H. Nau. Air cooling of direct coupled ultrasound applicators for interstitial hyperthermia and thermal coagulation. *Medical Physics*, 25(12):2400–2409, december 1998.

[19] M. W. Dewhirst, B. L. Viglianti, M. Lora-Michiels, M. Hanson, and P. J. Hoopes. Basic principles of thermal dosimetry and thermal thresholds for tissue damage from hyperthermia. *International Journal of Hyperthermia*, 19(3):267–294, May-June 2003.

[20] C. Diederich. Thermal ablation and high-temperature thermal therapy: Overview of technology and clinical implementation. *International Journal of Hyperthermia*, 21(8):745–753, December 2005.

[21] D. D. Dincov, K. A. Parott, and K. A. Pericleous. Heat and mass transfer in two phase porous materials under intensive microwave heating. *Journal of Food engineering*, 65:403–412, 2004.

[22] F. Duck. *Physical properties of Tissue: a comprehensive reference book*, chapter 6, pages 177–196. Harcourt Brace Jovanovich, Publishers, 1990.

[23] V. Eppert and B. S. Trembly. Air cooling for an interstitial microwave hyperthermia antenna: Theory and experiment. *IEEE Transactions on Biomedical Engineering*, 38(5):450–460, 1991.

[24] T. Gmur, J. Botsis, and M. Del Pedro. *Introduction à la mécanique des solides et des structures*, chapter 2, page 19. Presses polytechniques et universitaires romandes, 2001.

[25] L. Graetz. Uber die wärmeleitungsfähigkeit von flüssigkeiten (on the thermal conductivity of liquids). *Ann. Phys. Chem*, 18:79–94, 1883.

[26] F. Guardiol. *Electromagnétisme*, chapter 1, pages 17–20. Presses polytechniques et universitaires romandes, 2004.

[27] F. Guardiol. *Electromagnétisme*, chapter 9, pages 177–178. Presses polytechniques et universitaires romandes, 2004.

[28] F. Guardiol. *Electromagnétisme*, chapter 3, page 70. Presses polytechniques et universitaires romandes, 2004.

[29] B. Guru and H. Hiziroglu. *Electromagnetic field theory fundamentals*, chapter 1, pages 552–554. Cambridge University Press, 2004.

[30] D. Hardie. *Non linear modelling of microwave soft tissue ablation using the finite element method*. PhD thesis, Heriot watt University, school of engineering and physical science, September 2006.

[31] H. Hausen. *Heat Transfer in Counterflow, Parallel Flow and Cross Flow*, chapter 1, pages 14–15. 1976.

[32] E. Hecht. *Optics*, chapter 3, page 74. Addison Wesley, 2002.

[33] W. Hilbert. *Electrical characteristics of transmission lines an introduction to the calculation of characteristic impedances and specific capacity and inductance of homogeneous cylindrical and conical electrical transmission lines*. Artech House, 1979.

[34] C. d. Ho, H. M. Yeh, and W.-Y. Yand. Double-pass flow heat transfer in a circular conduit by inserting a concentric tube for improved performance. *Chemical Engineering Communications*, 192(2):237–255, 2005.

[35] N. Honda, Q. Guo, H. Uchida, H. Ohishi, and Y. Hiasa. Percutaneous hot saline injection therapy for hepatic tumors: an alternative to percutaneous ethanol injection therapy. *Radiology*, 190(1):53–57, 1994.

[36] F. Incropera and D. Dewitt. *Fundamentals of heat and mass transfer*, chapter 2, pages 52–55. School of mechanical engineering Purdue University. John Wiley and Sons, 1996.

[37] F. Incropera and D. Dewitt. *Fundamentals of heat and mass transfer*, chapter 8, page 421. School of mechanical engineering Purdue University. John Wiley and Sons, 1996.

[38] F. Incropera and D. Dewitt. *Fundamentals of heat and mass transfer*, chapter appendix A, page 846. School of mechanical engineering Purdue University. John Wiley and Sons, 1996.

[39] F. Incropera and D. Dewitt. *Fundamentals of heat and mass transfer*, chapter appendix A, page 839. School of mechanical engineering Purdue University. John Wiley and Sons, 1996.

[40] F. Incropera and D. Dewitt. *Fundamentals of heat and mass transfer*, chapter appendix A, pages 827–836. School of mechanical engineering Purdue University. John Wiley and Sons, 1996.

[41] H. Ishiguro and B. Rubinsky. Mechanical interaction between ice crystals and red-blood-cells during directional solidification. *Cryobiology*, 31:483–500, October 1994.

[42] A. Khaled and K. Vafai. The role of porous media in modeling flow and heat transfer in biological tissues. *International journal of heat and mass transfer*, 46(26):4989–5003, December 2003.

[43] J. A. Koutcher, D. Barnett, A. B. Kornblith, D. Cowburn, T. J. Brady, and L. E. Gerweck. Relationship of changes in ph and energy status to hypoxic cell fraction and hyperthermia sensitivity. *International journal of radiation oncology biology physics*, 18(6):1429–1435, June 1990.

[44] C. Lafon, D. Melodelima, R. Salomir, and J. Y. Chapelon. Interstitial devices for minimally invasive thermal ablation by high-intensity ultrasound. *International Journal of Hyperthermia*, 23(2):153–163, March 2007.

[45] H. Lamb. Hydrodynamics. *Ed. Dover, New York*, 1932.

[46] L. D. Landau and E. M. Lifshitz. *Fluid mechanics*, volume 6, chapter 5, pages 208–209. Institute of Physical Problems. U.S.S.R. Academy of Sciences, 1987.

[47] G. L. Lecarpentier, M. Motamedi, L. P. Mcmath, S. Rastegar, and A. J. Welch. Continuous-wave laser ablation of tissue - analysis of thermal and mechanical events. *IEEE Transactions on Biomedical Engineering*, 40(2):188–200, February 1993.

[48] E. Liapi and J. Geschwind. Transcatheter and ablative therapeutic approaches for solid malignancies. *Journal of clinical oncology*, 25(8):978–986, March 2007.

[49] K. Luia, D. Gervais, R. Arellanoa, and P. Mueller. Radiofrequency ablation of renal cell carcinoma. *Clinical Radiology*, 58(12):905–913, December 2003.

[50] P. Mazur. Role of intracellular freezing in death of cells cooled at supraoptimal rates. *Cryobiology*, 14(3):251–272, 1977.

[51] A. C. Metaxas. *Foundations of Electroheat: an unified approach*, chapter 2, pages 12–17. Wiley, 1996.

[52] L. F. Moody. Friction factors for pipe flow. *Transactions ASME*, 66:671, 1944.

[53] S. Mulier, Y. C. Ni, J. Jamart, T. Ruers, G. Marchal, and L. Michel. Local recurrence after hepatic radiofrequency coagulation. multivariate meta analysis and review of contributing factors. *Annals of Surgery*, 242(2):158–171, August 2005.

[54] V. Muralidharan and C. Christophi. Interstitial laser thermotherapy in the treatment of colorectal liver metastases. *Journal of Surgical Oncology*, 71(1):73–81, 2001.

[55] D. Pozar. *Microwave engineering*, chapter 1, page 1. Wiley, 2005.

[56] D. Pozar. *Microwave engineering*, chapter 1, page 10. Wiley, 2005.

[57] D. Pozar. *Microwave engineering*, chapter 3, pages 176–177. Wiley, 2005.

[58] D. Pozar. *Microwave engineering*, chapter 2, page 58. Wiley, 2005.

[59] D. Pozar. *Microwave engineering*, chapter 2, page 90. Wiley, 2005.

[60] I. Rhyming. *Dynamique des fluides*, chapter 7, page 296. Presses polytechniques et universitaires romandes, 1991.

[61] I. Rhyming. *Dynamique des fluides*, chapter 7, page 295. Presses polytechniques et universitaires romandes, 1991.

[62] G. Roussy and J. A. Pearce. *Foundations and industrial applications of microwave and radio frequency fields physical and chemical processes*, chapter 7, page 285. Wiley, 1995.

[63] B. Rubinsky, C. Y. Lee, J. Bastacky, and G. Onik. The process of freezing and the mechanism of damage during hepatic cryosurgery. *Cryobiology*, 27(1):85–97, February 1990.

[64] J. Seifert, G. J. Stewart, P. M. Hewitt, E. J. Boltan, T. Junginger, and D. L. Morris. Interleukin-6 and tumor necrosis factor-alpha levels following hepatic cryotherapy: Association with volume and duration of freezing. *World journal of surgery*, 23(10):1019–1026, October 1999.

[65] S. R. Smith and R. Foster, Kenneth. Dielectric properties of low water content tissues. *Physics in medicine and biology*, 30(9):965–973, March 1985.

[66] M. Sofer, G. A. Vilos, P. Borg, W. Zheng, and J. D. Denstedt. Stray radiofrequency current as a cause of urethral strictures after transurethral resection of the prostate. *Journal of Endourology*, 15(2):221–225, March 2001.

[67] A. Sommerfeld. *Mechanics of Deformable Bodies*, chapter 3, pages 101–105. Academic Press London, 1964.

[68] C. W. Song, M. S. Kang, J. G. Rhee, and S. H. Levitt. The effect of hyperthermia on vascular function, ph and cell-survival. *Radiology*, 137(3):795–803, 1980.

[69] H. Suit. Hyperthermic effects on animal-tissues. *Radiology*, 123(2):483–487, 1977.

[70] B. Swift, A. Strickland, K. West, P. Clegg, N. Cronin, and D. Lloyd. The histological features of microwave coagulation therapy: an assessment of a new applicator design. *International Journal of Experimental Pathology*, 84(1):17–24, 2003.

[71] H. Takahashi, T. Suda, H. Motoyama, T. Uzuka, S. Takahashi, K. Morita, K. Kakinuma, and R. Tanaka. Radiofrequency interstitial hyperthermia of malignant brain tumors: development of heating system. *Experimental Oncology*, 22:186–190, December 2000.

[72] R. Tateishi, S. Shiina, T. Teratani, S. Obi, S. Sato, Y. Koike, T. Fujishima, H. Yoshida, T. Kawabe, and M. Omata. Percutaneous radiofrequency ablation for hepatocellular carcinoma. an analysis of 1000 cases. *Cancer*, 103(6):1201–1209, March 2005.

[73] K. Thorvaldsson and H. Janestad. A model for simultaneous heat, water and vapour diffusion. *Journal of food engineering*, 40:167–172, 1999.

[74] M. Turner, R. Clough, H. Martin, and L. Topp. Stiffness and deflection analysis of complex structures. *Journal of the aeronautical Sciences*, 23(9):805–824, September 1956.

[75] Underwriters Laboratories Inc., 333 Pfingsten road, Northbrook, IL 60062-2096. *UL Standard for Safety for Medical Electrical Equipment, Part 1: General Requirements for Safety, UL 60601-1, Part 1, Section 7, Clause 42.3*, april 2003.

[76] W. Vankan, J. Huyghe, M. Drost, J. Janssen, and A. Huson. A finite element mixture model for hierarchical porous media. *International journal for numerical methods in engineering*, 40:193–210, 1997.

[77] T. Vogl, R. Straub, S. Zangos, M. Mack, and K. Eichler. Mr-guided laser-induced thermotherapy of liver tumours: experimental and clinical data. *International Journal of Hyperthermia*, 20(7):713–724, November 2004.

[78] website: medlineplus. www.nlm.nih.gov.

[79] D. K. Whittaker. Mechanisms of tissue destruction following cryosurgery. *Annals of the royal college of surgerons of england*, 66(5):313–318, 1984.

[80] I. Wieland and P. Clegg. Temperature measurement of the ceramic tip in ex vivo bovine liver. University of Bath, unpublished data, 2008.

[81] W. Wien. Lehrbuch der hydrodynamik. *Hirzel, Leipzig*, page 274, 1900.

[82] D. Yang, M. C. Converse, D. M. Mahvi, and J. G. Webster. Measurement and analysis of tissue temperature during microwave liver ablation. *IEEE Transactions on Biomedical Engineering*, 54(1):150–155, January 2007.

[83] M. M. Yeh, B. S. Trembly, E. B. Douple, T. P. Ryan, P. J. Hoopes, E. Jonsson, and J. A. Heaney. Theoretical and experimental analysis of air cooling for intracavitary microwave hyperthermia applicators. *IEEE Transactions on Biomedical Engineering*, 41(9):874–882, 1994.

[84] O. C. Zienkiewicz. Reduced integration technique in general analysis of plates and shells. *International Journal of Numerical methods in engineering*, 3(2):275–290, april–june 1971.

Appendix A

Flow for an annular geometry

Velocity profile and pressure drop in an annular geometry

The cooling gas flow inside the applicator for the inflow between the center conductor and the inner coax and for the outflow flows between the inner shaft and outer coax. For both cases, it is a fluid flowing between two cylinders of an outer radius r_0 and an inner radius r_i. The one dimensional Navier Stokes equation for a laminar incompressible flow in steady state regime with constant viscosity, zero volume forces and assuming a constant pressure gradient, is solved for the flow between two cylinders to obtain the pressure drop.

The velocity has only one component along the direction z. The pressure gradient acts only in the z direction and is constant. The fluid is assumed to be fully developed so the z velocity component is only a function of the radial direction.

For a low Mach number, the incompressibiltiy of the gas can be assumed, with the velocity only in the z direction, we have:

$$v_r = 0 \tag{A.1}$$

$$v_\theta = 0 \tag{A.2}$$

$$v_z = v_z(r) \tag{A.3}$$

$$\nabla \cdot \boldsymbol{v} = 0 \tag{A.4}$$

The Navier stokes equations in cylindrical coordinates (z, r, θ) for a laminar incompressible flow are [60]:

$$\rho(\frac{\partial v_z}{\partial t} + v_z\frac{\partial v_z}{\partial z} + v_r\frac{\partial v_z}{\partial r} + \frac{v_\theta}{r}\frac{\partial v_z}{\partial \theta}) = -\frac{\partial p}{\partial z} + \mu\nabla^2 v_z + \rho f_z \tag{A.5}$$

$$\rho(\frac{\partial v_r}{\partial t} + v_z\frac{\partial v_r}{\partial z} + v_r\frac{\partial v_r}{\partial r} + \frac{v_\theta}{r}\frac{\partial v_r}{\partial \theta} - \frac{v_\theta^2}{r}) = -\frac{\partial p}{\partial r} + \mu(\nabla^2 v_r - \frac{v_r}{r^2} - \frac{2}{r^2}\frac{\partial v_\theta}{\partial \theta}) + \rho f_r$$

$$\rho(\frac{\partial v_\theta}{\partial t} + v_z\frac{\partial v_\theta}{\partial z} + v_r\frac{\partial v_\theta}{\partial r} + \frac{v_\theta}{r}\frac{\partial v_\theta}{\partial \theta} + \frac{v_\theta v_r}{r}) = -\frac{1}{r}\frac{\partial p}{\partial \theta} + \mu(\nabla^2 v_\theta - \frac{v_\theta}{r^2} + \frac{2}{r^2}\frac{\partial v_r}{\partial \theta}) + \rho f_\theta$$

with

$$\nabla^2 v_i = \frac{\partial^2 v_i}{\partial^2 z} + \frac{1}{r}\frac{\partial}{\partial r}(r\frac{\partial v_i}{\partial r}) + \frac{1}{r^2}\frac{\partial^2 v_i}{\partial^2 \theta} \quad \text{with i = z, r, } \theta \tag{A.6}$$

With the previous assumptions, the only remainning terms is:

$$\frac{1}{r}\frac{\partial}{\partial r}(r\frac{\partial v_z}{\partial r}) = \frac{1}{\mu}\frac{dp}{dz} \tag{A.7}$$

The boundary condition on the wall of the tubes are:

$$v_z(r_i) = v_z(r_0) = 0 \tag{A.8}$$

The velocity profile between two cylinder is obtained by integrating A.7 :

$$v_z(r) = \frac{1}{4\mu}\frac{dp}{dz}(r^2 - r_i^2) + \frac{1}{4\mu}\frac{dp}{dz}(r_0^2 - r_i^2)\frac{lnr_i - lnr}{ln\frac{r_0}{r_i}} \tag{A.9}$$

The mean velocity is calculated in order to express the presure gradient as a function of the mean velocity. The mean velocity is obtained by integrating the velocity between the inner and outer radii of the annular area.

$$v_m = \frac{1}{\pi(r_0^2 - r_i^2)}\int_{r_i}^{r_0} 2\pi r v_z(r) dr \tag{A.10}$$

$$v_m = \frac{1}{2\mu}\frac{dp}{dz}\frac{1}{r_0^2 - r_i^2}\left[\frac{r^4}{4}\Big|_{r_i}^{r_0} - \frac{r_i^2 r^2}{2}\Big|_{r_i}^{r_0} + \frac{r_0^2 - r_i^2}{ln\frac{r_0}{r_i}}\frac{ln(r_i)r^2}{2}\Big|_{r_i}^{r_0} - \frac{r_0^2 - r_i^2}{ln\frac{r_0}{r_i}}\int_{r_i}^{r_0} rln(r)dr\right] \tag{A.11}$$

$$= \frac{1}{2\mu}\frac{dp}{dz}\frac{1}{ln\frac{r_0}{r_i}}\left[ln\frac{r_0}{r_i}\frac{r_0^2 - r_i^2}{4} + \frac{lnr_i(r_0^2 - r_i^2)}{2} - \frac{r_0^2 lnr_0 - r_i^2 lnr_i}{2} + \frac{r_0^2 - r_i^2}{4}\right] \tag{A.12}$$

where $k = \frac{r_i}{r_0}$ the average velocity is:

$$v_m = -\frac{1}{8\mu}\frac{dp}{dz}\frac{1}{lnk}r_0^2\big[lnk(1+k^2) + 1 - k^2\big] \tag{A.13}$$

and the pressure gradient is:

$$\frac{dp}{dz} = -\frac{8\mu lnk\, v_m}{r_0^2[lnk(1+k^2) + 1 - k^2]} \tag{A.14}$$

From the previous assumptions and from equation A.14, the pressure drop in an annular geometry is only a function of the viscosity μ of the fluid, the mean velocity v_m and the ratio k betweeen inner and outer diameters.

Pressure drop for air flowing between the shaft and the coax

The inner radius is $r_i = 0.9\,mm$ and $r_0 = 1\,mm$ for the outer radius. The area between the shaft and the coax is: $\pi(r_0^2 - r_i^2) = 0.597\,mm^2$. For a volume flow rate of $5\,lmin^{-1}$ wich is $8.3333 \times 10^{-5}\,\frac{m^3}{s}$, the average velocity is:

$$v_m = \frac{V}{A} = \frac{8.3333 \times 10^{-5}}{0.597 \times 10^{-6}} = 139.6\,\frac{m}{s} \tag{A.15}$$

The pressure gradient is:

$$\frac{dp}{dz} = \frac{8 \times 181.1 \times 10^{-7} \times ln0.9 \times 140}{[ln0.9 \times (1 + 0.9^2) + 1 - 0.9^2] \times 10^{-6}} = 3042000 \, \frac{Pa}{m} \tag{A.16}$$

So, for a length of 10cm, the pressure drop is 3.04 bars. For an input of air at $-20\,^{\circ}\mathrm{C}$, to take account of the higher density of cold air, the mean velocity for a $5\,lmin^{-1}$ flow rate is $118\,ms^{-1}$. The corresponding pressure drop is 2.56 bars.

Pressure drop for air flowing inside the coaxial line between the inner and outer conductor

The inner radius is $r_i = 0.45\,mm$ and the outer radius is $r_0 = 0.75\,mm$.

$$\frac{dp}{dz} = \frac{8 \times 181.1 \times 10^{-7} \times ln0.6 \times 73.6}{[ln0.6 \times (1 + 0.6^2) + 1 - 0.6^2] \times 5.625 \times 10^{-7}} = 176900 \frac{Pa}{m} \tag{A.17}$$

For the air flowing inside the coaxial cable at room temperature, the pressure drop is 0.177 bar for a 10 cm length tube. The mean velocity for a temperature of $-20\,^{\circ}\mathrm{C}$ at the entrance is $62\,ms^{-1}$ to have a standard flow rate of $5\,lmin^{-1}$, the corresponding pressure drop is 0.149 bars.

Pressure drop for both channels

The pressure drop due to both channel is $0.177 + 3.04 = 3.2$ bars for room temperature air and $0.15 + 2.56 = 2.71$ bars for air at $-20\,^{\circ}\mathrm{C}$.

Appendix B

Stress in the ferrule and ceramic interface

In order to evaluate the stress between the copper ferrule and the ceramic during the heating process, the thermal stress is calculated for two cylinders of copper and ceramic in contact. Calculations are similar to the example of thermal stress calculation of a steel and copper ring [24]. Stress calculations were made to evaluate the average stress in the wall of the ceramic and the copper ferrule cylinder. The thickness is small compared to the radius, we consider only the tangential stress (hoop stress) which is assumed constant through the thickness. The behaviour law for the ceramic and the copper is the linear elastic Hooke's law.

$$\sigma = E\epsilon \tag{B.1}$$

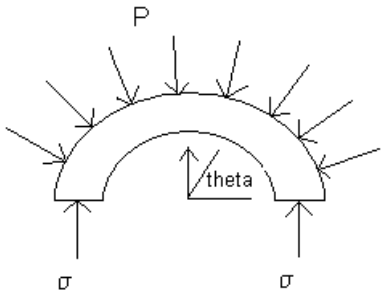

Figure B.1: Radial stress on the cylinder wall

Circumferential stress

Under and external stress p, the cylinders in equilibrium give:

$$\int_0^{\pi} psin\theta Rd\theta = 2\sigma_1 e_1 \tag{B.2}$$

and

$$\int_0^{\pi} psin\theta Rd\theta = 2\sigma_2 e_2 \tag{B.3}$$

with σ_1 the internal circumferential stress inside the copper ferrule wall and σ_2 the internal circumferiential stress inside the ceramic wall under a pressure p. So the circumferential uniform stress in the copper is:

$$\sigma_1 = \frac{pR}{e_1} \tag{B.4}$$

in the ceramic the stress is:

$$\sigma_2 = \frac{pR}{e_2} \tag{B.5}$$

When we heat both the copper and the ceramic, a compressive stress appeared in the copper ferrule and a traction stress appeared in the ceramic due to the difference of thermal expansion. At the equilibrium, the copper has a compressive stress σ_1 due to the stress p. Assuming a linear elastic behaviour, the corresponding displacement is:

$$\Delta l_{copper} = \frac{\pi R\sigma_1}{E_1} \tag{B.6}$$

The ceramic has a traction stress σ_2 due to the stress p. The corresponding displacement is:

$$\Delta l_{ceramic} = \frac{\pi R\sigma_2}{E_2} \tag{B.7}$$

Now the copper and the ceramic are heated and from T_1 to T_2 The displacement for the copper is:

$$\Delta l_{copper} = \pi R\alpha_1 \Delta T - \frac{\pi R\sigma_1}{E_1} \tag{B.8}$$

The displacement for the ceramic is:

$$\Delta l_{ceramic} = \pi R\alpha_2 \Delta T + \frac{\pi R\sigma_2}{E_2} \tag{B.9}$$

We can use the linear property and add the displacement due only to the thermal expansion and the displacement due to an external stress.(during expansion of the copper, the ceramic generates a stress p on the copper).

Now, we suppose the compatibility of deformation, that means the ceramic and copper ferrule remained in contact:

$$\Delta l_{copper} = \Delta l_{ceramic} \tag{B.10}$$

By using equations B.8 and B.9 we have:

$$\pi R\alpha_1 \Delta T - \frac{\pi R\sigma_1}{E_1} = \pi R\alpha_2 \Delta T + \frac{\pi R\sigma_2}{E_2} \tag{B.11}$$

and with equation B.4 and B.5 we have:

$$pR\left[\frac{1}{E_2 e_2} + \frac{1}{E_1 e_1}\right] = \Delta T(\alpha_1 - \alpha_2) \tag{B.12}$$

hence,

$$p = \frac{\Delta T[\alpha_1 - \alpha_2]E_1 E_2 e_1 e_2}{[E_1 e_1 + E_2 e_2]R} \tag{B.13}$$

finally

$$\sigma_1 = \frac{\Delta T[\alpha_1 - \alpha_2]E_1 E_2 e_2}{[E_1 e_1 + E_2 e_2]} \tag{B.14}$$

$$\sigma_2 = \frac{\Delta T[\alpha_1 - \alpha_2]E_1 E_2 e_1}{[E_1 e_1 + E_2 e_2]} \tag{B.15}$$

, the stress in the copper and ceramic are related to the thickness by:

$$\frac{\sigma_1}{\sigma_2} = \frac{e_2}{e_1} \tag{B.16}$$

For the 2.4 mm applicator the thickness of the copper ferrule and the ceramic are: $e_1 = 0.15\,mm$ and $e_2 = 0.29\,mm$. The average radius R_{cera} is $R_{cera} = 1.055\,mm$ and the average radius for the copper ferrule is $R_{copper} = 0.825\,mm$ for the 2.4 mm applicator. The difference of temperature is $\Delta T = 200$. The elastic modulus and thermal expansion coefficient for copper and ceramic are: $E_1 = 120\,GPa$, $\alpha_1 = 17 \times 10^{-6} C^{-1}$, $E_2 = 205\,GPa$, $\alpha_2 = 10 \times 10^{-6} C^{-1}$. The stress in the copper is $\sigma_1 = 128\,Mpa$ and the stress in the ceramic is $\sigma_2 = 67\,Mpa$.

The average radius for the 5 mm applicator for the copper ferrule is $1.65\,mm$ and $2.225\,mm$ for the ceramic. With $e_1 = 0.3\,mm$ and $e_2 = 0.8\,mm$ for the 5 mm applicator, we have: $\sigma_1 = 137\,Mpa$ and $\sigma_2 = 51\,Mpa$. The relative deformation of copper ferrule radius is:

$$\frac{\Delta R}{R} = \alpha_1 \Delta T - \frac{\sigma_1}{E_1} \tag{B.17}$$

and the relative deformation of ceramic tip is:

$$\frac{\Delta R}{R} = \alpha_2 \Delta T + \frac{\sigma_2}{E_2} \tag{B.18}$$

For the 2.4 mm applicator, the relative deformation for the copper ferrule is:

$$\epsilon = \frac{\Delta R}{R} = 17 \times 10^{-6} \times 200 - \frac{130E6}{120E9} = 2.32E - 3 \tag{B.19}$$

The relative radial deformation of the copper ferrule is 0.23 % and is in compression. With this linear analysis and assuming that the copper ferrule remained in contact with the ceramic, the relative deformation of the ceramic is the same. The relative deformation of the ceramic is 0.23 % and is positive. The ceramic is in traction.

Appendix C

Finite element method

The origin of the finite element method has its roots in is the aeronautical industry in the mid 50's after the work from Argyris, Kelsey [5] and Turner [74]. The notion of finite element is from Clough [12] and Zienkiewicz [84]. In this thesis, the finite element method is used by HFSS software package when solving Maxwell's equation in order to find the electric field pattern and the S_{11} parameter. It is also used by ANSYS sofware to solve the Navier Stokes equation and the heat equation to determine the field temperature in the fluid and solid part of the applicator.

The principle of the finite element method is to reduce a continuous equation of equilibrium in time and space into a linear equation discrete in time and space in order to solve a system of the form $A\boldsymbol{x} = \boldsymbol{b}$. Space is divided into elements which are elementary units or bricks of material and time is divided into a given number of discreet time steps. The volume is meshed into a number of elements with each element having a number of nodes. After a process of assembly (the overall matrix is filled with the contribution of each element), the global nodal vectors are obtained.

The method can be divided into a few steps. The first step is to write the equation of equilibrium in integral form and identify boundary conditions over the volume and areas attached to the domain of interest. This form is usually called the strong form. By multiplying by an arbitrary test function over all terms of the equation, integration by parts enables the inclusion of boundary conditions within the integral. This form is called the weak form, because by using integration by parts, the second derivative of the unknown has been removed. Transformation from the strong form to the weak form is shown in the following example of one-dimensional transient heat propagation in a beam in figure C.1.

Temperature is set at the origin and the heat flux is known at the end of the beam. Conservation of energy for the beam gives the transient heat equation with the boundary

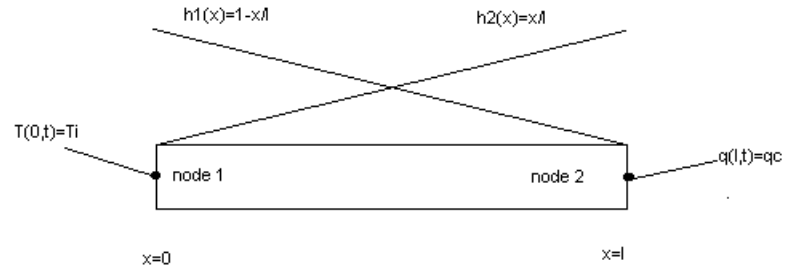

Figure C.1: Beam with two nodes, two boundary conditions and the two interpolation functions h1 and h2

conditions:

$$\rho\, C\, A \frac{\partial \theta(x,t)}{\partial t} = \frac{\partial q(x,t)}{\partial x} A \tag{C.1}$$

$$\theta(0,t) = \bar{\theta}(t) \tag{C.2}$$

$$q(l,t) = q_c \tag{C.3}$$

$$0 \leq x \leq l \tag{C.4}$$

$$0 \leq t$$

with ρ the density, C the specific heat capacity, A the area of the cross section of the beam, θ the temperature, q the heat flux through the beam and x the distance from the origin of the beam. The left hand term is the energy stored in the material and varies with the rate of temperature; the right hand term is the heat flux gradient going inside the beam. By multiplying by a test function and integrating over the length l, the equation becomes:

$$\int_0^l \rho C\, A \frac{\partial \theta}{\partial t} w\, dx - \int_0^l \frac{\partial q}{\partial x} A\, w\, dx = 0 \;\; \forall w \tag{C.5}$$

Then, by integrating by parts the weak form with continuous function is obtained:

$$\int_0^l \rho C\, A \frac{\partial \theta}{\partial t} w\, dx + \int_0^l q\, A \frac{\partial w}{\partial x} dx + w(0)q(0)A - w(l)q(l)A = 0 \;\; \forall w \tag{C.6}$$

Because the temperature at the origin is known $\theta(0,t) = \bar{\theta}(t)$, it implies that the virtual temperature or test function cancels at the origin so that $w(0,t) = 0$. This is called an essential boundary condition. The approximate discreet form is obtained by writing the same equation with the approximated functions written with the indices h.

$$\int_0^l \rho C\, A \frac{\partial \theta^h}{\partial t} w^h\, dx + \int_0^l q^h\, A \frac{\partial w^h}{\partial x} dx + w^h(0)q^h(0)A - w^h(l)q^h(l)A = 0 \;\; \forall w^h$$

Now, we express the approximate temperature rate and test function with the linear interpolation function $h_1(x) = 1 - \frac{x}{l}$ and $h_2(x) = \frac{x}{l}$. The matrix of interpolating functions

is $B(x) = (h_1\ h_2)$. The approximate variables are expressed with the interpolation functions. The approximate temperature θ^h, temperature rate $\dot{\theta}^h$, test function w^h, gradient of test function $\frac{\partial w^h}{\partial x}$ are expressed below:

$$\theta^h(x,t) = h_1(x)\theta_1(t) + h_1(x)\theta_1(t) = B(x)\boldsymbol{\theta}(t) \tag{C.7}$$
$$\dot{\theta}^h(x,t) = h_1(x)\dot{\theta}_1(t) + h_1(x)\dot{\theta}_1(t) = B(x)\dot{\boldsymbol{\theta}}(t)$$
$$w^h(x,t) = B(x)\boldsymbol{w}(t) \tag{C.8}$$
$$\frac{\partial w^h(x,t)}{\partial x} = B'(x)\boldsymbol{w}(t)$$

where

$$\boldsymbol{\theta}(t) = \begin{pmatrix} \theta_1(t) \\ \theta_2(t) \end{pmatrix}$$
$$\dot{\boldsymbol{\theta}}(t) = \begin{pmatrix} \dot{\theta}_1(t) \\ \dot{\theta}_2(t) \end{pmatrix} \tag{C.9}$$

with $\boldsymbol{\theta}(t)$, $\dot{\boldsymbol{\theta}}(t)$ the nodal temperature and rate temperature vectors respectively. The nodal test vector $\boldsymbol{w}(t)$ is defined by:

$$\boldsymbol{w}(t) = \begin{pmatrix} w_1(t) \\ w_2(t) \end{pmatrix}$$

The value for the test function at the extremity of the bar is $w_l^h = B(l)\boldsymbol{w}(t)$ and the approximated heat flux is expressed as a function of the nodal temperature $q_h(x,t) = kB'(x)\boldsymbol{\theta}(t)$. In our example there are only two nodes, the origin is located at $x = 0$ and the extremity of the beam at $x = l$. For this example the two linear interpolation functions are defined over the length l of the beam and are therefore called global functions. The local approach, which consists of defining local functions attached to each element, is easier to programme and to use for a large model. In this example, the length could be replaced by the length l_e of one element.

Local interpolation functions have to satisfy three necessary conditions. They have to be continuous enough in the neighbourhood of their node and have to take a unit value at the node to which they are attached, and zero on other nodes. They have to be differentiable inside the element to keep the differentiability of the assembled solution. They have to contain at least one constant and a linear term to assure the convergence to the exact solution when the number of elements increased [15].

Approximate temperature, rate temperature and test function expressed with the linear function of interpolation are inserted in the approximate weak form. The nodal test function factorises the equation of equilibrium.

$$\boldsymbol{w^T}[\rho\, C \int_0^l B^T B dx \dot{\boldsymbol{\theta}}(t) + k \int_0^l B'^T B' dx \boldsymbol{\theta}(t) - \boldsymbol{q}(t)] = 0\ \forall \boldsymbol{w}(t) \tag{C.10}$$

with $\boldsymbol{q}(t)$ the nodal heat flux vector. By calculating the integral we obtain finally:

$$\frac{\rho C\, l}{6}\begin{pmatrix}2 & 1\\ 1 & 2\end{pmatrix}\begin{pmatrix}\dot{\theta}_1\\ \dot{\theta}_2\end{pmatrix} + \frac{k}{l}\begin{pmatrix}1 & -1\\ -1 & 1\end{pmatrix}\begin{pmatrix}\theta_1\\ \theta_2\end{pmatrix} = \begin{pmatrix}q_1\\ q_2\end{pmatrix} \tag{C.11}$$

The problem of heat conduction in a beam with the previous boundaries conditions C.3 and C.4 has been reduced in a matrix form and vector form.

The choice of interpolation function is usually linear, quadratic or cubic. By carrying out this process, the new problem to be solved is discrete and can be solved by a numerical method such as Gaussian elimination. The approximate solution can be closer to the exact solution by increasing the number of elements and/or the order of functions of interpolation. The higher is the order of the function of interpolation the higher the number of nodes becomes.

Similarly, an increased number of elements increases the number of nodes and the size of the matrix and nodal vectors. The finite element method considered then divides a volume into sub domains called the elements. For each element, the discrete equation of equilibrium is solved as shown in this example. To obtain the overall solution, the overall matrix is filled with all the nodal forces that contributed to a given node. This process is called assembling. The finite element method is well suited to solve classical equations of engineering for complex geometries.

Appendix D

Calculation of the characteristic impedance

Centered configuration

Analytic calculations are made for the characteristic impedance of a coaxial cable with two different dielectrics, PTFE and Air between the inner and outer conductor in the centered configuration and off centered configuration with an eccentricity e.

The coax cable is made of an inner and outer conductor of copper material and PTFE heat shrink tube around the inner conductor. The radius of the center conductor is $R_a = 0.25\,mm$

The radius with the ptfe around is $R_c = 0.45\,mm$

The inner radius of the coaxial cable is $R_b = 0.75\,mm$

The constant permittivity of free space is $\epsilon_0 = 8.854 \times 10^{-12}\,\frac{F}{m}$ and the constant magnetic permeability is $\mu_0 = 4\pi \times 10^{-7}\,\frac{H}{m}$

The characteristic impedance is calculated for a coaxial cable with air and ptfe material, the impedance of free space is : $\eta_0 = \sqrt{\frac{\mu_0}{\epsilon_0}} = 376.798\,\Omega$. The relative permittivity of the dielectric inside the coax cable is 1 for air and 2 for the ptfe

$$\epsilon_r = 1 \;\; R_c \leqslant r \leqslant R_b \tag{D.1}$$

$$\epsilon_r = 2 \;\; R_a \leqslant R_c \tag{D.2}$$

$$\tag{D.3}$$

The general expression for the characteristic impedance from the transmission line theory is given by:

$$Z_0 = \sqrt{\frac{R + j\omega L}{G + j\omega C}} \tag{D.4}$$

where $R\,[\Omega m^{-1}]$ is the resistance, $L\,[Hm^{-1}]$ is the inductance, $G\,[Sm^{-1}]$ is the conductance, and $C\,[Fm^{-1}]$ is the capacitance of the line. Copper is a very good conductor so the case of a lossless coaxial line is assumed. Therefore the characteristic impedance of the line is:

$$Z_0 = \sqrt{\frac{L}{C}} \tag{D.5}$$

Because the magnetic relative permeability of ptfe is the same as air $\mu_r = 1$, the inductance is given by:

$$L = \frac{\mu_0 \mu_r}{2\pi} ln \frac{R_b}{R_a} = \frac{\mu_0}{2\pi} ln \frac{R_b}{R_a} \tag{D.6}$$

The capacitance C is calculated from the electric field, the gauss law states that the total electric flux leaving a closed surface is equal to the total charge enclosed by the surface. For the cylinder geometry we can write:

$$Q = \epsilon \int_{\partial\Omega} \boldsymbol{E} \cdot \boldsymbol{ds} \quad = \quad \epsilon E 2\pi\rho L \tag{D.7}$$

Hence, the electric field only in the radial direction is:

$$\boldsymbol{E} = \frac{Q}{2\pi\epsilon\rho L} \boldsymbol{e_\rho} \tag{D.8}$$

The electric potential is given by integrating the electric field over a length $\boldsymbol{dl} = d\rho \boldsymbol{e_\rho}$

$$\begin{aligned} V &= -\int_{R_b}^{R_a} \boldsymbol{E} \cdot \boldsymbol{d}l & \text{(D.9)} \\ &= -\int_{R_b}^{R_a} \frac{Q}{2\pi\epsilon_0\epsilon_r\rho L} d\rho & \text{(D.10)} \\ &= -\int_{R_b}^{R_c} \frac{Q}{2\pi\epsilon_0\epsilon_{air}\rho L} d\rho - \int_{R_c}^{R_a} \frac{Q}{2\pi\epsilon_0\epsilon_{ptfe}\rho L} d\rho & \text{(D.11)} \\ &= \frac{Q}{2\pi\epsilon_0 L} (\frac{1}{\epsilon_{air}} ln \frac{R_b}{R_c} + \frac{1}{\epsilon_{ptfe}} ln \frac{R_c}{R_a}) & \text{(D.12)} \end{aligned}$$

The capacitance $C\,[Fm^{-1}]$ is the ratio of the charge Q and the potential V:

$$C = \frac{2\pi\epsilon_0}{\frac{1}{\epsilon_{air}} ln \frac{R_b}{R_c} + \frac{1}{\epsilon_{ptfe}} ln \frac{R_c}{R_a}} \tag{D.13}$$

The capacity is the combination of two capacitors in series. The capacity C_1 due to the ptfe is:

$$C_1 = \frac{2\pi\epsilon_0}{\frac{1}{\epsilon_{ptfe}} ln \frac{R_c}{R_a}} \tag{D.14}$$

and the capacity C_2 due to air dieletric is

$$C_2 = \frac{2\pi\epsilon_0}{ln \frac{R_b}{R_c}} \tag{D.15}$$

for two capacitors in series we have:

$$\frac{1}{C} = \frac{1}{C_1} + \frac{1}{C_2} \tag{D.16}$$

Now, the characteristic impedance Z_0 is calculated from D.5 with D.6 and D.13.

$$Z_0 = \sqrt{\frac{L}{C}} = \sqrt{\frac{\frac{\mu_0}{2\pi} ln\frac{R_b}{R_a}}{\frac{2\pi\epsilon_0}{ln\frac{R_b}{R_c} + \frac{1}{\epsilon_{ptfe}} ln\frac{R_c}{R_a}}}} \tag{D.17}$$

$$= \frac{1}{2\pi}\sqrt{\frac{\mu_0}{\epsilon_0}}\sqrt{ln\frac{R_b}{R_a}(ln\frac{R_b}{R_c} + \frac{1}{\epsilon_{ptfe}} ln\frac{R_c}{R_a})} \tag{D.18}$$

$$= \frac{1}{2\pi} \times 376.7 \times \sqrt{ln3(ln1.666 + \frac{1}{2} ln1.8)} \tag{D.19}$$

$$= 56.37\,\Omega \tag{D.20}$$

Coaxial line with eccentricity e

For a dielectric between the inner and outer conductor the characteristic impedance can be calculated by using a stereographic projection [33] and conformal transformation [16]. A conformal transformation is a mapping transformation that preserves angles between every pair of curves at each point of some domain. By using a transformation, the capacity is easier to calculate. Capacity is conserved with a conformal transformation.

The first conformal transformation used is:

$$w(z) = sinh(x_1) coth(\frac{z}{2}) \tag{D.21}$$

This cotangent hyperbolic transformation transforms circles into parallel lines. This circle defining the boundary of the dielectric is transformed in a curved countour. The second conformal transformation used is :

$$w(z) = \frac{z - z_2}{z - z_1} \tag{D.22}$$

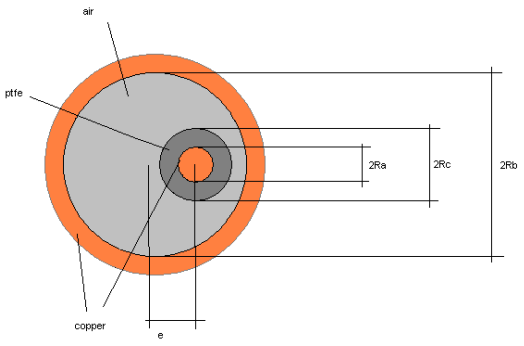

Figure D.1: Cross section of a coaxial line of eccentricity e

The conductor's boundaries are transformed in concentric circles, and the boundary of the dielectric is transformed in a circle with a center displaced from the origin. By using the stereographic projection [33], the characteristic impedance for an eccentric coaxial line is:

$$Z_0 = \frac{\sqrt{\frac{\mu_r \mu_0}{\epsilon_r \epsilon_r}}}{2\pi} cosh^{-1}(\frac{R_a^2 + R_b^2 - 4e^2}{2R_a R_b}) \tag{D.23}$$

The dimensions used are from figure D.1. This formula applies only when there is one dielectric of relative permittivity ϵ_r between the two conductors. The calculation of the impedance for the coaxial line of figure 1 is done in 2 steps. The first step is to calculate the inductance of the coaxial line. Because PTFE is non magnetic material, the medium between the inner and outer conductor has a magnetic permeability of 1. The stereographic projection is used to calculate the inductance [33]. The second step is to calculate the capacity for an eccentric coaxial line with a dielectric. It has been done by Das *et al* [16]. The conformal mapping transformation used is a bilinear transformation followed by a logarithmic transformation. The speed of propagation of a wave is :

$$v = \frac{1}{\sqrt{LC}} = \frac{1}{\sqrt{\mu\epsilon}} \tag{D.24}$$

hence, the inductance can be expressed as:

$$L = \sqrt{\mu\epsilon} Z = \frac{\mu}{2\pi} cosh^{-1}(\frac{R_a^2 + R_b^2 - 4e^2}{2R_a R_b}) \tag{D.25}$$

The transformation is:

$$w = u + jv = \frac{z - z_2}{z - z_1} = \frac{x + jy - z_2}{x + jy - z_1} \tag{D.26}$$

and transforms the circles C_1 and C_2 into a coaxial configuration.

The final expression for the capacity is [16]:

$$C = \frac{\epsilon_0 \epsilon_r}{ln\frac{\rho_1}{\rho_2}} \int_0^{2\pi} \frac{d\phi}{1 + (\epsilon_r - 1)\frac{ln\frac{\rho_1}{f(\phi)}}{ln\frac{\rho_1}{\rho_2}}} \tag{D.27}$$

where ρ_1 and ρ_2 are the radii of the outer and inner conductor in the w plane. $f(\phi)$ parameterizes the location of the point of the circle of the dielectric.

As shown in table D.1, the calculated impedance and the impedance obtained with a finite element model are exact for the first decimal point. The error is less than 0.2 % as shown in table D.1

e	$Z_{model}\,[\Omega]$	$Z_{calculated}\,[\Omega]$	error[%]
0	56.412	56.400	0.021
0.05	56.069	56.065	0.007
0.1	55.042	55.038	0.007
0.15	53.267	53.272	-0.009
0.2	50.650	50.650	0.001
0.25	46.968	46.959	0.017
0.29	43.060	42.969	0.211

Table D.1: Variation of characteristic impedance with eccentricity, $\epsilon_r = 2$

Appendix E

Power handling of a coaxial line

Minimum attenuation constant

The attenuation constant α can be expressed as [59] :

$$\alpha = \frac{P_l(z)}{2P(z)} = \frac{P_l(z=0)}{2P_0} \tag{E.1}$$

where P_0 is the input power and P_l is the power loss per unit length. From [59], the attenuation constant for a coaxial line is:

$$\alpha_c = \frac{R_s}{2\eta ln\frac{R_b}{R_a}}(\frac{1}{R_a}+\frac{1}{R_b}) \tag{E.2}$$

$$= \frac{R_s}{2\eta R_b}\frac{x+1}{lnx} \tag{E.3}$$

with $x = \frac{R_b}{R_a}$ the ratio between the outer radius R_b and inner radius R_a conductor and R_s the surface resistance of the conductors and $\eta = \sqrt{\frac{\mu}{\epsilon}}$. To find the value x of the ratio between the outer and inner conductor that minimize the attenuation constant , we take the derivative:

$$\frac{d\alpha_c(x)}{dx} = K\frac{lnx-(x+1)\frac{1}{x}}{(lnx)^2} \tag{E.4}$$

$$= Kf(x) \tag{E.5}$$

with $K = \frac{R_s}{2\eta R_b}$ after simplification, the attenuation constant is minimized when:

$$xlnx = 1+x \tag{E.6}$$

The value $x = \frac{R_b}{R_a} = 3.591$ satisfaying the equation E.6 is an extremum. To check that it is a minimum for the function f, the second derivative of f must be positive:

$$\frac{d^2f(x)}{dx^2} = \frac{lnx+2}{x^2}+\frac{2-lnx}{x} \tag{E.7}$$

we have

$$\frac{d^2 f(3.591)}{dx^2} \geq 0 \tag{E.8}$$

so $x = \frac{R_b}{R_a} = 3.591$ is a minimum and minimises the attenuation constant of a coaxial line. For a relative permittivity of 1, the corresponding characteristic impedance is 77 Ω.

Maximal power Handling

The electric field inside a coaxial line is:

$$E(\rho) = \frac{V_0}{\rho ln \frac{R_b}{R_a}} \tag{E.9}$$

The maximum electric field occurs for $\rho = R_a$. The electric field breakdown of air is $E_d = 3 \times 10^6 \frac{V}{m}$. Thus, the maximum voltage before breakdown is:

$$V_{max} = E_d R_a \, ln \frac{R_b}{R_a} \tag{E.10}$$

The characteristic impedence Z_0 of the line is:

$$Z_0 = \frac{\eta_0}{2\pi} ln \frac{R_b}{R_a} \tag{E.11}$$

and the maximum power capacity is:

$$\begin{aligned} P_{max} &= \frac{V_{max}^2}{2Z_0} && \text{(E.12)} \\ &= \frac{\pi R_a^2 E_d^2}{\eta_0} \, ln \frac{R_b}{R_a} && \text{(E.13)} \\ &= c_1 R_a^2 \, ln \frac{R_b}{R_a} && \text{(E.14)} \\ &= R_b^2 c_1 \frac{R_a^2}{R_b^2} \, ln \frac{R_b}{R_a} && \text{(E.15)} \\ &= c_2 \frac{lnx}{x^2} && \text{(E.16)} \\ &= c_2 g(x) && \text{(E.17)} \end{aligned}$$

with $c_1 = \frac{\pi E_d^2}{\eta_0}$ and $c_2 = R_b^2 c_1$ two constants independant of $x = \frac{R_b}{R_a}$. To find the value x that maximize the power capacity, the derivative of the function g of expression E.17 is calculated:

$$\frac{dg(x)}{dx} = \frac{x - 2xlnx}{x^4} = \frac{1 - 2lnx}{x^3} \tag{E.18}$$

The extrema is obtained for $lnx = \frac{1}{2}$ or $x = e^{0/5} = 1.648$. To check that it is a maximum, the second derivative has to be negative:

$$\frac{d^2 g(x)}{dx^2} = \frac{-5 + 6\, lnx}{x^4} \tag{E.19}$$

the value $g''(e^{0.5})$ is negative , so $x = 1.648$ is a maximum. This ratio maximize the power handling inside a coaxial line. The corresponding characteristic impedance obtained with E.11 is $Z_0 = 30\,\Omega$.

Impedance of a standard coaxial line

Standard coaxial lines usually have a characteristic impedance of 50Ω which a compromise between maximum power handling and minimum attenuation constant to minimize losses of the line. From the catalogue of Micro Coax company, the attenuation constant of the 1.8 mm coaxial line low loss (Cable UT 70-LL) is $0.646\ dBm^{-1}$ at 1 GHz and $1.463\ dBm^{-1}$ at 5 GHz. A linear interpolation gives an attenuation of $0.942\ dBm^{-1}$ at 2.45 GHz. The ratio between the power at the end of the coaxial line P_0 and the input power P_i for a 20 cm length is:

$$-0.0189 = log(\frac{P_0}{P_i}) \tag{E.20}$$

hence,

$$\frac{P_0}{P_i} = 0.96 \tag{E.21}$$

If the input power P_i is 60 watts, the loss inside the coax cable of a 20 cm length is 2.4 watts. For an input power of 80 watts, the loss is 3.2 watts.

Appendix F

Temperature recorded with a thermocouple

The thermocouple measured the temperature of its surrounding. Depending of the thermal conductivity of the material in contact with the thermocouple, the temperature of recorded by the thermocouple at the junction of the two surfaces is function of both the inner and outer surface.

To assess the effect of the aluminium tape employed to stick the thermocouples on to the shaft during temperature measurement, a thermal steady calculation in the radial direction was performed.

Geometry

The model consist of the shaft and two thin layers of high conductivity material such as copper representing the thermocouple. The tape is a thin layer of aluminium material. The geometry and dimensions of the model are given in figure F.1. $T1$ is the shaft temperature, $T2$ is the thermocouple temperature, $T3$ is the temperature of the aluminium tape on the inner surface and $T4$ is the temperature of the tape on its outside surface.

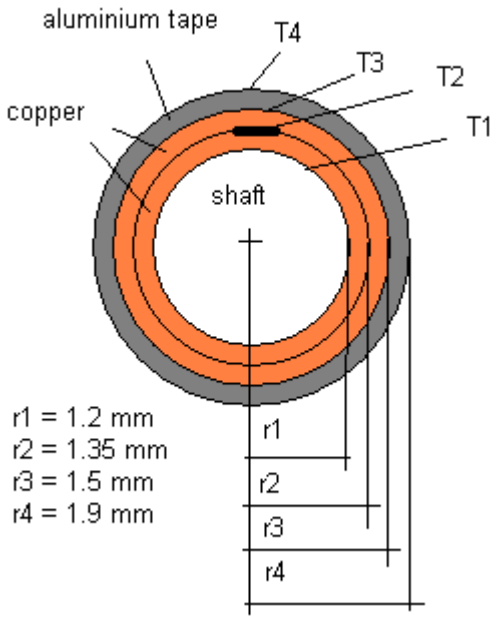

Figure F.1: Geometry of the model for the thermocouple located on the shaft with aluminium tape

Assumptions

The heat conduction occurs only in the radial direction, the material properties are constant, the system is in thermal equilibrium. The shaft $T1$ temperature is given and the outside temperature $T4$ on the tape is assumed to be the room temperature. The thermal conductivity of material 1 is copper which is $400\,Wm^{-1}K^{-1}$, the thermal conductivity of material 2 which is pure aluminium is $277\,Wm^{-1}K^{-1}$.

Goal

The temperature of the thermocouple $T2$ is influenced by the surrounding. By knowing the shaft temperature $T1$ and the outside temperature $T4$, we want to find a relationship expressing the $T2$ in function of these two temperatures.

Equation of heat in radial direction

In cylindrical coordinates for one dimensional heat conduction in steady state regime with no heat generation, the heat equation is:

$$\frac{1}{r}\frac{d}{dr}\left(r\frac{dT}{dr}\right) = 0 \tag{F.1}$$

By solving this equation, the temperature distribution can be calculated for the model of figue F.1. The equation F.1 implies that the heat rate is constant through the different

materials.

Resolution

The heat rate are expressed for each interface by using the definition of the heat rate $q = kA\frac{dT}{dr}$ with $A = 2\pi rl$ the area of the cylinder of radius r and the temperature solution obtain with equation F.1.

$$q = \frac{2\pi\, l\, k_1\,(T_1 - T_2)}{ln\frac{r_2}{r_1}} \tag{F.2}$$

$$= \frac{2\pi\, l\, k_2\,(T_2 - T_3)}{ln\frac{r_3}{r_2}} \tag{F.3}$$

$$= \frac{2\pi\, l\, k_3\,(T_3 - T_4)}{ln\frac{r_4}{r_3}} \tag{F.4}$$

$k_1 = k_2$, hence from the first two equation, the temperature $T2$ can be expressed in function of $T1$ and $T3$:

$$T_2 = \frac{\frac{1}{ln\frac{r_2}{r_1}}T_1 + \frac{1}{ln\frac{r_3}{r_2}}T_3}{\frac{1}{ln\frac{r_3}{r_2}} + \frac{1}{ln\frac{r_2}{r_1}}} \tag{F.5}$$

$$= f_1\,(T_1, T_3) \tag{F.6}$$

With the second equation F.3 and third equation F.4, the temperature $T3$ can be expressed as a function of $T2$ and $T4$:

$$T_3 = \frac{\frac{k_2}{ln\frac{r_3}{r_2}}T_2 + \frac{k_3}{ln\frac{r_4}{r_3}}T_4}{\frac{k_3}{ln\frac{r_4}{r_3}} + \frac{k_2}{ln\frac{r_3}{r_2}}} \tag{F.7}$$

$$= f_2\,(T_2, T_4) \tag{F.8}$$

By combining equations F.5 and F.7, the thermocouple temperature $T2$ can be expressed in function of the shaft temperature $T1$ and the outside temperature $T4$.

$$T_2 = \frac{\frac{1}{ln\frac{r_2}{r_1}}T_1 + \frac{1}{ln\frac{r_3}{r_2}}\left(\frac{\frac{k_2}{ln\frac{r_3}{r_2}}T_2 + \frac{k_3}{ln\frac{r_4}{r_3}}T_4}{\frac{k_3}{ln\frac{r_4}{r_3}} + \frac{k_2}{ln\frac{r_3}{r_2}}}\right)}{\frac{1}{ln\frac{r_3}{r_2}} + \frac{1}{ln\frac{r_2}{r_1}}} \tag{F.9}$$

$$T_2 = \frac{\frac{1}{ln\frac{r_2}{r_1}}T_1 + \frac{\frac{k_3}{ln\frac{r_4}{r_3}}}{ln\frac{r_3}{r_2}\left(\frac{k_3}{ln\frac{r_4}{r_3}} + \frac{k_2}{ln\frac{r_3}{r_2}}\right)}T_4}{\frac{1}{ln\frac{r_3}{r_2}} + \frac{1}{ln\frac{r_2}{r_1}} - \frac{\frac{k_2}{ln\frac{r_3}{r_2}}}{ln\frac{r_3}{r_2}\left(\frac{k_3}{ln\frac{r_4}{r_3}} + \frac{k_2}{ln\frac{r_3}{r_2}}\right)}} \tag{F.10}$$

$$= f_3\,(T_1, T_4) \tag{F.11}$$

$$= \alpha T_1 + (1 - \alpha)\,T_4 \tag{F.12}$$

with $r_1 = 1.2\,mm$, $r_2 = 1.35\,mm$, $r_3 = 1.5\,mm$, $r_4 = 1.9\,mm$, $k_1 = k_2 = 400\,Wm^{-1}K^{-1}$ and $k_3 = 277\,Wm^{-1}K^{-1}$, the equation F.10 gives $\alpha = 0.8$. This value has been used for the modelled temperature described in chapter 5.